



UNIVERSITY OF
LIVERPOOL

Low energy beam dynamics simulations for ELENA optimization

Thesis submitted in accordance with the requirements of
the University of Liverpool for the degree of Doctor in Philosophy

by

Bianca Veglia

May 2022

Declaration of Authorship

I, Bianca Veglia, declare that this thesis titled, ‘Low energy beam dynamics simulations for ELENA optimization’ and the work presented in it are my own. I confirm that:

- This work was done wholly or mainly while in candidature for a research degree at this University.
- Where any part of this thesis has previously been submitted for a degree or any other qualification at this University or any other institution, this has been clearly stated.
- Where I have consulted the published work of others, this is always clearly attributed.
- Where I have quoted from the work of others, the source is always given. With the exception of such quotations, this thesis is entirely my own work.
- I have acknowledged all main sources of help.
- Where the thesis is based on work done by myself jointly with others, I have made clear exactly what was done by others and what I have contributed myself.

Signed:

Date:

*“Four thousand holes in Blackburn, Lancashire
And though the holes were rather small
They had to count them all
Now they know how many holes it takes to fill the Albert Hall.”*

The Beatles, A Day in the Life

Abstract

Low energy antiprotons are an essential tool for antimatter research but they are hard to produce and store. The introduction of the new low energy antiproton storage ring (ELENA) at CERN will deliver low energy, high quality antiproton bunches to the antimatter experiment and increase their trapping efficiency by up to 100 times. In order to reduce the energy of the antiparticles without losses in the beam, electron cooling is employed. With the aim to guarantee the best possible beam quality from ELENA and for other next generation ultra-low energy antiproton and ion facilities, it is necessary to deeply understand the characteristics of the cooling process and to realistically include errors and imperfections in the simulation models. For this purpose, different simulation codes, as Betacool and RF-Track, were employed to investigate the effects impacting on beam, establishing realistic models of beam storage and cooling.

Acknowledgements

This thesis was developed as part of the Accelerators Validating Antimatter (AVA) project [1], an Innovative Training Network within the Horizon 2020 Marie Skłodowska-Curie actions [2]. The network comprised five universities, eight national and international research centres with 13 partners from industry. AVA is aimed at enabling an interdisciplinary and cross-sector program on antimatter research. I am very grateful of the opportunities and support the network provided me with and the great people I met through it, in particular Volodymyr and Bruno which shared their competences on ELENA.

I would like to thank my supervisor Prof. Dr. Carsten Welsch for giving me the opportunity to carry out this exciting and interesting work, and for encouraging my professional and personal development. I would also like to extend my deepest gratitude to my supervisors Dr. Javier Resta López and Dr. Aaron Farricker, who came along in the most delicate time and guided me through the preparation of this thesis.

I am grateful to have spent time as a part of the Quasar group and the Cockcroft Institute and would like to thank every member I have been fortunate enough to call a friend and a colleague for the good times we had.

At CERN I would like to thank every member of the ELENA project for their helpfulness and availability. In particular, I extend gratitude to Davide Gamba who has provided many useful and interesting discussions, and helped me to understand so much. Thank you also to Andrea Latina for being so helpful with his code and his explanations. Part of this project would not have been possible without the help of Angela Saa Hernandez and Niccolò Bianchi, who have provided their assistance with measurements at LEIR among the many things and who have my full gratitude. I also want to remember the help of Gerard Tranquille and Christian Carli and the useful discussions we had.

I thank Steve for all his kind help through my doctoral studies, thanks to Marcello for his spiritual and material support. Thank you, Pàvel, for inspiring me with your dedication.

Thanks to my family, that encouraged me so warmly and gently, including those who cannot read this words but who are present every day in my heart and memories.

Contents

Declaration of Authorship	iii
Abstract	v
Acknowledgements	vi
List of Figures	xi
List of Tables	xiii
1 Introduction	1
1.1 Introduction	1
1.2 Matter and Antimatter	2
1.2.1 Brief history of antimatter theory, experiments and production . .	2
1.3 The antiproton production and deceleration chain at CERN	4
1.4 The Extra Low ENergy Antiproton storage ring	6
1.4.1 Antimatter experiments in the ELENA era	8
1.5 Project goals and overview	14
2 Theoretical Background	15
2.1 Beam Dynamics	15
2.1.1 Co-ordinate System	16
2.1.2 Transverse Beam Dynamics	17
2.1.3 Transverse Emittance	17
2.1.4 Longitudinal Momentum Spread	19
2.2 Heating Effects	20
2.2.1 Intrabeam Scattering	21
2.2.2 Space-charge Forces	22
2.2.3 Rest Gas Scattering	23
2.3 Beam cooling	25
2.3.1 Introduction	25
2.4 Electron Cooling	26
2.4.1 Binary Collision approximation	28
2.4.2 Dielectric Theory	30

2.5	Beam Diagnostics	30
2.5.1	Beam Position Monitors	31
2.5.2	Ionisation Profile Monitor	32
2.5.3	Schottky monitor	32
2.5.4	Scraper system	33
3	The Model	35
3.1	Cooling Force	35
3.1.1	Parkhomchuk Formula	37
3.1.2	Erlangen Formula	38
3.1.2.1	Modified formula for antiprotons	41
3.2	Performance limiting factors	43
3.2.1	IBS	43
3.2.2	Space Charge in an Electron Beam	44
3.2.3	Electron Beam Shape	46
3.2.4	Misalignments	47
3.2.5	Magnetic field imperfections	48
4	Simulation Methods for Low Energy Synchrotrons	51
4.1	Simulation tools for electron cooling	51
4.2	Betacool	52
4.2.1	Betacool algorithms	52
4.2.1.1	Model Beam Algorithm	53
4.2.1.2	Kick procedure for IBS	54
4.2.1.3	Runge-Kutta Methods	54
4.2.1.4	Mapping the cooling section	55
4.2.1.5	Model of the cooler	56
4.2.1.6	Betacool modifications	58
4.3	RF-Track	59
4.4	Benchmarking	61
5	LEIR Measurements	65
5.1	LEIR	66
5.1.1	LEIR cooling force	67
5.1.2	Emittance Measurements	69
5.1.3	Electron Beam Distribution	72
5.1.4	Cooling maps	74
5.1.4.1	Orbit bumps	74
5.1.4.2	Results	75
6	ELENA studies	81
6.1	ELENA cooling force	81
6.2	Measurements	82
6.3	Emittance evolution	83
6.4	Magnetic field	84
6.4.1	The electron cooler magnetic system	85
6.4.2	Magnetic field measurements	86
6.5	Cooling Maps	92

6.6	ELENA Lifetime limitation effects and mitigations	98
6.7	Suggested measurements for the future	100
7	Summary and Conclusions	101
7.1	Outlook	104
	 Bibliography	 105

List of Figures

1.1	CERN accelerator complex	5
1.2	3D sketch of the ELENA ring and its components.	6
1.3	Optical functions of ELENA combined with horizontal dispersion at the nominal working points.	7
1.4	ELENA in the AD Hall and the beam lines transporting the antiprotons to the different experiments.	9
2.1	Curvilinear co-ordinate system applied in synchrotrons. x and y specify the transverse distance from the design orbit, z the longitudinal offset . .	16
2.2	Properties of the horizontal phase space ellipse.	19
2.3	Example of a typical ELENA cycle.	21
2.4	The ELENA tune diagram with the resonances up to third order.	23
2.5	IBS and rest gas scattering growth rates for ELENA	25
2.6	Schematics of the electron cooler system.	26
2.7	Picture of the electron cooler during installation in ELENA	29
3.1	Plot of the Coulomb logarithm as expressed in the binary collision approximation and the dielectric theory.	36
3.2	Representation of the impact of the Parkhomchuk's fitting parameter Δ_{eff} on the cooling force trend.	38
3.3	Schematic trajectories of relative motion of electrons and ions for different intensity ranges of the magnetic field.	39
3.4	Schematic representation of the difference for attractive and repulsive Coulomb interaction in magnetized electron cooling.	42
3.5	Comparison of the Erlangen cooling force model for protons and antiprotons with ELENA electron cooler parameters.	43
3.6	Distribution of an ensemble of 1000 modelled antiprotons in the cooler at $t=0$ s and at $t=4$ s for the second cooling plateau.	45
3.7	Schematic representation of electron beam distribution models used for the simulations.	46
3.8	Schematic representation of misalignments between the ion and the electron beam trajectories.	48
4.1	Cooling force for xenon ions as function of the relative ion velocity in the ESR storage ring at GSI.	62
5.1	Layout of the LEIR machine and its main components	65
5.2	Schematic of a typical LEIR cycle.	66
5.3	Longitudinal cooling force for LEIR lead ion beam as function of the relative ion velocity with respect to the rest frame of the electron beam. .	69

5.4	Lead beam profiles measured by the IPM during electron cooling. A shrinkage in the size is visible.	70
5.5	Example of the horizontal IPM signal transformation and Gaussian fit for emittance evaluation at different times during cooling.	71
5.6	LEIR emittance measurements compared with Betacool simulations for uniform electron distribution.	71
5.7	LEIR emittance measurements compared with Betacool simulations for hollow electron beam distribution.	73
5.8	LEIR emittance measurements compared with Betacool simulations for parabolic electron distribution.	73
5.9	LEIR electron cooler bump knob, calibrated to no offset and no angle	75
5.10	Vertical cooling maps for uniform electron beam distribution.	76
5.11	Vertical cooling maps for hollow electron beam distribution	77
5.12	Vertical cooling maps for parabolic electron beam distribution.	78
6.1	Longitudinal cooling force for ELENA as a function of the relative ion velocity with respect to the rest frame of the electron beam.	82
6.2	BETACOOOL emittance evolution simulations for ELENA compared with scraper data.	84
6.3	OPERA model of the ELENA cooler magnet system.	85
6.4	Measured magnetic field map inside of the ELENA electron cooler apparatus.	87
6.5	G4beamline visualisation of the electron beam inside the magnetic field.	88
6.6	Profile obtained from the first virtual detector, next to the electron source, in the G4Beamline simulation	88
6.7	Comparison of the initial and final electron beam profile across the electron cooler.	89
6.8	ELENA horizontal emittance measurements compared with Betacool simulations for different beam misalignment effects	90
6.9	ELENA vertical emittance measurements compared with Betacool simulations for different beam misalignment effects.	90
6.10	ELENA measurements compared with Betacool emittance evolution simulations.	91
6.11	Betacool emittance evolution simulations for ELENA with 0.8 mm solenoid shift and $D_x=0$ m or $D_x=1.498$ m.	91
6.12	ELENA cooling maps for uniform electron beam distribution.	93
6.13	ELENA cooling maps for Gaussian electron beam distribution.	94
6.14	ELENA cooling maps for hollow electron beam distribution.	95
6.15	ELENA cooling maps for parabolic electron beam distribution.	97
6.16	Distribution of the ELENA antiproton beam in 3D phase space ($dP/P, \varepsilon_x$).	98
6.17	BETACOOOL longitudinal momentum spread for ELENA with and without the 0.8 mm solenoid shift.	99

List of Tables

1.1	ELENA parameters.	8
2.1	Nominal electron cooler parameters for ELENA.	28
5.1	LEIR parameters.	67
5.2	Nominal electron cooler parameters for LEIR.	68
6.1	Scraper measurements results for the ELENA 100 keV cooling plateau. . .	83

Chapter 1

Introduction

1.1 Introduction

The focus of this thesis project is on simulations of the Extra Low ENergy Antiproton storage ring (ELENA), an anti-matter synchrotron operating at unprecedented low energies [3]. The project's goal is to fully characterise the performance of the machine and obtain accurate predictions of the expected beam parameters, helping to improve the efficiency of the related antimatter experiments (described in section 1.4.1).

Existing low energy storage rings, operating at similar beam energies, found limitations on beam intensity and life time in experimental studies. When the energy is very low, the self interaction of the particles in the beam becomes relevant and many approximations used at higher energies are no longer valid. This renders the description of the beam dynamics particularly tricky. Additionally electron cooling on antiprotons at such low energies had never been performed before but was successfully demonstrated in the first run of ELENA. Electron cooling plays an essential role in the success of ELENA, reducing the antiproton beam emittance and energy spread. To obtain the best quality antiprotons for experiments it is important to be able to deeply understand the characteristics of the cooling process and to realistically include errors and imperfections in the simulation models. For this purpose, different simulation codes, for example Beta-cool [4] and RF-Track [5], were employed to investigate the effects impacting on beam, establishing realistic models of beam storage and cooling.

Additionally, considerations at other low energy storage rings are also discussed, in order to develop a reliable model applicable to any low energy storage ring. All the tools developed were formulated for an overall optimisation of beam handling at low energies.

The introduction of the new ELENA ring will be essential in the pursuit of answers to the fundamental questions about antimatter. The new ring will dramatically increase the antiproton trapping efficiency of the related experiments by up to a factor of 100 [3], allowing for more detailed studies. The characterisation of the beam dynamics and optimisation of the ring operations, which is the aim of this thesis, is hence key to the successful study of antimatter.

1.2 Matter and Antimatter

Many unanswered questions are still hindering the way to a better understanding of the universe and its laws. Baryon asymmetry is one of the greatest unsolved problems in modern physics [6]. It is well known that matter and antimatter particles, which have equal mass but all additive quantum numbers opposite (e.g. the electric charge), are always observed being created in pairs [7]. In other words, energy can transform into matter only when the latter is accompanied by its counterpart antimatter. The opposite holds true as well: when a particle and its antiparticle are brought together, they annihilate completely into energy. However, the universe we observe is entirely made of matter and there is no significant amount of detectable baryonic antimatter [8], even though our theoretical models expected that equal amounts of both should have been formed in the Big Bang [9].

1.2.1 Brief history of antimatter theory, experiments and production

The possibility of the existence of “antiparticles” was initially discussed by Sir F. A. F. Schuster in two letters to the journal *Nature* in 1898 [10]. He hypothesized the existence of antiatoms and entire solar systems made of antimatter, with the property of yielding energy when combined with “regular” atoms. However the mathematical formulation and the concept of antimatter that we are familiar with was proposed by P. A. M. Dirac in 1928 [11], by considering the negative energy state solution of the quantum mechanical equation which bears his name [12]. Just two years later, C. Y. Chao with an experiment on hard γ -rays and heavy elements found a much higher absorption coefficient than predicted by the accepted theories, including the Klein-Nishina formula [13]. This anomalous behaviour can be explained by the production of electrons and *positrons* in pairs. Two years later came the direct observation of the positron in a cloud chamber by C. D. Anderson and his study on cosmic radiation [14].

A paper titled “Observation of antiprotons” by O. Chamberlain, E. Segrè et al., members of the Radiation Laboratory of the University of California at Berkeley in the USA,

appeared in the 1 November 1955 issue of *Physical Review Letters* [15]. It announced the discovery of a new subatomic particle, identical in every way to the proton — except its electrical charge was negative instead of positive. A month before the paper appeared, *The New York Times* had put the news on the front page: “New Atom Particle Found” [16]. With the discovery of the antiproton, Segrè et al. had further proof of the essential symmetry of nature, between matter and antimatter. Segrè and Chamberlain were awarded the Nobel prize in physics in 1959 “for their discovery of the antiproton” [17]. It is very complex to produce and store heavy antiparticles like antiprotons and antineutrons. Because of this it is very important to maximise the efficiency of machines such as ELENA by means of accurate models and detailed characterisation.

In 1964, J. Cronin and V. Fitch at Brookhaven National Laboratory in the USA performed an experiment with neutral K-mesons, or *kaons* [18]. They started with two types of kaon that had seemingly identical masses but different lifetimes. Kaons of the long-lived type exist for 5.2×10^{-8} s before each decays into three pions. Kaons of the short-lived type exist for only 0.89×10^{-10} s before each decays into two pions. Cronin and Fitch shot the two types of kaon down a 17 m beam line and detected the resulting pion-decays at the other end. Given the different lifetimes of the kaon types and the length of the beam line, you would expect only to see decays from the long-lived kaon type at the detector. Cronin and Fitch anticipated that the short-lived kaons would decay long before reaching the end of the beam line, and so their decay products would not be detected. Specifically you would expect to detect only three-pion decays and no two-pion decays at all. But in their experiment, Cronin and Fitch did detect two-pion decays. In total 45 two-pion decays were observed in 22,700 events — a ratio of 1 in 500. This showed that kaons transform into their antiparticles (composed of the corresponding antiquarks) and vice versa, but that such transformation does not occur with exactly the same probability in both directions. The result violated a fundamental principle of physics called charge conjugation parity symmetry (or CP)—the symmetry between matter and antimatter. They shared the 1980 Nobel prize in physics “for the discovery of violations of fundamental symmetry principles in the decay of neutral K-mesons” [19]. In 1967 Sakharov showed that CP violation is part of a possible reason why the universe is made of matter rather than equal amounts of matter and antimatter. He proposed a set of three necessary conditions that a baryon-generating interaction must satisfy to produce matter and antimatter at different rates [20]. The three necessary “Sakharov conditions” are:

- Baryon number B violation.
- C-symmetry and CP-symmetry violation.

- Interactions out of thermal equilibrium. This means that the rate of a reaction which generates baryon-asymmetry must be less than the rate of expansion of the universe. In this situation the particles and their corresponding antiparticles do not achieve thermal equilibrium due to rapid expansion hence decreasing the occurrence of pair-annihilation.

CP violation is also predicted to occur in the leptonic sector, for example in the oscillations of neutrinos and anti-neutrinos [21]. Although experiments are ongoing, no observations have been made [22, 23]. If discovered, CP violation in neutrinos could also be part of the Sakharov mechanism [24]. Another possibility to generate a baryon asymmetry rests on CPT violation, that is violation of the combined CP and Time Reversal Symmetry (T) [25].

To shed light onto the possible mechanism responsible of the baryon asymmetry we need to create and study atoms of anti-hydrogen, the bound state of an antiproton and a positron, the most stable bound state of pure antimatter that presently can be produced in laboratories. Further its matter counterpart, the hydrogen atom, is the most abundant, simple and well-understood atom in the universe from both theoretical and experimental perspectives [26]. Its spectrum has been measured to very high precision and by comparing its properties and transitions with antihydrogen it is possible to understand if they obey the laws of physics in the same way. For this purpose the Low Energy Antiproton Ring (LEAR) was created at CERN in Geneva, Switzerland [27]. In 1995 the PS196 experiment at LEAR became the first experiment to successfully create and detect atoms of antihydrogen [28], beating the E862 experiment at Fermilab in Chicago, USA, which also successfully created antihydrogen atoms in 1997 [29]. However, these antihydrogen atoms were extremely energetic and therefore not suitable for precision studies of the properties of antihydrogen to be compared with those of hydrogen. For such investigations, it is essential to have trapped and cold antimatter atoms at rest.

1.3 The antiproton production and deceleration chain at CERN

The production of antiproton beams at CERN starts with protons accelerated in a linear accelerator, the so-called Linac4 which replaced Linac2 during CERN's Second Long Shutdown(LS2) [30]. The proton source is a bottle of negative hydrogen ions at one end of Linac4. By the time they reach the other end, the H^- have reached the energy of 160 MeV. The ions are then injected horizontally into the Proton Synchrotron Booster (PSB) by means of a charge-exchange injection system, where a stripping foil

converts the ions into protons [31]. The PSB, the next step in CERN's accelerator chain, takes the obtained proton beam to a higher energy. The PSB is composed of four superimposed synchrotron rings that accelerate the proton beam to 2 GeV for injection into the Proton Synchrotron (PS).

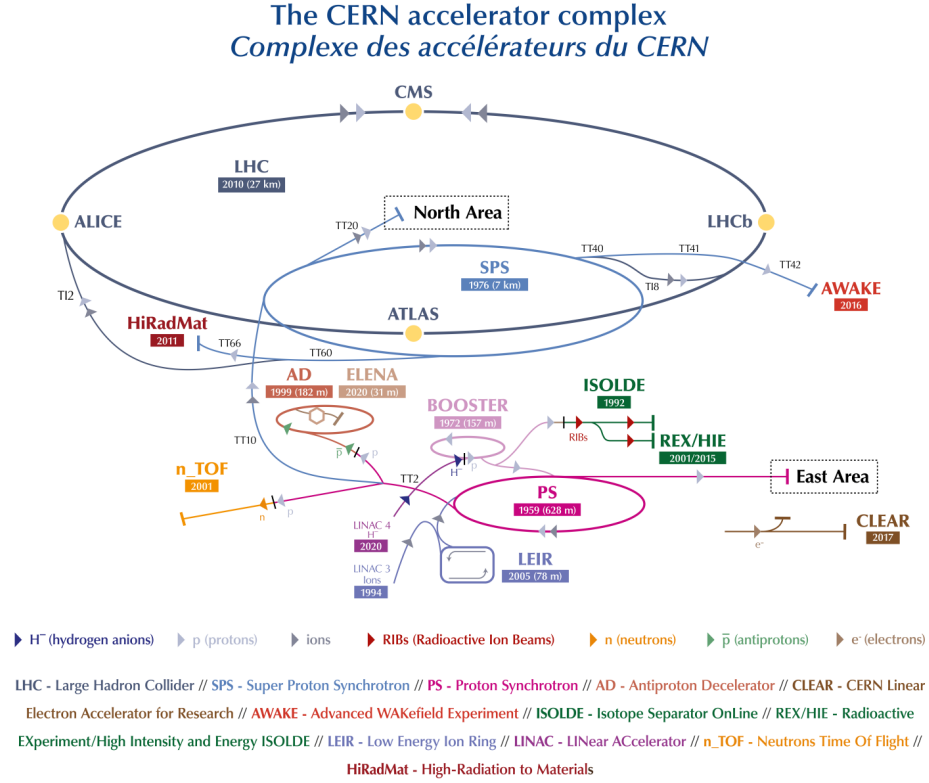


FIGURE 1.1: CERN accelerator complex [32].

With a circumference of 628 m, the PS has 277 conventional (room-temperature) electromagnets, including 100 combined function dipoles to bend the beam round the ring. The accelerator operates from 2 to 26 GeV. The highly energetic beam of protons is fired onto an iridium target [33], which is a very dense and corrosion-resistant metal. The high energy collision of the proton beam with the atoms of the target creates a shower of secondary particles, and among which are antiprotons. The generated antiprotons are collected downstream by magnetic focusing, after which they are selected and magnetically transported via the injection line to the Antiproton Decelerator (AD) [34]. Only a fraction of the produced particles have the right energy to be injected into and stored in the AD, therefore many of the antiprotons are lost. The AD is a 182.4 m long ring and the world's only source of low energy antimatter. It has been operational since the year 2000. In contrast to other machines at CERN which accelerate particles to high energies, the AD slows them down. The AD's bending and focusing magnets keep the antiprotons on the same trajectory, while strong electric fields decelerate them. Sideways motion

and spread in energies are reduced by electron and stochastic cooling [35]. Eventually, antiprotons are slowed down to 10% of the speed of light and the lowest possible beam energy that can be achieved is 5.3 MeV. The antimatter production chain is part of the CERN accelerator complex depicted in Fig. 1.1. Before the introduction of the ELENA ring, antiprotons were sent directly to the experiments. Most of the experiments need antiprotons with a kinetic energy of 3–5 keV, which is significantly lower than what the AD can achieve. Because of this, experiments used sets of degrader foils to further decelerate the antiprotons [36]. Unfortunately, such a method is very inefficient and 99% of antiprotons are lost.

1.4 The Extra Low ENergy Antiproton storage ring

ELENA is a 30.4 m magnetic synchrotron ring designed to further decelerate the antiprotons supplied by the AD from 5.3 MeV down to 100 keV and deliver them to the experiments. Figure 1.2 shows the schematic layout of the ring.

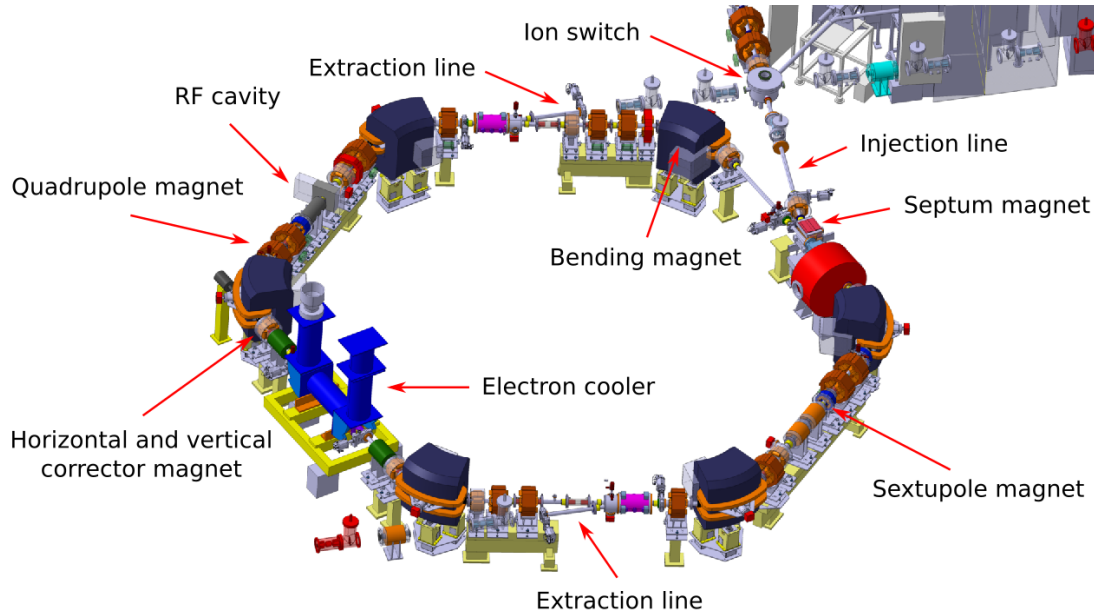


FIGURE 1.2: 3D sketch of the ELENA ring and its components.

Most of the challenges and possible issues of the ELENA project are a consequence of its low energy, small size and low intensity. Figure 1.3 shows the ELENA lattice functions calculated with MAD-X [37]. The low beam energy makes the beam very sensitive to perturbations such that even the Earth's magnetic field has a significant impact. The circumference of the machine has therefore been chosen to be as small as possible, thus demanding higher-field magnets, to mitigate these effects. On the other hand, the ring

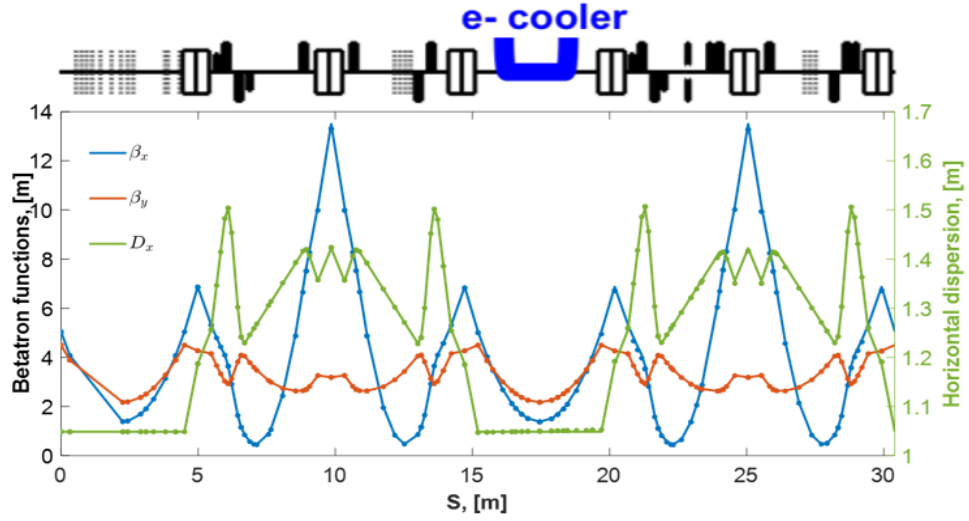


FIGURE 1.3: Optical functions of ELENA combined with horizontal dispersion at the nominal working points ($Q_x = 2.3, Q_y = 1.3$). Solid lines represent values from single particle dynamics and dot values were obtained from bunch tracking.

had to be long enough to install all necessary components. The main parameters for ELENA operations are listed in Table 1.1.

The additional deceleration in ELENA will allow the experiments to increase their antiproton capture capabilities by one to two orders of magnitude. Furthermore, ELENA will provide beam almost simultaneously to all experiments in the AD hall, which as a result will significantly increase the integrated beam time for each experiment. The ring was installed in 2015 and its commissioning came to an end at the start of CERN Long Shutdown two (LS2) in November 2018. ELENA is situated inside the circumference of the AD and receives 5.3 MeV antiprotons through a magnetic transport line. The antiprotons are decelerated in two stages. Electron cooling on an intermediate plateau is applied to reduce emittances and losses during deceleration to the final energy. Once the final energy is reached, electron cooling is applied again to generate dense bunches with low emittances and energy spread, which are then transported to the experiments. At the final energy, so-called intra-beam scattering (IBS) caused by Coulomb interactions between different particles in the beam that increases the beam emittances and the energy spread, which, in turn, increases the beam size. This phenomenon is the dominant source of beam degradation in ELENA, and the equilibrium between IBS and electron cooling determine the characteristics of the bunches sent to the experiments.

The improved availability of trapped antiprotons will allow experiments to greatly improve measurement statistics and achieve meaningful results in a shorter time frame. Currently the AD beam time is divided by experiments in eight hour shifts whereas

ELENA will be capable of distributing four bunches amongst four experiments per AD shot, allowing for almost continuous beam time.

TABLE 1.1: ELENA parameters [3].

Particle	Antiproton
Ring Circumference (m)	30.4
Energy (MeV/u)	5.3–0.1
Relativistic β_{rel}	0.106–0.015
Revolution frequency (MHz)	0.166–0.024
Vacuum (Torr)	3×10^{-12}
Intensity (Charges)	2×10^7
Tunes	$Q_H = 2.3, Q_V = 1.3$

1.4.1 Antimatter experiments in the ELENA era

Several antimatter experiments investigate whether CPT invariance and the WEP (weak equivalence principle) hold. The systems probed are antihydrogen, antiprotonic helium and individual antiprotons. In this section an overview of the experiments located at the AD hall are given highlighting the increased efficiency with the introduction of ELENA in the antiproton accelerator chain. Figure 1.4 shows the plan of the AD hall, including ELENA and the experimental areas. The ALPHA [38], ASACUSA [39] and BASE [40] experiments are primarily focused on precision tests of CPT symmetry comparing antimatter with matter. Any deviation in a property of antimatter from the same property in matter, e.g. the resonance frequency of the 1S to 2S spectroscopy in (anti)hydrogen, would immediately indicate CPT symmetry violation [41]. The AEgIS [42], ALPHA-g [43] and GBAR [44] experiments instead pursue tests of the WEP by determining the sign and absolute value of the gravitational acceleration g of antimatter in the Earth's gravitational field. So far no conclusive direct test of the WEP has been carried out, so it cannot be excluded that an antibaryon-antilepton system like antihydrogen may break CTP invariance and WEP.

AEgIS

The AEgIS (Antimatter Experiment: Gravity, Interferometry, Spectroscopy) experiment is designed to test the WEP with antimatter by studying the free fall of antihydrogen in the Earth's gravitational field. In the first phase of the experiment, the AEgIS team is using antiprotons from the AD together with a pulse of laser-excited positronium atoms (obtained by shooting positrons onto a nano-structured target [45]) to make a

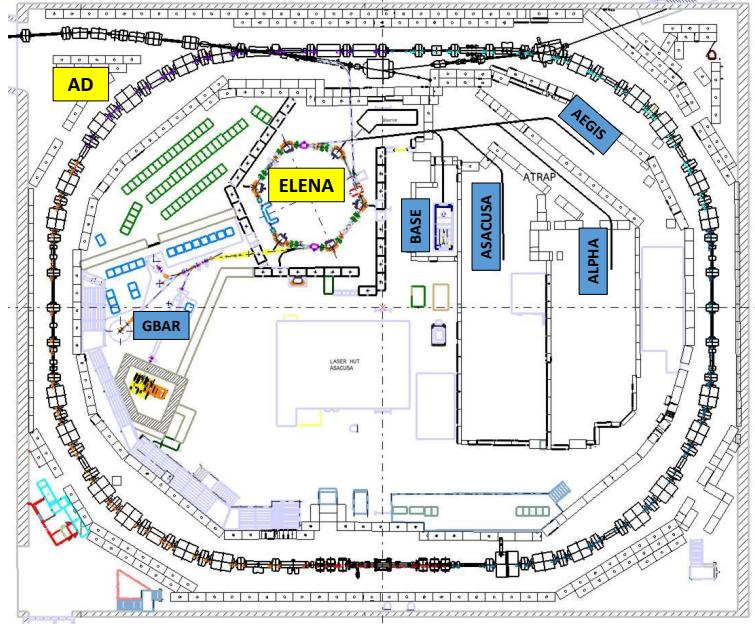


FIGURE 1.4: ELENA in the AD Hall and the beam lines transporting the antiprotons to the different experiments.

pulse of horizontally-travelling antihydrogen atoms. They then pass the antihydrogen beam through an instrument called a Moire deflectometer coupled to a position-sensitive detector to measure the strength of the gravitational interaction between matter and antimatter to a precision of 1%. A system of gratings in the deflectometer split the antihydrogen beam into parallel rays, forming a periodic pattern. From this pattern, the physicists can measure how much the antihydrogen beam drops during its horizontal flight. Combining this shift with the time each atom takes to fly and fall, the AEGIS team can then determine the strength of the gravitational force between the Earth and the antihydrogen atoms. The operation of ELENA will allow the number of trappable antiprotons to be increased by more than a factor of 50. For the antihydrogen production scheme chosen by AEGIS, this will be reflected in a corresponding increase of produced antihydrogen atoms, leading to a significant reduction of measurement times and providing a path towards high-precision measurements.

ALPHA

The ALPHA (the Antihydrogen Laser Physics Apparatus) experiment is a successor of an earlier antimatter experiment, ATHENA [46]. Set up in late 2005 with similar overall research goals as its predecessor, ALPHA makes, captures and studies atoms of antihydrogen and compares these with hydrogen atoms. The simple hydrogen atom is hugely significant in fundamental physics, underpinning the modern atomic picture.

Its spectrum is characterised by well-known spectral lines at certain wavelengths, corresponding to the emission of photons of a certain frequency when electrons jump between different levels [47]. Measurements of the hydrogen spectrum agree with theoretical predictions at the level of a few parts in a quadrillion (1×10^{15})—a stunning achievement that antimatter researchers have long sought to match for antihydrogen. Comparing such measurements with those of antihydrogen atoms tests a fundamental symmetry of CPT invariance. The ALPHA team makes antihydrogen atoms by taking antiprotons from the AD and binding them with positrons from a sodium-22 source. Next it confines the resulting antihydrogen atoms in a magnetic trap, which prevents them from coming into contact with matter and annihilating. Laser light is then shone onto the trapped antihydrogen atoms, their response measured and finally compared with that of hydrogen. Thin foils of material are used to slow down and trap antiprotons in a Penning-Malmberg trap [48], where they can be used for antihydrogen creation and measurements. The reduced initial kinetic energy of the beam coming from ELENA will increase the percentage of trappable antiprotons by up to two orders of magnitude.

ALPHA-g

The ALPHA experiment has recently entered an expansion phase of its experimental studies, driven in part by the expected benefits of conducting experiments in the framework of the new AD+ELENA antiproton facility. ALPHA-g is very similar to the ALPHA experiment, extending the physics programme to include a measurement of antimatter gravitation. The goal is to perform a precise measurement of antimatter gravitational acceleration with the aim of achieving a test of the WEP at the 1% level. ALPHA-g, will be an additional atom-trapping apparatus located at the ALPHA experiment. It consists of the same type of apparatus for making and trapping antiatoms, except that it is oriented vertically. With this vertical setup, the ALPHA-g collaboration can precisely measure the vertical positions at which the antihydrogen atoms annihilate with normal matter once the traps magnetic field is switched off and the atoms are under the sole influence of gravity. The values of these positions will allow them to measure the effect of gravity on the antiatoms. With the introduction of ELENA, the increased 24h beam availability to experiments is critical in enabling operation on multiple fronts: spectroscopic measurements and the focus on gravitational acceleration in tandem, advancing the knowledge base on antimatter.

ASACUSA

This experiments approach is different as ASACUSA is able to create very special hybrid atoms made of a mix of matter and antimatter: these are the antiprotonic helium atoms composed of an antiproton and an electron orbiting a helium nucleus. They are made by mixing antiprotons with helium gas. In this mixture, about 3% of the antiprotons replace one of the two electrons of the helium atom. In antiprotonic helium, the antiproton is in orbit around the helium nucleus, and protected by the electron cloud that surrounds the whole atom, making antiprotonic helium stable enough for precision measurements. By using lasers to excite the antiproton from one orbit to another and precisely measuring the atom's transition frequencies, and comparing the results with quantum-electrodynamics (QED) calculations, ASACUSA tests CPT through a precise determination of the antiproton-to-electron mass ratio. The consistency of the fundamental matter-antimatter symmetry has been so far tested to a precision below 1 part-per-billion. The ASACUSA collaboration also intends to measure the ground state hyperfine splitting of antihydrogen (the energy difference between the two states with parallel and antiparallel electron and proton spins [49]). The hydrogen ground state hyperfine splitting of about 1.42 GHz had been measured very accurately with a relative precision of about 1 part in 10^{12} . It was also determined recently by ASACUSA, albeit with a more modest precision of a few parts per billion [50] in a hydrogen beam by using the Rabi resonance method, which will also be applied to determine the hyperfine transition frequency of antihydrogen. Positrons are obtained from a sodium-22 source and stored in the positron accumulator. Together they form antihydrogen in the mixing trap. The neutral antihydrogen atoms escape the trap and get spin polarised by the strong magnetic field gradients of the CUSP trap. Low-field seekers enter the spectrometer consisting of a microwave cavity—to induce hyperfine transitions—and an analysing sextupole magnet. The force from magnetic field gradients exerted on the magnetic moments separates the antihydrogen atoms according to their spin states (Stern-Gerlach effect [51]), the sextupole magnet focusing the low-field seeking states and defocusing the high-field seekers. A detector records the annihilation signal at the end of the beam line, as a function of microwave frequency. Additionally the ASACUSA collaboration has built a beam of cold atomic hydrogen with the initial aim to test the components of the antihydrogen hyperfine spectroscopy line. The operation of the antihydrogen hyperfine spectroscopy apparatus is a basic prerequisite for the proposed CPT test and it requires a careful characterization of every component of the experiment, which can be done with hydrogen (with the obvious exception of the annihilation detector). The setup can be also used to investigate a possible dependence of the hyperfine transition frequencies on the orientation of the external magnetic field, which will constrain some

coefficients of the non-minimal Standard Model Extension that have never been determined experimentally [52]. The ELENA will provide a lower beam energy and a higher beam availability which will be beneficial to the ASACUSA experiment on three fronts: a higher number of low energy antiprotons, a round-the-clock antiproton availability which will avoid the daily time consuming beam-tuning through the ASACUSA components and a separate beam line for the second ASACUSA activity, sparing the bi-annual disassembly and assembly of the entire apparatus and therefore allowing for necessary developments throughout the year. With the lower energy and emittances of the ELENA antiproton beam, the antiprotonic helium would then be formed in a smaller volume, so that lasers of lower power and higher precision could be used in the experiments. The high stability of the antiproton beam should ensure a high signal-to-noise ratio on the antiprotonic helium spectral lines. By using this high-quality antiproton beam and new diode-pumped solid-state lasers, the precision of the laser spectroscopy experiments may be improved to approximately 10^{-10} .

BASE

The Baryon Antibaryon Symmetry Experiment (BASE) [40] compares the magnetic moments of protons and antiprotons to look for differences between matter and antimatter. Using an experimental setup with two Penning traps—devices that hold particles in place with electromagnetic fields—the team aims to measure the antiproton magnetic moment to a hitherto unreachable part-per-billion precision. A direct measurement of the magnetic moment requires the measurements of two frequencies: the Larmor frequency, which characterizes the precession of the spin of a particle, and the cyclotron frequency, which describes a charged particles oscillation in a magnetic field. BASEs double Penning trap separates the measurements of the Larmor as well as the cyclotron frequency from the spin-state analysis. Two traps are used for the measurements: the analysis trap which will identify the spin state of the particle and the precision trap which will flip the spin of the particle while measuring the cyclotron frequency. Two further traps are used. The monitor trap will check for any variance in the magnetic field caused by external sources, allowing the BASE team to make instant adjustments to the core traps while measurements are under way. The reservoir trap will store antiprotons for months on end, allowing the BASE collaboration to continue operating even without beam. With the introduction of the ELENA ring in the antiproton cycle and after the successful implementation of the double-trap method, fractional precisions on the parts per billion level will be reached, with the potential to be further improved by at least a factor of ten. Highly stabilized superconducting trap magnets together with elegant phase-sensitive detection techniques applied to measure the proton/antiproton

oscillation frequencies will allow further reduction of the resonance line-widths. The implementation of sympathetic cooling of antiprotons by coupling the particles to laser-cooled Be^+ ions using a common endcap method [53] or by direct Coulomb coupling in a micro-fabricated Penning trap [54], which are currently being prepared by collaboration members of BASE, will enable measurements at an improved rate. Combining all these techniques magnetic moment measurements at the ten part-per-trillion level will become possible, in the long term.

GBAR

The GBAR project (Gravitational Behaviour of Antimatter at Rest), aims to measure the free fall acceleration of ultracold neutral antihydrogen atoms in the terrestrial gravitational field. It is a direct test of the WEP for antimatter. The experiment first combines the antiprotons with two positrons, to form antihydrogen ions with a positive charge. Although more difficult to produce than the simpler antiatoms, the antimatter ions can be more easily manipulated. Using laser-cooling techniques, these ions are brought to μK temperatures before they are stripped of the additional positron, transforming them into antihydrogen atoms. These antihydrogen atoms are then allowed to fall from a height of 20 cm and their annihilation at the end of the fall is recorded. The first step of the experiment is to produce an antihydrogen ion $\bar{\text{H}}^+$ and catch it in a Paul trap, where it can be cooled to μK temperature using ground state Raman sideband sympathetic cooling. The μK temperature corresponds to a particle velocity in the order of 1 m/s. Once such velocity is reached, the antihydrogen ion can be neutralised and starts to fall. Due to the low temperature, a fall from 10 cm height corresponds to approximately a 0.14 s time of flight. Such a long free fall allows achieving 37% error on the measurement of the gravitational acceleration \bar{g} for antihydrogen after only one event. With this method, the aim is to reach 1% precision with about 1500 events [55]. GBAR aims to test the so-called Equivalence Principle put forth by Albert Einstein, which states that the trajectory of a particle is independent of its composition and internal structure when it is only submitted to gravitational forces. Observing a difference in the way hydrogen and antihydrogen fall under gravity would demonstrate that this principle is violated. The second goal of the experiment is to reach 10^{-5} – 10^{-6} precision in the measurement of the gravitational quantum states of cold antihydrogen.

GBAR is the first experiment which has been connected to the ELENA ring. The first antiproton beam reached the experiment in June 2018 and was tested until November 2018. This beam gets further deceleration to 1–10 keV energy in order to obtain the highest possible $\bar{\text{H}}^+$ formation rate. Still, given the expected number of order 5×10^6

low energy antiprotons available per burst, a high density of 10^{12} cm^{-3} of positronium is necessary to produce one $\bar{\text{H}}^+$, making the role of ELENA essential for the operations.

1.5 Project goals and overview

The primary goal of this project is the characterisation and optimisation of beam quality for extra low energy antiproton beams in presence of electron cooling. The bulk of this thesis is an in depth analysis of relevant effects acting on low energy beams and electron cooling and their correct implementation into simulation tools.

Chapter 2 introduces the underlying theoretical concepts used for this work. In Chapter 3 the model used for the simulations is described in detail focusing on the cooling force and the heating effects relevant for low energy storage rings. Chapter 4 presents the simulation tools used for the beam dynamics studies and its algorithms. The model and simulation programs are then tested and benchmarked against data taken at the Low Energy Ion Ring (LEIR) in Chapter 5. The simulation results for ELENA are discussed in Chapter 6, including a few supporting measurements. Finally Chapter 7 gives a summary of the work presented in the previous chapters.

The work described here is done in the context of the ELENA ring, but is generally of interest for future low energy ion and antimatter facilities. For example, the Facility for Low-energy Antiproton and Ion Research (FLAIR) is a future addition to the Facility for Antiproton and Ion Research (FAIR) [56, 57]. FAIR is currently under construction at the GSI Helmholtz Centre for Heavy Ion Research in Darmstadt with FLAIR proposed as a phase 2 upgrade [58]. Furthermore the simulation model and new implemented components for simulating the transport of extra low energy antiprotons and ions may also be built upon and adapted for future experimental, commercial and medical facilities in the future.

Chapter 2

Theoretical Background

This chapter presents the basic concepts and relevant theories in the field of particle beams and accelerators. This branch of physics examines the motion of charged particles in electric and magnetic fields. The main focus of the chapter is to introduce the fundamental quantities and effects required to model electron cooling and for the derivation of the cooling force.

2.1 Beam Dynamics

Particle beams are used to explore matter at the molecular, atomic and subatomic level. Accelerators were invented in the 1930s to provide high-energy particles to investigate the structure of the atomic nuclei. Since then, high-energy accelerators have led to the discovery of the fundamental building blocks of the universe and the exploration of the forces acting between them. More than 30,000 accelerators are currently used to diagnose and treat cancer as well as other diseases [59], improve manufacturing processes [60], in addition to study energy, environmental and security issues [61–63]. Beam dynamics describes the physics underpinning the behaviour of particles inside accelerators. The fundamental problem is to represent the motion of charged particles through the electric and magnetic fields in an accelerator on the transverse and longitudinal plane, taking into account the impact of interactions between the particles within the beams. The discipline combines electromagnetism, special relativity, classic mechanics and non-linear physics.

2.1.1 Co-ordinate System

We consider two co-ordinate systems when describing a beam traversing an accelerator or transport line. In both systems the transverse plane is described by the horizontal co-ordinate x and the vertical position co-ordinate y . In all accelerators there is a single ideal path taken by a hypothetical perfectly centred particle with the design momentum and no initial divergence known as the reference particle. The path it traces out through the machine is called the closed orbit in the case of a ring (since it ends exactly where it began) or the reference orbit for a linear machine. This path defines $x = 0$, $y = 0$ and $z = 0$ along the machine.

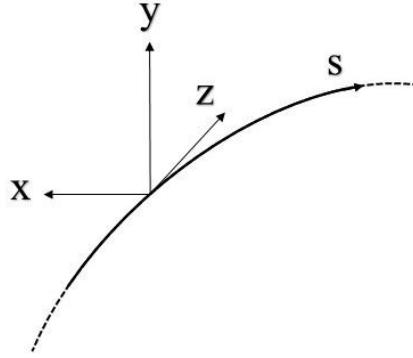


FIGURE 2.1: Curvilinear co-ordinate system applied in synchrotrons. x and y specify the transverse distance from the design orbit, z the longitudinal offset

In the frame of reference which travels with the reference particle, we define a co-moving system x, y, z where the z component describes a particles longitudinal offset from the reference particle. When considering a beams position around a ring or along a transport line we may use x, y, s where s defines a distance along or around the machine from some arbitrary point, $s = 0$. Typically $s = 0$ will be at the injection point or the start of a beam transfer line and follows the path of the reference particle. It should be noted that z is a curvilinear co-ordinate and is always parallel to the reference particles closed orbit, as illustrated in Fig. 2.1. Each particle of the beam may be described at any single point along s by a set of six phase space co-ordinates

$$(x, x', y, y', z, \delta), \quad (2.1)$$

where $x' = \frac{dx}{ds} = \frac{p_x}{mc\beta_{rel}\gamma_{rel}}$, $y' = \frac{dy}{ds} = \frac{p_y}{mc\beta_{rel}\gamma_{rel}}$ with p_x and p_y the components of the transverse momentum, m the mass of the particle, c the speed of light in vacuum, β_{rel} the relativistic velocity as a fraction of the speed of light and γ_{rel} the Lorentz factor

$1/\sqrt{1 - \beta_{rel}^2}$. $\delta = \frac{p_i - p_0}{p_0}$, with p_i as the momentum of the particle and p_0 as the design momentum, δ is known as the longitudinal momentum offset.

2.1.2 Transverse Beam Dynamics

The basic expression for the particle trajectories, having the design momentum p_0 (i.e. $\delta = 0$), under the influence of the focusing properties of the quadrupole and dipole fields are the so-called Hill's equations [64]

$$x''(s) + K_x(s)x(s) = 0, \quad (2.2)$$

$$y''(s) + K_y(s)y(s) = 0. \quad (2.3)$$

The parameter K combines the focusing strength k of the quadrupole and the weak focusing term $1/\rho^2$ of the dipole field. (Note that by convention a negative value of k is a horizontal focusing magnet.) The value of K in the horizontal and vertical planes is given by $K_x(s) = \frac{1}{\rho^2(s)} - k(s)$ and $K_y(s) = k(s)$. They are periodic functions of the s -coordinate due to the orbit being a closed curve: $K_{x,y}(s) = K_{x,y}(s + C)$ where C is the circumference of the machine.

2.1.3 Transverse Emittance

Emittance is the property of a particle beam that characterizes its phase space area. It is used to describe a beam because unlike the physical dimensions of the beam, which vary with location in an accelerator, emittance is invariant in the absence of dissipative or cooling forces [65]. The general solution of the equations 2.2 and 2.3 for the single particle transverse position (as a function of s , the longitudinal location) is the following

$$x(s) = \sqrt{\varepsilon} \sqrt{\beta(s)} \cos(\varphi(s) + \varphi_0), \quad (2.4)$$

$$x'(s) = -\sqrt{\frac{\varepsilon_x}{\beta_x(s)}} (\alpha_x(s) \cos(\varphi(s) - \varphi_0) + \sin(\varphi(s) - \varphi_0)). \quad (2.5)$$

The position and angle of the transverse oscillation of a particle at a point s are given by the value of the so-called beta function $\beta(s)$ which varies around the ring as a result of the focusing properties of the accelerator elements. In any case, like the lattice itself, it has to fulfil the periodicity condition

$$\beta(s + L) = \beta(s). \quad (2.6)$$

Inserting the solution 2.4 into the Hill's Eq. 2.2 and rearranging, we get

$$\varphi(s) = \int_0^s \frac{ds}{\beta(s)} \quad (2.7)$$

which describes phase advance of the oscillation between point 0 and s in the lattice. It should be emphasized that φ depends on the amplitude of the particle oscillation. At locations where $\beta(s)$ reaches large values, i.e., the beam has a large transverse dimension, the corresponding phase advance will be small; and vice versa, at locations where we create a small $\beta(s)$ in the lattice, we will obtain a large phase advance. The number of oscillations that the particle performs per turn in each plane are known as the horizontal and vertical tunes of the lattice which may be calculated by integrating Eq. 2.7 around the ring

$$Q_{x,y} = \frac{1}{2\pi} \oint_C \frac{1}{\beta_{x,y}(s)} ds \quad (2.8)$$

where C is the circumference of the ring [66].

We define the horizontal emittance by combining the Hill's equations solution for x and x' to get

$$\varepsilon_x = \gamma_x(s)x^2 + 2\alpha_x(s)x(s)x'(s) + \beta_x(s)x'(s)^2. \quad (2.9)$$

Here we follow the usual convention in the literature and introduce the two parameters [65]

$$\alpha = -\beta'_x(s)/2, \quad (2.10a)$$

$$\gamma_x = \frac{1 + \alpha^2(s)}{\beta_x} \quad (2.10b)$$

called the alpha and gamma function respectively and together combined with beta these are known as the Twiss parameters [65].

Plotting Eq. 2.9 gives an ellipse which a particle will trace out in phase space when measured many times at a given position s around the lattice. The ellipse will be centred around the closed orbit of the beam (x_0 or y_0) and has the properties shown in Fig. 2.2. As a particle moves through the machine the ellipse will change shape yet the area $\pi\varepsilon_{x,y}$ will remain constant as long as conservative forces are considered. The conservation of emittance around the machine is known as Liouville's theorem [65] and applies only for a closed system, where the energy is constant.

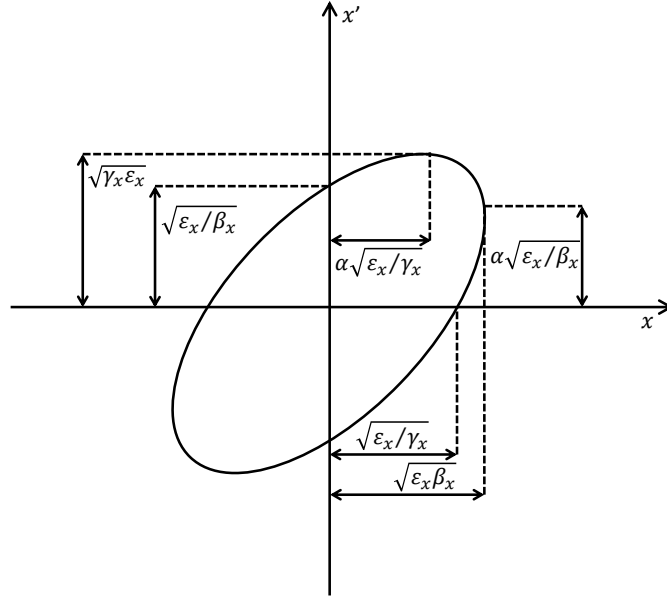


FIGURE 2.2: Properties of the horizontal phase space ellipse.

In an accelerator a beam is made up of a number of particles all with different coordinates and momentum offsets. Typically it is the case that the distribution of these two quantities can be approximated by Gaussian distributions [67]. The overall emittance of a beam must be defined by how much of the beam distribution is being considered. For example, the phase space area of the 95% emittance contains 95% of the particles in the distribution. Here the RMS (root mean square) definition is used where we consider the area containing one standard deviation of the beams particles. We may compute the statistical RMS emittance of a distribution of particles using

$$\varepsilon_x = \sqrt{\langle x^2 \rangle \langle x'^2 \rangle - \langle x x' \rangle^2}, \quad (2.11)$$

where $\langle \dots \rangle$ denotes the weighted averages and are the second order moments of the beam. Units of emittance for machines like ELENA are typically given in mm mrad. The momentum spread of the beam σ_δ is defined as the RMS width of the momentum offset distribution and in unitless as is δ .

2.1.4 Longitudinal Momentum Spread

Until now we have treated the beam and the equations of motion as a mono-energetic problem. Unfortunately, in the case of a realistic beam, we have to deal with a considerable distribution of the particles in energy/momentum

$$\frac{\Delta p}{p} = \delta \neq 0. \quad (2.12)$$

This momentum spread will lead to several effects notably in the bending of the dipole magnets and the focusing strength of the quadrupoles. An on-axis yet off-momentum particle will have some modified divergence x' after a sector bend due to its exit angle being slightly different from the design angle for the reference momentum p_0 . The equation of motion, which was a homogeneous differential equation until now, will have a non-vanishing term introduced on the right hand side. We must then rewrite Eq. 2.4 as [64]

$$x''(s) + K_x(s)x(s) = \frac{\delta}{\rho(s)}. \quad (2.13)$$

The orbit of the particle is now adjusted and so we redefine the original on-momentum co-ordinate as the betatron position x_β , which traces out the phase space ellipse. It is possible then to define a new closed orbit around which a hypothetical particle of $\delta = 1$ would follow. This path is referred to as the dispersion function and denoted by $D(s)$. It should be noted that in reality particles with $\delta = 1$ would be immediately lost in the machine. $D(s)$ is a property of the lattice and is usually accounted for in the design of the machine. A particle with some small δ would then have a position

$$x(s) = x_\beta(s) + D_x(s)\delta. \quad (2.14)$$

at some point s along the machine. The dispersive term $D_x\delta(s)$ causes a shift in the horizontal position of the ellipse traced out by x_β . The quantity $x_\beta(s) + D_x(s)\delta$ may be thought of as the momentum-dependent closed orbit of a particle. In the case of a Gaussian beam the emittance at any point along s may be estimated from the RMS beam widths $\sigma_{x,y}$ with

$$\varepsilon_x = \frac{\sigma_x^2}{\beta_x} - \frac{\sigma_\delta^2 D_x^2}{\beta_x}, \quad (2.15)$$

$$\varepsilon_y = \frac{\sigma_y^2}{\beta_y}. \quad (2.16)$$

The dispersive effects in the horizontal plane are accounted for by the second term. From these equations it is clear to see that the RMS beam width varies as a function of $\beta_{x,y}$ (noting that $\varepsilon_{x,y}$ is constant in absence of cooling and heating effects).

2.2 Heating Effects

The beam in ELENA is decelerated from the injection energy of 5.3 MeV to an extraction energy of 100 keV in two stages (see Fig. 2.3) to allow for an intermediate cooling plateau at 650 keV [68]. The adiabatic blow up of the beam is inversely proportional to the change in momentum of the beam.

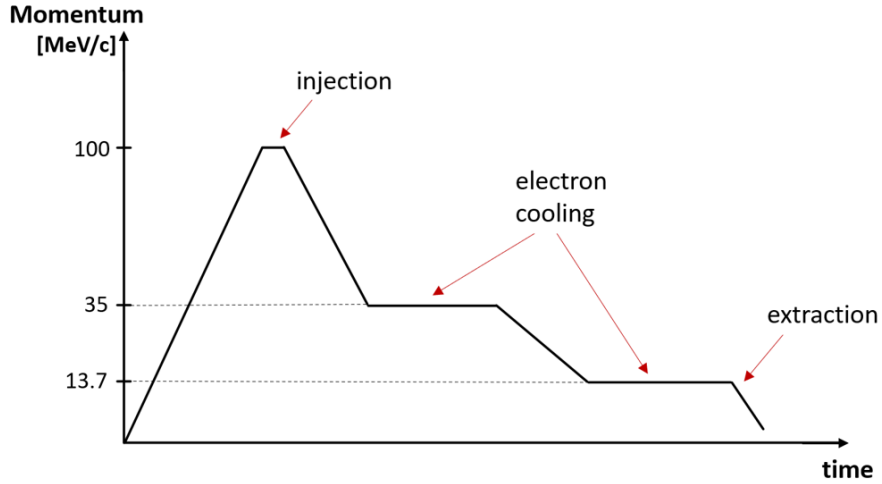


FIGURE 2.3: Example of a typical ELENA cycle.

The particle beam can be considered as an ion plasma circulating in the storage ring [69]. Its temperature is defined as the energy spread of the ions in the frame moving with the particles and is a measure of the beam quality (with lower temperature corresponding to higher quality). Interactions with targets and rest gas, IBS and space-charge effects are examples of processes that heat the ion plasma. Moreover, the lifetime of the beam in a storage ring can be limited by IBS, transverse instabilities, incoherent space charge tune-shifts and resonances. At the low energy region in which ELENA operates, these dispersive effects become significant.

2.2.1 Intrabeam Scattering

IBS is a beam heating effect produced by multiple small-angle Coulomb scatterings of charged particles within the beam itself [70]. It causes an exchange of energy between the transverse and longitudinal planes, leading to the growth of the beam phase space dimensions. This phenomenon places fundamental limitations on the achievable minimum beam emittance in a storage ring [71].

Charged particles within the beam can scatter via Coulomb collision. It is important to distinguish between two cases:

1. large-angle single scattering events
2. multiple small-angle scattering events

Treatment of both kinds of collisions is a well known subject in plasma physics [72]. The effect where particles are lost in a single collision is typically called the *Touschek effect* [73]. In this case the energy transfer from horizontal to the longitudinal direction

is amplified due to relativistic γ . When scattering angles are sufficiently small, random addition of many small-angle collisions causes beam dimensions to grow (similar to diffusion in gas). In circular accelerators, multiple Coulomb scattering (MCS) was first applied to explain emittance growth in electron machines: Bruck and Le Duff in 1965 called it “multiple Touscheck effect” [74], and was later generalized by Piwinski (1974) [70] for proton machines calling it IBS. IBS is well explained in literature with models developed by Piwinski [75], Martini [76] and later by Bjorken and Mtingwa [77]. Beam growth rates due to this effect may be approximated by

$$\frac{1}{\tau_{x,y,p}} \propto \frac{r_p^2 c \lambda}{32 \pi^{3/2} \beta_{rel}^3 \gamma_{rel}^4 \varepsilon_x \varepsilon_y \sigma_\delta}, \quad (2.17)$$

$\beta_{rel} = v/c$ and γ_{rel} is the Lorentz factor. For coasting beams $\lambda = N/C$ and for bunched beams $\lambda = N_b/(2\sqrt{\pi}\sigma_s)$. N is the total number of particles in the beam and N_b in each bunch, σ_s is the bunch length and C is the ring circumference. The speed of light in vacuum is classically represented with c and r_p is the classical proton radius. The inverse dependence on γ_{rel}^4 highlights the significance of this effect for low energy machines where γ_{rel} approaches one and so understanding the magnitude of this effect is crucial at an energy of 100 keV where $\gamma_{rel} = \frac{938+0.1}{938}$.

2.2.2 Space-charge Forces

An ensemble of identically charged particles experiences a Coulomb repulsion, which is commonly known as direct space charge effect. However, if the particles are non-stationary, their movement also constitutes an electric current, which is accompanied by a magnetic field. The charge and current of the beam create self-fields and image fields which alter its dynamic behaviour and influence the single-particle motion as well as coherent oscillations of the beam as a whole. Due to the defocusing force that is caused by the space charge of the beam, the tune of the oscillating particles is changed. This change must be minimized such that tune resonances which can result in beam losses can be avoided. The maximum number N_i of ions that can be stored is determined by the incoherent tune shift ΔQ given by:

$$N_i \approx \frac{A}{Z} \frac{2\pi}{r_p} B_f \beta_{rel}^2 \gamma_{rel}^3 \varepsilon_{x,y} (-\Delta Q_{x,y}), \quad (2.18)$$

$$\Delta Q_{x,y} \approx -\frac{Z}{A} \frac{r_p}{2\pi} \frac{N_i}{B_f \beta_{rel}^2 \gamma_{rel}^3 \varepsilon_{x,y}}, \quad (2.19)$$

where A is the mass number of the ions, Z the charge number, B_f the bunching factor ($B_f = 1$ for coasting beams) and $\varepsilon_{x,y}$ the transverse beam emittances.

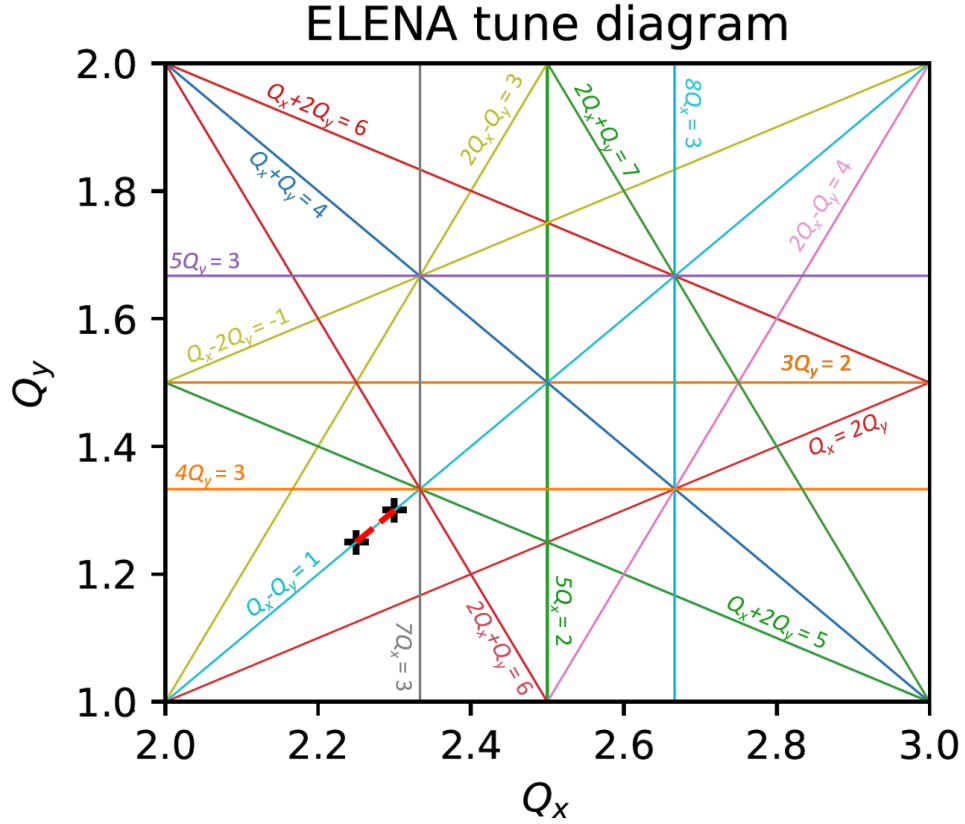


FIGURE 2.4: The ELENA tune diagram showing resonance lines up to third order. The black x marks represent the initial ($Q_x = 2.3, Q_y = 1.3$) and final working points ($Q_x = 2.25, Q_y = 1.25$). The incoherent tune shift is due to the space charge effect at 100 keV for the emittance decrease during electron cooling.

In Fig. 2.4 the tune diagram of ELENA is shown. Resonance lines up to the third order are plotted together with the chosen working point ($Q_x = 2.3, Q_y = 1.3$) and the incoherent tune shift due to space charge forces $\Delta Q = -0.05$ calculated at 100 keV for a beam intensity $N_i = 2 \times 10^7$ and the emittances $\varepsilon_x = 0.55 \text{ mm mrad}$, $\varepsilon_y = 0.53 \text{ mm mrad}$ obtained after cooling. The chosen working points are placed on the coupling resonance $Q_x - Q_y = 1$ and it is observed that the tune shift moves the working points away from the third order resonance lines.

2.2.3 Rest Gas Scattering

The interaction of the beam particles with the molecules of the residual gas (rest gas scattering) may have a detrimental effect at such low energies and leads to stringent vacuum requirements [78]. Beam particles can interact with residual gas molecules through two types of force: the strong and electromagnetic interactions. The first is relevant

only for hadron beams which interact with the nuclei of the residual gas molecules. The strong interaction's range is short, about 10^{-15} m or 1 fm, which is approximately the size of a nucleon. The electromagnetic interaction instead is relevant for all charged beams. The beam can interact with both atomic nuclei and atomic electrons of the residual gas. The strength of the electromagnetic interaction is typically reduced by the factor $\alpha = 1/137$ compared with the strong interaction but has infinite range. At large impact parameter (>1 fm), where the strong interaction becomes inactive, the electromagnetic interaction becomes visible and will be dominated by elastic scattering. This is what causes multiple scattering when a charged particle passes through matter. The emittance growth due to rest gas scattering is usually considered to be caused mainly by MCS. In [79], the RMS transverse emittance (1σ) growth rate due to MCS on residual gas is given by

$$\frac{d\varepsilon_{rms}}{dt} = 2\pi \langle \beta_{\perp} \rangle n_{ms} \ln \left(\frac{280}{\alpha} \right) r_e^2 \frac{(m_e c^2)^2}{\beta_{rel} c p^2} \quad (2.20)$$

with m_e the electron mass, r_e the classical electron radius, α the fine structure constant, $\beta_{rel} = v/c$ the relativistic velocity factor of the beam and p the beam momentum. Here $\langle \beta_{\perp} \rangle = \frac{\langle \beta_x \rangle + \langle \beta_y \rangle}{2}$ represents the average betatron function over the ring and n_{ms} is the multiple scattering density given by the following expression

$$n_{ms} = \sum_i n_i \frac{Z^2 \ln \left(\frac{280}{\alpha (AZ)^{1/3}} \right)}{\ln(280/\alpha)} \quad (2.21)$$

with n_i the density of each residual gas component i in the vacuum pipe. In Eq. 2.20, note that the rate of emittance blow-up due to scattering on the residual gas is independent of the beam intensity and the initial emittance. However, it is strongly momentum dependent ($\propto p^{-2}$), and increases rapidly at lower momenta. But with the extremely low nominal pressure of 4×10^{-12} mbar obtained with a carefully designed ELENA vacuum system [80], at low energies and emittances, rest gas effects are small compared with the dominant performance limitation of IBS. Figure 2.5 shows a comparison between IBS and rest gas scattering growth rates in the horizontal plane. The ELENA vacuum system is based on the NEG-coating technology [81], and a typical residual gas composition of this kind of system was considered in the calculations: 95% H₂, 2% CO, 2% CO₂ and 1% CH₄. As the energy decreases, the growth rate due to rest gas scattering becomes negligible compared to IBS and will not be considered in the rest of this thesis.

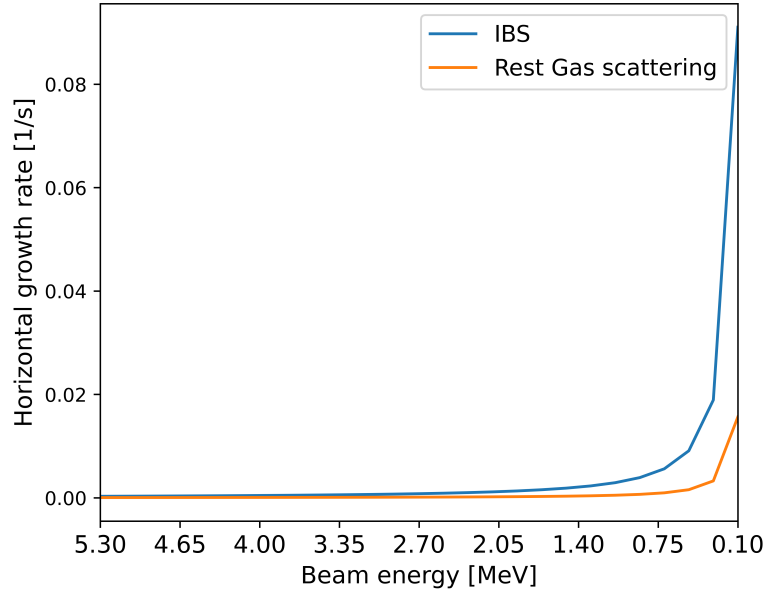


FIGURE 2.5: IBS and rest gas scattering growth rates for ELENA. At 100 keV the IBS effect is dominant.

2.3 Beam cooling

2.3.1 Introduction

The main obstacle for beam focusing is the transverse velocity of the beam caused by the initial temperature leading to thermal motion. As a consequence of Liouville's theorem the momentum spread and the emittance in charged-particle beams cannot be reduced by magnets [82]. Beam cooling can overcome this obstacle. The ability to increase the phase space density that results from the application of cooling methods can be required for many purposes such as accumulation of antiprotons or other particles to increase the beam current or the luminosity in the case of colliders. It is also a very valuable tool when there is a need to counteract heating effects that follow interactions with an internal target or during the deceleration process. Cooled beams are also preferable in the pursuit of improved precision measurements. It is a technique to reduce the energy spread, transverse size and divergence of a charged particles beam. During this process, the particles are compressed into a beam with less energy spread and less angular divergence. It is used to compensate various heating and intensity-limiting effects acting on circulating beam as:

- IBS (discussed previously in sections 2.2.1)
- space charge effects (2.2.2)
- residual gas (2.2.3)

There are various methods to achieve a cooled beam: radiation cooling, electron cooling, stochastic cooling, laser cooling, muon cooling are among them. ELENA, for its design requirements and the low energies at which it operates, uses electron cooling.

2.4 Electron Cooling

One method to cool a plasma is to mix it with a plasma of much lower temperature. This is accomplished by aligning a low temperature electron beam with the ion¹ beam along a straight section in the accelerator. The large mass ratio between ions and electrons makes it possible to accelerate electrons to the same velocity as the ions using a static electric field. The temperature of the electron plasma will then be given by the temperature of the electron source. The technique to cool ion beams with electrons was

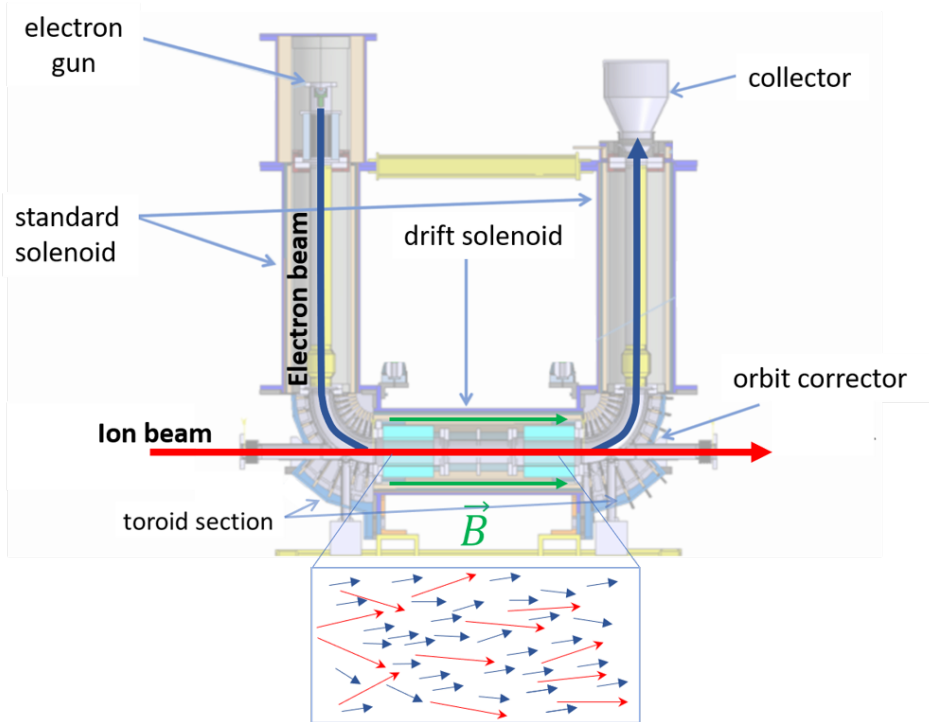


FIGURE 2.6: Schematics of the electron cooler system [83].

invented by G. Budker in 1966 at the Budker Institute of Nuclear Physics (BINP) in Novosibirsk, Russia [84, 85]. It has been used successfully in LEAR [86, 87] and the AD [88] to reduce and maintain the emittance of low energy antiproton beams and so is well understood technology at CERN and the natural choice for ELENA. As the density in the ion beam increases as a result of cooling, the heating due to IBS increases rapidly. The ion plasma will therefore be cooled towards an equilibrium temperature at which

¹To distinguish between electrons and electron cooled particles, the term ion is used for any electron cooled particle, including antiprotons.

the heating counteracts the cooling. The circulating beam is superimposed with a co-moving electron beam in a cooling section of about one to two meters in length. The electron beam is guided through this section by a magnetic field of about $B = 0.02 - 0.2 \text{ T}$ and separated from the ion beam thereafter as shown in Fig. 2.6. A close-up of the overlap region shows the ions traversing, under different angles and velocities, the stream of parallel electrons, all moving with the same velocity. However, if observed from a frame moving with the velocity of the electrons (rest frame), the latter are at rest, whilst the ions pass through the electron gas from any direction and with a variety of velocities, resembling the motion of particles in a hot gas. In the rest frame, one can associate an ion temperature T , which is normally of the order of $1 \times 10^6 \text{ K}$, with the width of the ion velocity distribution. In the rest frame of the beams the cooling process may be regarded as a thermal equilibration between the ion beam and a cold electron plasma, or in a more detailed and microscopic view as the stopping of ions in an electron plasma with a density of about $n_e = 10^6 - 10^7 \text{ cm}^{-3}$. Owing to the Coulomb interaction, their temperatures become equal, i.e., the energy of the thermal motion is transferred from the proton beam to the colder electron beam.

As the proton mass is greater than the electron mass a factor of ≈ 1836 , when their temperature is equal, the velocity of thermal motion of the proton beam and its angular spread are much smaller than those of the electron beam. The cooling rate depends on charge and the mass of the ion, the electron density n_e of the electron beam and the ratio $\eta_e = L/C$ of the length L of the cooling section to the ring circumference C . The cooling rate is particularly sensitive to velocity deviations Δv of the ion from the average electron velocity in all degrees of freedom. In Table 2.1 are listed the nominal parameters of the ELENA electron cooler at intermediate and ejection cooling plateaus.

In a traditional electron cooling system the electrons are emitted from a thermal gun which is immersed in a longitudinal magnetic guiding field, as in the ELENA electron cooler case pictured in Fig 2.7. It was experimentally and theoretically investigated that the magnetic field affects the cooling power and increases the cooling force experienced by ions [89]. Although electron cooling is routinely used at many facilities, the peculiarity of the interaction between the heavy particles (ions or antiprotons) and the electron beam makes the modelling of the cooling process particularly difficult. There are two complementary pictures in which the passage of charged particles through a plasma can be treated: the binary collision approximation (BC) and the dielectric theory (DT). In the BC approximation the focus is on the pairwise interaction of the particles. But in the presence of an external magnetic field \vec{B} even the non-relativistic problem of two charged

TABLE 2.1: Nominal electron cooler parameters for ELENA.

	Intermediate plateau	Ejection Plateau
Momentum (MeV/c)	35	13.7
Electron beam energy (eV)	355	55
Electron current (mA)	5	1
Electron beam density (10^{12} m^{-3})	1.38	1.41
B_{gun} (G)	1000	
B_{drift} (G)	100	
Expansion Factor	10	
Cathode radius (mm)	8	
Electron beam radius (mm)	25	
Electron beam temperatures (eV)	$T_{\perp} = 0.01, T_{\parallel} = 0.001$	
Twiss parameters (m)	$\beta_x = 2.103, \beta_y = 2.186, D_x = 1.498$	
Flange-to-flange (mm)	2330	
Drift solenoid length (mm)	1000	
Effective length (mm)	700	

particles cannot be solved in a closed form as the relative motion and the motion of the centre of mass are coupled to each other. The DT, also referred to as Vlasov technique, takes into account the collective interaction of the electrons in the plasma. A charged particle induces a displacement of electrons, whose electromagnetic field acts back on the particle. The connection between the inducing field from the ion and the induced electric field in the plasma is mediated through a dielectric function, which is a property of the plasma only. Unfortunately, there exists no closed solution of this problem that is uniformly valid for any strength of the magnetic field and the Coulomb force between the particles in either of the models [69].

2.4.1 Binary Collision approximation

In the BC, the momentum transfers from individual electrons scattered against one ion are summed. The method does not take into account screening effects of the electric potential induced by the ion. As a result, an upper integration limit for the impact parameters needs to be introduced.

Consider a single electron-ion collision for the un-magnetised cooling case in the electron beam rest frame. The ion moves with a velocity v_i and scatters from the electron at impact parameter b . The momentum transfer is

$$\Delta P = \int_{-\infty}^{+\infty} \phi_c dt = \frac{1}{4\pi\epsilon_0} \int_{-\infty}^{+\infty} \frac{Ze^2}{s^2 + b^2}, \quad (2.22)$$

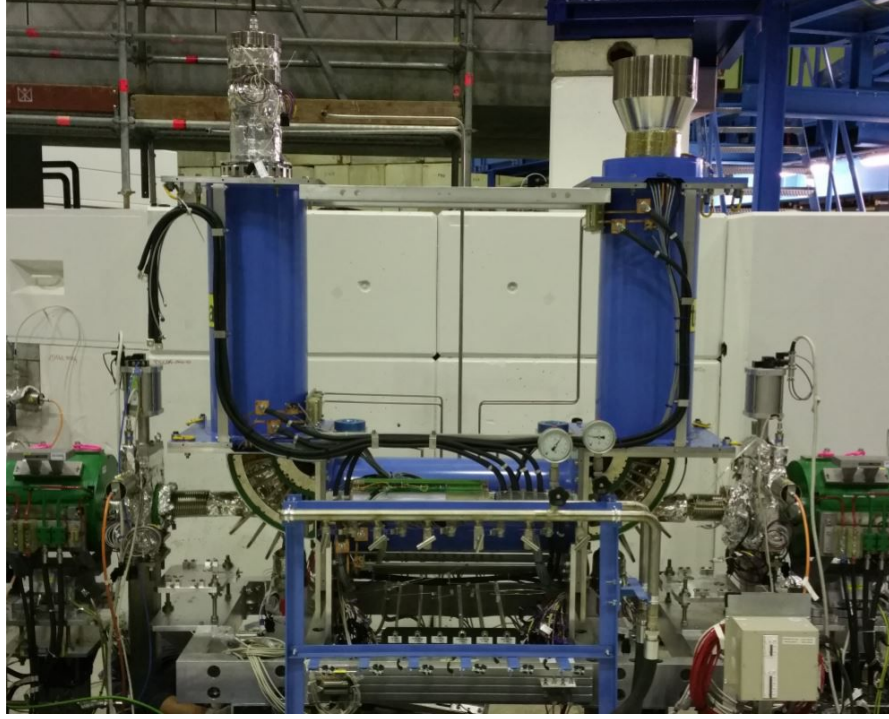


FIGURE 2.7: Picture of the electron cooler during installation in ELENA

ϕ_c being the Coulomb force. As we consider times from negative to positive infinity we can neglect the longitudinal part of the force and we can replace the Coulomb force with the transverse component

$$\phi_{\perp} = \phi_c \frac{b}{\sqrt{s^2 + b^2}}, \quad (2.23)$$

to get

$$\Delta P = \int_{-\infty}^{+\infty} \phi_{\perp} dt = \frac{ze^2}{4\pi\epsilon_0 V_i} \int_{-\infty}^{+\infty} \frac{b ds}{(s^2 + b^2)^{3/2}} = \frac{2Ze^2}{4\pi\epsilon_0 V_i b}. \quad (2.24)$$

The energy transferred from the ion to the electron is then

$$\Delta E(b) = \frac{\Delta P^2}{2m_e} \approx \frac{2Z^2 e^4}{(4\pi\epsilon_0)^2 m_e V_i^2 b^2}, \quad (\text{for } b \gg b_{min}). \quad (2.25)$$

So far we have only considered a single electron-ion collision. When an ion passes through a large number of electrons, we have to integrate over all possible impact parameters to obtain the energy lost as it travels a length ds through an electron cloud of density n_e

$$-\frac{dE}{ds} = 2\pi \int_{b_{min}}^{b_{max}} b n_e \Delta E(b) db = \frac{4\pi z^2 e^4}{(4\pi\epsilon_0)^2 m_e v_i^2} n_e \ln \left(\frac{b_{max}}{b_{min}} \right). \quad (2.26)$$

The logarithmic ratio of maximum to minimum impact parameters $\ln \left(\frac{b_{max}}{b_{min}} \right)$ is called the Coulomb logarithm and its typical value is $L_C \approx 10$. We have considered electrons has being stationary. However, they have a finite temperature T_e and hence a velocity

distribution $f(v_e)$ which can be considered to be Maxwellian characterised by its velocity spread Δ_e . The expression for the unmagnetised cooling force can be then written as

$$\vec{F}(\vec{V}_i) = -\frac{4\pi Z^2 e^4 n_e}{(4\pi\epsilon_0)^2 m_e} \int L_C(\vec{v}_{rel}) f(\vec{v}_e) \frac{\vec{v}_{rel}}{v_{rel}^3} d^3\vec{v}_e. \quad (2.27)$$

Numerical calculations have been performed for BC between magnetized electrons [90, 91] and for collisions between magnetized electrons and ions [92, 93]. A different situation arises for the BC between an electron and uniformly moving heavy ion. As an ion is much heavier than an electron, its uniform motion is only weakly perturbed by collisions with the electrons and the magnetic field. The BC considers the interaction between electrons and heavy ions as a perturbation to the helical motion of the magnetized electrons. We will show in the next chapter the derivation of a cooling force formula in case of a finite magnetic field.

2.4.2 Dielectric Theory

The DT is a continuum theory in which the response of charge and current densities to external perturbations is calculated. While this requires cutoffs at small distances (or large wave numbers in Fourier space) to exclude hard collisions of close particles, the collectivity of the excitation can be taken into account.

For a physically meaningful comparison between DT and BC we adhere to the following terminology: the basic, but generally unobserved quantity in BC is the energy or velocity transfer ΔE_i or Δv_i , respectively, to the test particle in a collision with specific initial data. Averaging with respect to quantities like the phase angle φ of the cyclotron motion and integration with respect to the impact parameter b yields the energy loss dE_i/ds of the test particle with monochromatic electrons. Here $d\vec{s} = \vec{v}_i dt$ is the path element of the test particle moving with velocity \vec{v}_i in a time interval dt . Then averaging with respect to the electron velocity distribution $f(\vec{v}_e)$ yields the stopping power S and the stopping force or cooling force \mathcal{F}

$$S = -\mathcal{F} \cdot \hat{\mathbf{V}}_i - \frac{d\mathcal{E}_i}{dl} = -\left\langle \frac{dE_i}{dl} \right\rangle. \quad (2.28)$$

2.5 Beam Diagnostics

Beam diagnostics are all the instrumentation used for the observation of particle beams with the precision required to tune, operate, and improve the accelerators and their associated transfer lines. Beam diagnostics are an essential constituent of any accelerator.

These systems are like organs of sense that allow measurement of the properties of the beam and to be observed inside the accelerator. There exists today a vast choice of different types of diagnostic devices, each usually in many variants. To ensure that the low emittance required by the antimatter experiments is reached in ELENA, different diagnostics systems were implemented in the ring:

- Eight combined beam position monitors (BPMs) for reliable orbit measurements
- Longitudinal Schottky pick-ups for intensity measurement and cooling control
- Ionisation profile monitor (IPM);
- Beam Scraper for beam profile and emittance measurements

2.5.1 Beam Position Monitors

BPMs are the non-destructive diagnostics used most frequently at nearly all linacs, cyclotrons, and synchrotrons. BPMs deliver the centre of mass of the beam and act as a monitor for the longitudinal bunch shape. The signal generation by the beams electromagnetic field is described using the transfer impedance concept [94]. In the early days a BPM monitoring system simply consisted of an oscilloscope linked directly to the pick-up signals. Since then, enormous advances in the acquisition and processing electronics have been made, turning beam position monitors into very complex systems. The measurement of beam position relies on processing the information from pick-up electrodes located in the beam pipe [95]. A great variety of devices can be used:

- Optical techniques:
 - scintillating screens (all beams)
 - synchrotron light monitors (for e^-)
 - optical transition radiation (e^-)
 - residual gas fluorescence monitors (for protons)
 - residual gas monitors (protons).
- Electronics techniques:
 - secondary electron emission grids
 - wire scanners (all beams)
 - grids with gas amplification (protons).

As the beam passes through the accelerator vacuum tube, it produces electromagnetic fields that depend on the beam position and geometry. The beam locations are detected by a number of electrodes around the beam pipe composing the BPM device. The beam should be ideally located at the pipe centre. To assure proper positioning of the beam, the beam position should be monitored continuously in real time. A BPM normally provides information about the beam phase and beam transverse position by using position sensitive detectors (PSDs). In most accelerators, each BPM setup consists of four PSDs symmetrically placed 90 degrees apart, followed by an electronic system for signal processing in order to determine the beam transverse position. The beam position is achieved by comparing the picked up voltages of either horizontal or vertical directions.

2.5.2 Ionisation Profile Monitor

IPMs are non-destructive devices used in proton synchrotrons: the circulating particles interact with the residual gas of the machine creating pairs of ions and electrons. The idea is to collect one of these two species or even both to measure the beam profile [96]. In a simple detector the ions are preferably used, as their transverse speed is smaller. The ultrahigh vacuum (less than 10×10^{-11} mbar) needed in the low-energy machines limits the ionisation rate to some $10 \times 10^4 \text{ s}^{-1}$ in a monitor of 50 mm length. One way to amplify the signal consists of accelerating the ions to a Micro Channel Plate systems (MCP) where electrons are created, their number amplified and then collected on the detector.

2.5.3 Schottky monitor

Diagnostics performed with the use of Schottky pick-ups have the advantage of being non-perturbative, i.e. there is no change in the beam parameters. The method is based on statistical information extracted from RMS noise. In ELENA the Schottky monitors are used to measure the longitudinal momentum spread, used also to calculate the emittance [97]. The signals detected for a coasting beam may be summed around the ring, making corrections for time of flight between pick-ups and allowing for the data to be analysed as a single Schottky pickup measurement. The signal may then undergo a fast Fourier transform (FFT) resulting in a spectral density distribution, with Schottky peaks at harmonic frequencies. Averaging to account for the 20 BPMs, an estimate for the longitudinal momentum spread may be made by measuring the RMS of a frequency

peak in the data, Δf_h , of known harmonic number, h

$$\sigma_\delta = \frac{1}{\eta} \frac{\Delta f_h}{f_h} \quad (2.29)$$

where η is the frequency dispersion or phase slip factor and f_h is the centre frequency of the peak [98]. In ELENA the system is able to measure up to $h = 111$, and where possible a higher harmonic will be selected to allow for more frequent measurements, since the required acquisition time is inversely proportional to h .

2.5.4 Scraper system

Beam scraping allows the transverse phase space of the beam to be probed by either moving a scraper blade transversely into the path of the beam, or creating a local orbit bump using steering magnets to progressively shift the beam into a fixed position blade as in the BEAMSCOPE of the PSB [99]. For the scraper in ELENA, the moving mechanism had been chosen [100, 101]. The movement of the scraper blades is slow in comparison to the beams revolution frequency to ensure all particles with a maximum amplitude equal to, or greater than, the scrapers position are eliminated. As the beam is intercepted, the intensity of the subsequently generated secondary particle shower is measured as a function of the position of the scraper blade. By taking the intensity of this particle shower as an indicator for the intensity of the beam along the corresponding scraper position, the transverse phase space density for the direction of the scrapers movement can be obtained. The emittance and other useful information may then be inferred through analysis, for example by estimating the 95% beam width as in the AD system, or by making a fit to the data assuming a specific beam profile. Although scraping destroys the beam being measured, it has the advantages of being simple to use and is suitable for low energy and low intensity machines. The main hardware comprising the scraping system in ELENA consists of two scraper blade windows at right angles to each other, each attached to a motorised arm, four MCPs, two scintillator detectors, a stainless steel vacuum tank, and the associated support structures.

In the next chapter it will be illustrated how these effects can be accurately modelled in order to be able to perform predictive simulations for beams in low energy storage ring.

Chapter 3

The Model

The previous chapter introduced electron cooling and the cooling force (also called friction force or drag force) exerted on the circulating ions. This chapter presents how the electron cooling process is treated in different theoretical frameworks. The models used to describe the beam geometry and machine imperfections are also introduced together with collective effects impacting the beam.

3.1 Cooling Force

It has been already shown how the theories used to describe the cooling process cannot provide closed form solutions to express the force in case of a finite magnetic field inside the cooler (see section 2.4). In this section the models and approximations used to provide accurate predictions for electron coolers are discussed.

The change in the ion energy is calculated under the assumption of a constant ion velocity. Alternatively this energy transfer can be expressed by the velocity transferred to the electrons during the collision.

We will approximate the distribution of electrons assuming an axial symmetry. The electron distribution function can then be written in the following form

$$f(v_e) = \left(\frac{1}{2\pi}\right)^{3/2} \frac{1}{\Delta_{\perp}^2 \Delta_{\parallel}} \exp\left(-\frac{v_{\perp}^2}{2\Delta_{\perp}^2} - \frac{v_{\parallel}^2}{2\Delta_{\parallel}^2}\right), \quad (3.1)$$

where Δ_{\perp} and Δ_{\parallel} are the electron rms velocity spreads in the transverse and longitudinal direction, respectively.

In the case of an ultracold electron plasma, i.e. in a plasma where the rms electron velocity is negligible compared to the ion velocity, both BC and DT give the same

expression for unmagnetized cooling [102]

$$\vec{F}(\vec{V}_i) = \frac{Z^2 e^2 \omega_p^2}{4\pi\epsilon_0} L(V_i) \frac{\vec{V}_i}{v^3}, \quad (3.2)$$

except for the Coulomb logarithm which is model dependent:

$$L(V_i) = \begin{cases} \ln \left(\sqrt{1 + \left(\frac{V_i^2 b_{max}}{Z r_e c^2} \right)^2} \right), & \text{BC} \\ \ln \left(\frac{V_i k_{max}}{\omega_p} \right), & \text{DT} \end{cases} \quad (3.3)$$

where $r_e = 2.82 \times 10^{-15}$ m is the classical electron radius, Z is the charge number of the ion, V_i its velocity and $\omega_p = \sqrt{\frac{4\pi n_e e^2}{m_e}}$ is the plasma frequency. The cut-off parameters b_{max} and $k_{max} = 1/b_{min}$ are given by

$$\begin{aligned} b_{min} &= \frac{Z r_e c^2}{V_i^2}, \\ b_{max} &= \frac{V_i}{\omega_p}. \end{aligned} \quad (3.4)$$

In the regime of electron cooling the logarithm is large leading to agreement as shown in Fig. 3.1. The two formulations differ when $V_i \ll 1$. The upper integration limit b_{max} is given by the Debye screening length while the lower limit b_{min} can be identified as the closest distance in an electron collision for $Z < 0$. For positively charged ions the corresponding cut in wave number k can be understood as a threshold for an electron to become captured by the Coulomb potential. Until now, the acceleration and the solenoid field, which prevents the electron beam from diverging, have not been taken into account.

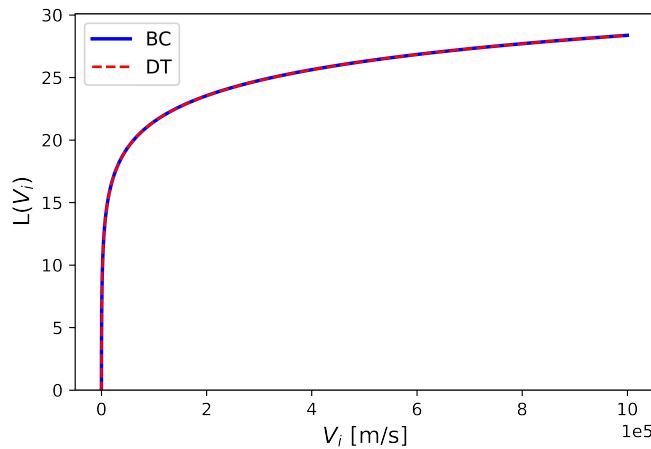


FIGURE 3.1: Plot of the two expression for the Coulomb logarithm. In blue is the result from the BC and in red from the DT.

The velocity spread in the longitudinal direction decreases by several orders of magnitude when the electrons are accelerated. The resulting anisotropic velocity distribution does not equalize in all directions due to the magnetic field. Since the mobility of the electrons in the transverse directions is suppressed by the magnetic field, the effective velocity spread is small compared to the initial velocity spread given by the cathode temperature. As a consequence, the cooling force is enhanced and reaches its maximum at the velocity determined by the rms angle of solenoid field imperfections. The effect of the solenoid field and the anisotropic electron velocity distribution was implemented into the theory of electron cooling by Derbenev and Skrinsky in 1978 [89, 103]. The presence of a strong external magnetic fields constitutes a theoretical challenge [89], as its influence on the cooling which the magnetized electrons exert on the ions is not so obvious as earlier models might suggest [104]. In the DT the drag on the ion is due to the polarization it creates in its wake. This can be either calculated in linear response (LR) [105, 106] or numerically by a particle-in-cell (PIC) [107, 108] simulation of the underlying nonlinear Vlasov-Poisson equation [109]. While the LR requires cutoffs to exclude hard collisions of close particles the collectivity of the excitation can be taken into account in both approaches. In the complementary BC approximation the drag force is accumulated from the velocity transfers in individual collisions. This has been calculated by scattering statistical ensembles of magnetized electrons from the ions in the classical trajectory Monte Carlo method (CTMC) [93], and by treating the Coulomb interaction as a perturbation to the helical motion of the electrons [69, 110, 111]. The observed cooling force \vec{F} on an individual ion is obtained by integrating with respect to the impact parameter and the electrons velocity distribution. The ion velocity \vec{V}_i is measured with respect to the centre of that distribution. As in an electron cooler the electrons are accelerated from the cathode, their velocity distribution is flattened longitudinally, but the spread does not vanish.

3.1.1 Parkhomchuk Formula

Due to the limitations of the Coulomb logarithm approximation, the general practice is to use the empirical formula by Parkhomchuk [112, 113]

$$\vec{F}(\vec{V}_i) = -\frac{Z^2 e^2 \omega_p^2}{4\epsilon_0} \ln \left(1 + \frac{b_{max}}{b_{min}} \right) \frac{\vec{V}_i}{(V_i^2 + \Delta_{eff}^2)^{3/2}} \quad (3.5)$$

which has become the standard for analysis of electron cooling data. It was derived from parameter fitting of measured data and includes magnetic field imperfections.

The Coulomb logarithm, with impact parameters given by

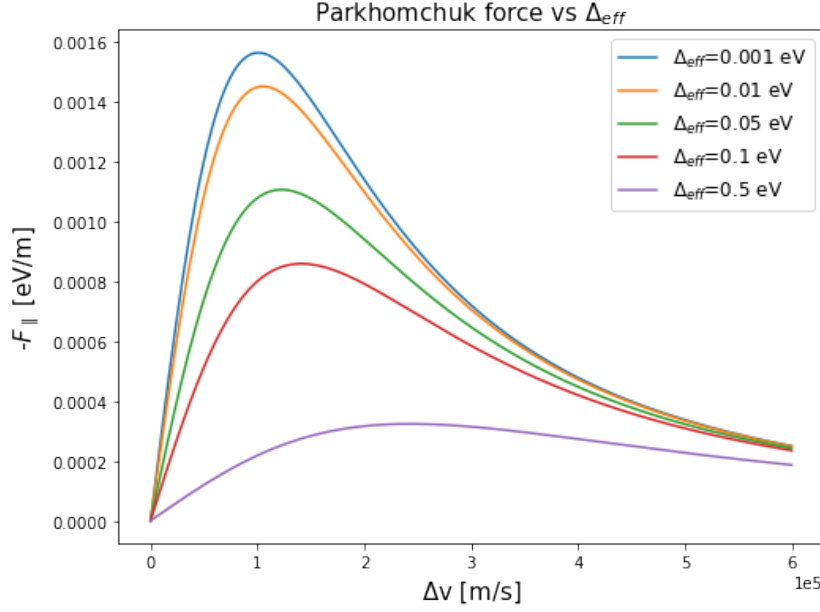


FIGURE 3.2: Representation of the impact of the Parkhomchuk's fitting parameter Δ_{eff} on the cooling force trend.

$$\begin{aligned} b_{\max} &= \frac{V_i}{\omega_p + 1/\tau}, \\ b_{\min} &= \frac{Z^2 r_e c^2}{V_i^2} + \frac{\Delta_{\perp}}{\omega_c}, \end{aligned} \quad (3.6)$$

is written such that it will always be positive and is applicable for small ratios of maximum to minimum impact parameters. Here $\tau = \frac{l_{\text{cool}}}{\beta_{\text{rel}} \gamma_{\text{rel}} c}$ is the ion time of flight inside the cooling section in the particle rest frame, $\omega_c = \frac{eB}{2m_e}$ is the cyclotron (or Larmor) electron frequency and Δ_{eff} is the effective velocity spread of the electron Larmor circles and can be expressed as

$$\Delta_{\text{eff}} = \sqrt{\Delta_{\parallel}^2 + \Delta_{\perp}^2}. \quad (3.7)$$

The effective velocity spread takes into account the magnetic field imperfections and the longitudinal velocity spread of the electrons. In general, Δ_{eff} is difficult to evaluate a priori and is used for parametrisation of measured data but as seen in Fig. 3.2 it has a huge impact on the resulting force.

3.1.2 Erlangen Formula

The treatment of the electron-ion interaction in the presence of a magnetic fields requires several considerations. In a strong magnetic field the electrons' transverse motion is

quenched and they are constrained to move along the field lines. Thus for reliable results on the influence of the magnetic field on the energy loss the scattering must be studied on a deeper level, as in the approach chosen by the Erlangen University group [69, 92].

Consider collisions of electrons with an ion moving along the field lines ($v_{i\perp} = 0$). The process is completely symmetric, the energy gained in approaching the ion is again lost on the way out. Therefore in this situation the magnetic field suppresses the energy loss completely [89]. It is important to note that this argument is only valid for the attractive interaction of electrons with positively charged ions. For the repulsive case, e.g. electrons and antiprotons, there will be reflections for small impact parameters. Such violent changes in the trajectories cannot be treated as perturbations of the helical motion of the electrons. The modification introduced to treat this case are presented in the next section.

It is useful to distinguish three regimes of trajectories depending on the relative size of the distance of closest approach, the cyclotron radius and the pitch of the helix as shown in Fig. 3.3.

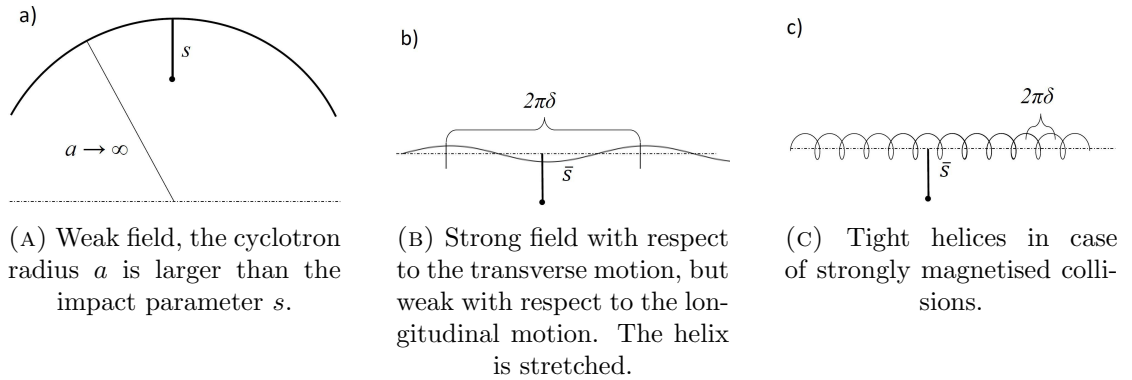


FIGURE 3.3: Schematic trajectories of relative motion of electrons and ions for different intensity ranges of the magnetic field.

The unperturbed motion of electron is a helix with the Larmor radius

$$\bar{s} = \frac{cmv_{\perp}}{eB} \quad (3.8)$$

and whose pitch is determined by the longitudinal velocity. The small v represents the electron velocity and its components. The three regimes for electron collisions are: weak field, stretched helices and tight helices.

If the cyclotron radius is much larger than the distance of closest approach (as in Fig. 3.3a) the influence of the magnetic field is weak and the energy loss in this Coulomb regime is the same as the unmagnetized case. This can also be seen at high ion velocities

($V/\omega_c \gg 2e^2/mV^2$). In this case the components of the cooling force (in cylindrical coordinates) can be written as [4]:

$$F_{\perp} = -\sqrt{\frac{2}{\pi}} \frac{Z^2 e^4 n_e}{m \Delta_{\perp}^2 \Delta_{\parallel}} \iiint \ln \left(\frac{\rho_{max}}{\rho_{min}} \right) \frac{(V_{\perp} - v_{\perp} \cos \varphi) \exp \left(-\frac{v_{\perp}^2}{2\Delta_{\perp}^2} - \frac{v_{\parallel}^2}{2\Delta_{\parallel}^2} \right)}{((V_{\parallel} - v_{\parallel})^2 + (V_{\perp} - v_{\perp} \cos \varphi)^2 + v_{\perp}^2 \sin^2 \varphi)^{3/2}} v_{\perp} d\varphi dv_{\parallel} dv_{\perp}, \quad (3.9)$$

$$F_{\parallel} = -\sqrt{\frac{2}{\pi}} \frac{Z^2 e^4 n_e}{m \Delta_{\perp}^2 \Delta_{\parallel}} \iiint \ln \left(\frac{\rho_{max}}{\rho_{min}} \right) \frac{(V_{\parallel} - v_{\parallel}) \exp \left(-\frac{v_{\perp}^2}{2\Delta_{\perp}^2} - \frac{v_{\parallel}^2}{2\Delta_{\parallel}^2} \right)}{((V_{\parallel} - v_{\parallel})^2 + (V_{\perp} - v_{\perp} \cos \varphi)^2 + v_{\perp}^2 \sin^2 \varphi)^{3/2}} v_{\parallel} d\varphi dv_{\parallel} dv_{\perp}. \quad (3.10)$$

Here both impact parameters — minimum and maximum — are functions of the electron velocity

$$\begin{aligned} \rho_{min} &= \frac{|Z|e^2}{m_e} \frac{1}{(V_{\parallel} - v_{\parallel})^2 + (V_{\perp} - v_{\perp} \cos \varphi)^2 + v_{\perp}^2 \sin^2 \varphi}, \\ \rho_{max} &= \bar{s} = \frac{cmv_{\perp}}{eB}. \end{aligned} \quad (3.11)$$

If the magnetic field is strong enough that the motion of the electrons is observed as helical also from an ion based reference system it is possible to define two limiting cases

$$\begin{cases} \delta = \frac{cm\sqrt{V_{\perp}^2 + (V_{\parallel} - v_{\parallel})^2}}{eB} \gg \bar{s} \\ \delta \ll \bar{s} \end{cases} \quad (3.12)$$

where δ is the pitch of the helix as seen from the ion.

- If the helices are stretched so that their pitch is larger than the impact parameter $\delta \gg \bar{s}$ (see Fig. 3.3b) the trajectories are quite similar to those of the Coulomb regime in the vicinity of the scattering centre. When the ion velocity $V_i \gg \Delta_{\parallel}$, the electron distribution can be approximated by the delta-function $f(v_{\parallel}) = \delta(v_{\parallel})$. The formulae for collisions with stretched helices can be then written in the form

$$F_{\parallel} \approx -V_{\parallel} \frac{4\pi Z^2 e^4 n_e}{m} \frac{1}{(V_i^2 + \Delta_{\parallel}^2)^{3/2}} \left[\ln \left(\frac{\rho_{max}}{\langle \bar{s} \rangle} \right) + \ln \left(\frac{\omega_p}{\omega_B} \right) \right], \quad (3.13)$$

$$F_{\perp} \approx -V_{\perp} \frac{4\pi Z^2 e^4 n_e}{m} \frac{1}{(V_i^2 + \Delta_{\parallel}^2)^{3/2}} \left[\ln \left(\frac{\rho_{max}}{\langle \bar{s} \rangle} \right) + \ln \left(\frac{\omega_p}{\omega_B} \right) \right] \quad (3.14)$$

where ω_p is the plasma frequency and $\omega_B = \frac{eB}{m}$ is the cyclotron frequency. This formula is valid for $\frac{V_i}{\Delta_{\perp}} \gg 1$ and its structure is similar to semi-empirical formula by Parkhomchuk Eq. 3.5.

- More interesting is the case of tight helices, where $\delta \ll \bar{s}$ (as represented in Fig. 3.3c). The force on the ion must be modified as the electrons are only allowed to move in the direction of the magnetic field. The resulting cooling force components can be expressed in the following form

$$F_{\parallel} = -V_{\parallel} \frac{4\pi Z^2 e^4 n_e}{m V_i^3} \frac{V_{\perp}^2}{V_i^2} L_M, \quad (3.15)$$

$$F_{\perp} = -V_{\perp} \frac{4\pi Z^2 e^4 n_e}{m V_i^3} \frac{V_{\perp}^2 - V_{\parallel}^2}{V_i^2} L_M. \quad (3.16)$$

Here the Coulomb logarithm is evaluated as

$$L_M = \frac{1}{\Delta_{\perp}^2} \int_0^{\infty} \ln \left(\frac{\rho_{\max}}{\max(\bar{s}, \delta)} \right) \exp \left(-\frac{v_{\perp}^2}{2\Delta_{\perp}^2} \right) v_{\perp} dv_{\perp} \approx \ln \left(\frac{\rho_{\max}}{\langle \bar{s} \rangle} \right). \quad (3.17)$$

3.1.2.1 Modified formula for antiprotons

It is immediately expected for there to be a significant difference between the attractive and repulsive interactions in a binary collisions picture just by simple symmetry arguments. In fact in the presence of a strong magnetic field, the electrons move parallel to the magnetic field. For reasons of symmetry, no velocity can be transferred to positively charged ions which also move parallel to the field, with $v_{e\perp} = 0$. The energy transfer and hence the stopping power within BC treatment must therefore vanish.

In the case of a weak field the process can be approximated as a fast collision and the treatment for attractive or repulsive interaction is the same and the force components can be written as in Eq. 3.9 and Eq. 3.10.

But if the magnetic field is stronger, the relative velocity v_r between ions and electrons decreases, the minimum impact parameter $\rho_{\min} = \frac{|Z|e^2}{m_e v_r^2}$ grows and the unmagnetized approximation does not apply any more. The Coulomb logarithm used in the fast collision approximation goes to zero $L_C \rightarrow 0$ at $v_r = v_{\perp} \left(\frac{2e^2 \omega_c}{m_e} \right)^{1/3}$. With further reductions of the velocity the Coulomb logarithm for the magnetized collisions decreases and vanishes at $v_r \approx v_2 = \left(\frac{2e^2 \omega_p}{m_e} \right)^{1/3}$.

In this region the kinetic energy of the relative motion is comparable to the potential interaction energy

$$v_2 = \left(\frac{2e^2 \omega_p}{m_e} \right)^{1/3} \propto \left(\frac{2e^2 n_e^{1/3}}{m_e} \right)^{1/2}. \quad (3.18)$$

For large magnetic fields the electrons tend to move like beads on a wire along the magnetic field lines, as depicted in Fig. 3.4.

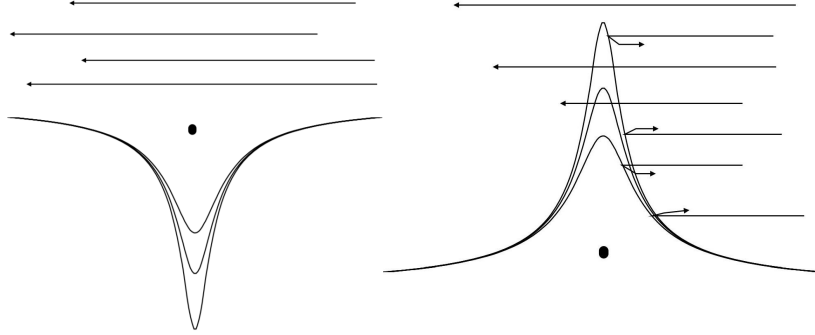


FIGURE 3.4: In a strong magnetic field electrons are constrained to move along the field lines. For an attractive potential there is no scattering (left), for a repulsive potential (as the one due to the negative charge of the antiprotons) low energy electrons are back-scattered (right).

For attractive interactions and for ions also moving along the magnetic field lines the acceleration of the electron when entering the potential is fully cancelled by the subsequent deceleration when leaving it. In this case the velocity and energy transfer between ion and electron vanishes. For a repulsive interaction, however, large velocity transfers occur when the particles are reflected from each other which results in a non-zero velocity and energy transfer between ion and electrons. For negatively charged ions, the electron can either pass over the potential well, which gives again no energy transfer, or it is reflected with a momentum transfer of two times its initial momentum. This effect leads to the appearance of an additional contribution to the cooling force for the negatively charged particles

$$\Delta F_{\parallel} = -\pi \rho_{min}^2 Z^2 n_e v_r (2m_e v_r) = -\frac{8\pi n_e e^4}{m v_r^2}. \quad (3.19)$$

This happens when the Larmor radius of the helical motion of the electrons \bar{s} is smaller than the minimum impact parameter $\rho_{min} = \frac{|Z|e^2}{m v_{r\parallel}}$, where $v_{r\parallel}$ is the initial relative velocity between the electron and the ion. Under these circumstances the electron is reflected by the potential well with a momentum transfer of two times its initial momentum, resulting in a backscattering event. The additional contribution (Eq. 4.21) gives rise to a significant increase of the cooling force as shown in Fig. 3.5.

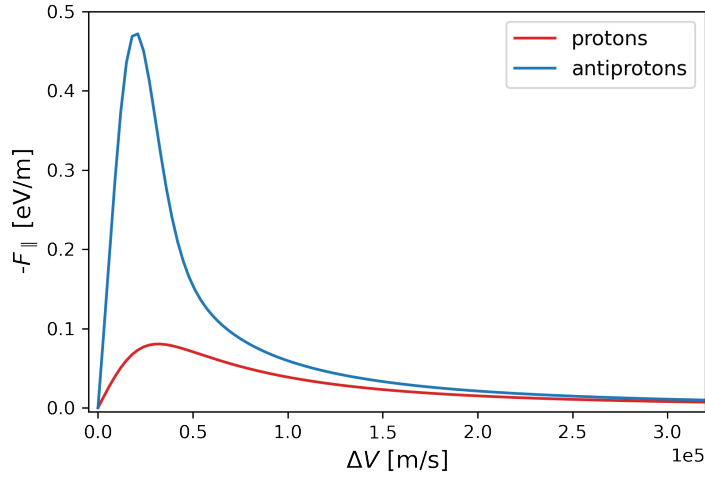


FIGURE 3.5: Comparison of the Erlangen cooling force model for protons and antiprotons with ELENA electron cooler parameters.

3.2 Performance limiting factors

3.2.1 IBS

During machine operation the beam will undergo IBS. Since the growth rates introduced by IBS are inversely proportional to the fourth power of the Lorentz factor, γ_{rel}^4 , they are much more significant for lower energy machines such as the AD or ELENA. IBS is expected to be a limiting factor in the final emittance when it is in equilibrium with the electron cooling force.

Bjorken and Mtingwa developed an approach to IBS using the scattering matrix formalism from quantum electrodynamics (B-M model) [77]. Both B-M and Martini's models are in good agreement with one another. One important question is “in what way is IBS in particle beams different from similar scattering of gas molecules?” The difference lays in the fact that in circular accelerators, the curvature of the orbit produces a dispersion. Because of this dispersion, a change of energy leads to change in the betatron amplitude. In other words, the longitudinal and transverse motion are coupled. For the analysis presented in this thesis the Martini model was applied to simulate this effect. This model extends the Piwinski model, taking into account derivatives of the lattice functions. The rms emittance growth is calculated assuming Gaussian beams and considering only the BC, so that multi-particle interactions are ignored. A detailed treatment of the Martini model is beyond the scope of this thesis and can be found in [4, 76].

3.2.2 Space Charge in an Electron Beam

The overall electron cooling system is embedded in a longitudinal magnetic field aimed to counteract the electron beam space charge forces and to magnetize the electrons.

Space charge effects are a specific case of Coulomb interaction in a multiparticle system. The net effect of the Coulomb interaction in a multiparticle system can be classified into two regimes [114]:

- (i) the *collisional regime*, dominated by binary collisions caused by close particle encounters, i.e. single-particle scattering,
- (ii) the *collective regime* or space charge regime, dominated by the self-field produced by the particle distribution, which varies appreciably only over large distances compared to the average separation of the particles.

The collisional part of the total interaction force arises when a particle is scattered by its immediate neighbours. This force will cause small random displacements of the particles trajectory and statistical fluctuations in the particle distribution as a whole, leading for example to IBS effects in high-energy storage rings [70]. On the other hand, space charge forces lead to collective behaviour of the beam, driving for example envelope oscillations and emittance [115]. The cooling efficiency depends drastically on the fluctuation intensity in the electron beam caused by the space charge effect. The fluctuations present in the cooling region cause the stochastic heating of the ions, which adversely affects the cooling efficiency and may even annihilate the ion beam.

The space charge effects lead to dependence of the mean electron velocity and electron velocity spread on co-ordinates inside the electron beam. There are two general effects related to the space charge of electron beam:

1. Electron longitudinal momentum shift due to potential distribution inside the beam.
2. Drift motion of the electrons in the crossed guiding longitudinal magnetic field of the cooler solenoid and radial electric field of the electron beam.

The electron drift motion leads to two effects: electron beam rotation with the drift velocity around its axis and increase of the transverse velocity spread by the value depending on conditions of the electron beam injection into the magnetic field. In the worst case additional transverse velocity spread is equal to the drift velocity value. The space charge effects can be calculated accurately for electron beam of uniform density

distribution. In this case the relative longitudinal momentum shift of the electrons at the point (x^*, z^*) is calculated in accordance with

$$\delta\theta_s = (1 - \eta_n(r^*)) \frac{eI}{\beta^3 \gamma m_e c^3} \left(\frac{r^*}{a} \right)^2 \quad (3.20)$$

where

$$r^* = \sqrt{(x^*)^2 + (z^*)^2} \quad (3.21)$$

I and a are the electron beam current and radius correspondingly, η_n is a factor indicating the electron beam space charge neutralisation by ions of residual gas. The relative coherent drift velocity is calculated as

$$\theta_d = (1 - \eta_n(r^*)) \frac{2I}{cB\beta\gamma^2} \frac{r^*}{a^2} \quad (3.22)$$

where B is the magnetic field value. Both quantities $\delta\theta_s$ and θ_d do not depend on the longitudinal coordinates.

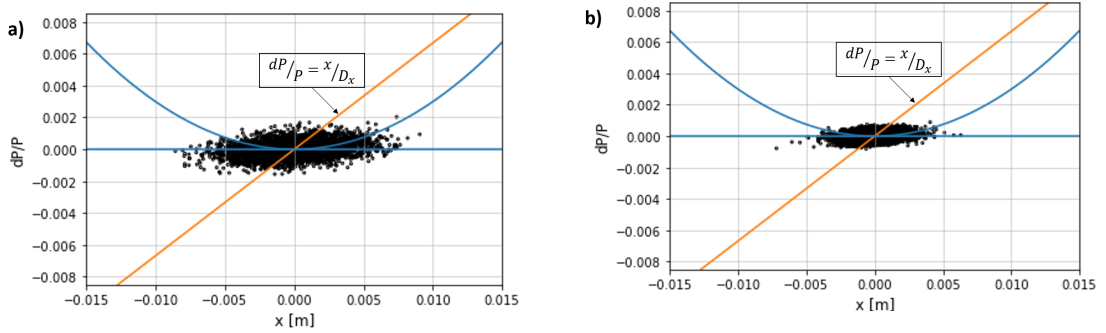


FIGURE 3.6: Distribution of an ensemble of 1000 modelled antiprotons in the cooler at $t=0$ s a) and at $t=4$ s b) for the second cooling plateau. The parabola represents the momentum spread of the electrons due to space charge. The straight orange line represents the dispersion line $\Delta p/p = x/D_x$ for the antiproton beam, where D_x is the first order optical dispersion at the electron cooler position.

Figure 3.6 shows the distribution of modelled antiprotons in the space $x - \Delta p/p$ at the beginning ($t=0$ s) and at the end ($t=4$ s) of the second cooling plateau. The parabolic momentum spread of the electrons due to space charge is also represented in Fig. 3.6. Antiprotons in the centre of the beam distribution cool faster than those in the tails, which is due to the strength of the electron-antiproton interaction as a function of the relative velocity. In other words, because of the space charge parabolic velocity distribution of the electrons, beam particles at large amplitudes experience a weaker cooling force than in the core.

3.2.3 Electron Beam Shape

Typical numerical approximations of electron cooling processes assume that the density distribution of electrons in analytical form and the velocity distribution space to be Maxwellian (Eq. 3.1). But since the cooling force and the process of ion cooling depends critically on the details of the electron velocity distribution, a treatment employing a more realistic distribution is desirable.

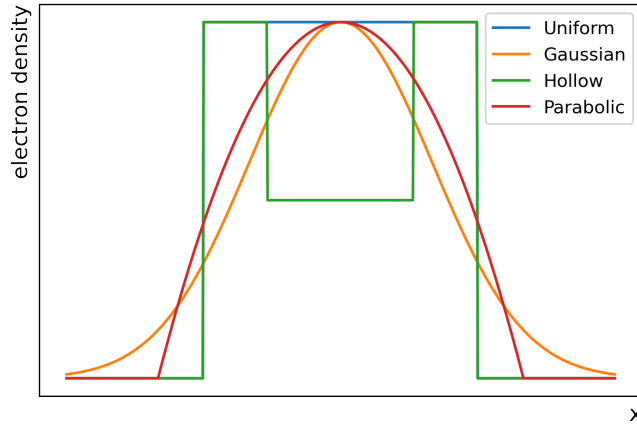


FIGURE 3.7: Schematic representation of electron beam distribution models used for the simulations.

It is not possible to perform direct measurements of the electron beam profile inside of the electron cooler. However, it is possible to see a clear dependence of the emittance evolution on the electron beam distribution, an understanding of the true shape of the distribution is therefore needed. Several analytical models of the electron beam profile can be considered and are shown in Fig. 3.7. The models of electron beam need to be accounted for in the simulations, which calculate the list of parameters required for cooling force evaluation. The local electron beam density is determined by the geometry of the electron beam. The local velocity spread is a function of co-ordinates inside the electron beam and space charge effects are also taken into account. The space charge effects can also lead to a shift of the electron mean velocity. This does not change the beam velocity spread and it is used to correct the longitudinal component of the ion velocity. For the studies presented in this thesis four distribution models are considered:

- **Uniform beam**, where the electron beam density is assumed to be independent of the ion co-ordinates inside the electron beam. The local electron beam density in the lab reference frame is constant and determined by the expression

$$n_e = \frac{I_e}{e\pi a^2 \beta_{rel} c}, \quad (3.23)$$

where I_e is the electron current and a is the electron beam radius.

- **Gaussian beam**, which is a more realistic model to represent the case of electron cooling with magnetized circulating electron beam. The local electron beam density in a position (x, y) is calculated in accordance with

$$n_e = \frac{\lambda_e}{2\sigma_x\sigma_z\gamma_{rel}} \exp\left(-\frac{x^2}{2\sigma_x^2} - \frac{y^2}{2\sigma_y^2}\right), \quad (3.24)$$

where λ_e is the number of electrons per unit of length, related to the electron current by $I_e = e\lambda_e\beta_{rel}c$ and σ_x, σ_y are the rms dimensions of the cylinder cross section.

- **“Hollow” beam**, which represents the electron distribution as an infinite cylinder which has non-uniform radial density distribution. It can be described as two cylinders inside one another, each having a different uniform electron density. The electron current is given by

$$I_{beam} = I_{ring} + I_{hole}, \quad (3.25)$$

where $I_{ring} = en_{ring}\pi(a - r_{hole})^2\beta_{rel}c$ and $I_{hole} = en_{hole}\pi r_{hole}^2\beta_{rel}c$.

- **Parabolic distribution**, that considers the density in the centre of the electron beam as

$$n_0 = 2 \frac{I_e}{\pi a^2 e \beta_{rel} c}, \quad (3.26)$$

and the dependence of the electron density on the beam radius is defined as

$$n_e(r) = n_0 \left(1 - \frac{r^2}{a^2}\right), \quad (3.27)$$

where r is the radial distance of the ion from the centre of the electron beam.

3.2.4 Misalignments

When modelling the performance of a machine like ELENA it is very important to simulate realistic scenarios, since at such low energies even small imperfections can lead to a significant changes in the orbit and evolution of the antiproton beam profile. One of the more common causes of a limitation in the cooling performance is the presence of misalignments between the ion and electron beam. There are two main sources of misalignment in the cooling section: one is the displacement of the electron and ion trajectories due for example to imperfections in the electron cooler assembly the other

is the presence of a shift and angle in the solenoid magnetic centre in respect of the ideal electron beam trajectory.

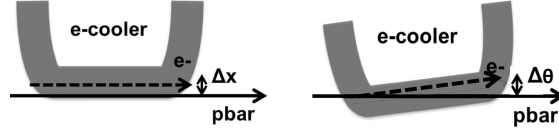


FIGURE 3.8: Schematic representation of misalignments between the ion and the electron beam trajectories. On the left is represented an offset Δx , on the right an angular displacement.

The displacement of the particles' trajectories can result in an angle or an offset between the ion and electron beam (schematically represented in Fig. 3.8) or both. An offset between ions and electrons will give rise to the probing of a smaller fraction of the electrons. If the ion beam is much smaller than the electron beam, this will only lead to small changes in the cooling time, which is caused by the increased initial velocity difference between the circulating beam and the electron beam. With an angular misalignment between the two beams the circulating beam experiences a higher effective electron temperature because part of the longitudinal velocity is now experienced as transverse velocity spread. The physical overlap as well may be altered, and the cooling time therefore increased. This effect will be further enhanced if there is dispersion in the ion beam, as parts of the electron beam may be offset. Finally, the longitudinal and transverse degrees of freedom of the electron beam are mixed, and as the longitudinal temperature is much smaller than the transverse this may lead to less efficient cooling.

3.2.5 Magnetic field imperfections

Another source of misalignment may be the presence of an imperfection in the electron cooler solenoid magnetic fields. The solenoids are used to minimize divergence of electron beam due to the transverse space charge force of the electron beam itself, stability and guidance of the electron beam, and also to decrease the electron transverse temperature via adiabatic expansion. In the presence of transverse components of the guiding magnetic field at the axis of the cooler solenoid, the electron beam is characterized by co-ordinates of its centre position and an angle between electron beam axis and ion equilibrium orbit. In this case the ion transverse angles in the frame referenced to the electron beam orbit have to be corrected by the values of the angular misalignment $\delta\theta$

between electron and ion beams

$$\theta_{\alpha}^* = \theta_{\alpha} - \delta\theta_{\alpha}(s), \quad \text{with } \alpha = x, z \quad (3.28)$$

where θ^* is the ion angle in the electron beam reference frame. In chapter 4 the impact of these imperfections on the calculations of emittance evolution will be shown.

Chapter 4

Simulation Methods for Low Energy Synchrotrons

To obtain reliable results and fully understand the impact of the effects acting on the ELENA antiproton beam during cooling, the model presented in the last chapter needs to be implemented into simulation tools. The following sections illustrate the programs used for the calculation of cooling force and emittance evolution.

4.1 Simulation tools for electron cooling

As had been shown previously, it is not possible to fully model the electron cooling process without the use of numerical methods. The magnetised cooling force, which is important to determine the physical conditions in which the cooling process take place, can only be calculated through simulations. Several codes have been developed to simulate beam dynamics under the influence of electron cooling. Betacool is one of them, specifically designed to simulate cooling processes and has been in use since 1994 [116]. Betacool had been benchmarked in many machines [117–120], and implements several models of the cooling force including: Parkhomchuk, non-magnetised, Erlangen as well as user-written formulae.

More recently at CERN a novel tracking code called RF-Track has been developed for the optimisation of low energy accelerators in presence of space-charge effects [5]. It performs the calculations of the cooling force acting on the ions by numerically evaluating the formula derived by H. Nersisyan *et al.* in “Interactions between charged particles in a magnetic field” [69]. Both of the computer programs have been used to simulate

the behaviour of the cooling force varying the relative ion-electron velocity for numerous settings, corresponding to existing storage rings equipped with electron coolers.

4.2 Betacool

The code was developed by JINR (Joint Institute of Nuclear Research, Dubna, Russia) electron cooling group and has been successfully used to simulate electron cooling in many laboratories worldwide. The general goal of Betacool is to simulate long term processes in ion storage rings leading to a variation of the ion distribution function in six-dimensional phase space. The ion beam motion inside the storage ring is supposed to be stable and is treated in the linear approximation. The program represents the ion beam as an array of macro-particles which undergo a transformation of co-ordinates when interacting with the cooler. The cooling process leads to changes of the particle momentum components, which are calculated at each step of the dynamics simulation over time. The cooling force can be chosen from a library of formulae or user written. The code is written in C++ and was initially developed as a program for simulations of particle dynamics in ion storage rings under the action of the electron cooling force. Further development led to the inclusion of additional effects such as stochastic and laser cooling, and numerical algorithms, like the molecular dynamics tracking feature.

4.2.1 Betacool algorithms

The program includes three basic algorithms:

- **RMS Dynamics** which simulates evolution in time of the second order momentum of the ion distribution function (rms emittances) under the action of a few heating or cooling effects. Such effects are described in terms of characteristic times of the beam rms parameter variation.
- The **Model Beam** (MB) algorithm simulates the evolution of the distribution function shape. The beam is presented as an array of model particles. The evolution of the particle momentum components is described in terms of the Langevin equation [121]. Each heating or cooling effect is characterized by friction and diffusion components. The friction leads to regular momentum variation, the diffusion is simulated using a random number generator.
- The **Tracking algorithm** provides tracking of a particle array along the ring circumference with arbitrary steps using molecular dynamics technique for IBS simulation.

4.2.1.1 Model Beam Algorithm

For the analysis presented in this thesis, the beam dynamics simulations have been performed using the MB algorithm. It was based on the SIMCOOL code which was originally developed by V. Parkhomchuk et al. (Budker Institute of Nuclear Physics, Russia) [122]. This algorithm uses a few thousand test particles with arbitrary distribution and the action of IBS and electron cooling on each test particle is calculated. It can reach a very good accuracy when the distribution of the test particles is close to Gaussian. More recently, some modifications of this method were made for simulations of IBS in the specific case of non-Gaussian distributions [123].

The evolution of the ion distribution function is described using the Fokker-Plank equation [124, 125]. Friction and diffusion terms in the general case depend on the distribution function. However, in some cases, when the effects acting on the distribution function do not lead to change of its shape, the Fokker-Plank equation can be reduced to an equation of the second order moments of the distribution function. In the general case the Fokker-Plank equation can be reduced to the Langevin equation in invariant or momentum space [121]. The MB algorithm realizes a solution of the Langevin equation in momentum space using the Monte-Carlo method [126]. In the frame of this algorithm the ion beam is presented as a particle array. Each particle is described by a six co-ordinate vector: $\vec{X} = \left(x, \frac{p_x}{p}, y, \frac{p_y}{p}, s - s_0, \frac{\Delta p}{p}\right)$, where x and y are the horizontal and vertical co-ordinates, p_x and p_y are corresponding momentum components, $s - s_0$ is the distance from the bunch centre (in the case of coasting beam the distance from a reference particle), Δp is the particle momentum deviation from momentum of reference particle p . The action of each effect considered is simulated by calculating the particle momentum variation in accordance with the following equation [4]:

$$\left(\frac{p_{x,y,s}}{p}\right)_{fin} = \left(\frac{p_{x,y,s}}{p}\right)_{in} + \Lambda_{x,y,s}\Delta t + \sqrt{D_{x,y,s}\Delta t}\xi_{x,y,s}, \quad (4.1)$$

where p_s is the particle longitudinal momentum deviation (subscript *in* corresponds to initial momentum value, subscript *fin* relates to the final particle momentum after the action of the effect), Λ and D are the drift and diffusion terms for the corresponding degree of freedom, Δt is the step of the integration over time, ξ is a Gaussian random number at unit dispersion. The MB algorithm has a few obvious advantages in comparison with the Monte-Carlo one. The main one is simplicity and as a result high calculation speed. Therefore, the results of simulations using the MB algorithm can be effectively used for bench-marking of the Monte-Carlo calculation. The basic scheme for the MB calculations is:

1. In the first stage the beam is generated as a six-component vector, using user-defined parameters. The initial emittance and particle distribution are evaluated;
2. In a selected point of the ring, the impact of active effects is calculated and kicks are applied to the beam momenta (co-ordinates and angles of every particle are changed correspondingly);
3. The obtained vector of co-ordinates \vec{X} is multiplied by the transformation parameters of the optical elements of the whole ring per number of revolutions in the machine;
4. The final emittance and particle distribution are evaluated;

4.2.1.2 Kick procedure for IBS

IBS calculations are done using mean growth rates, which are calculated in accordance with the analytical Martini model and the ring optical functions loaded from a MAD output file. When the growth rates are known, one can calculate the mean square of the scattering angle. The mean square angle after one revolution in the ring is equal to

$$\langle \theta_i^2 \rangle = 2 \frac{\varepsilon}{\beta} \frac{T_{rev}}{\tau_i}, \quad (4.2)$$

where β is the beta function and τ_i is the characteristic growth time in the corresponding degree of freedom. Here, the angular deviation of the particle trajectory means relative momentum components: $\theta_{x,y} = \frac{p_{x,y}}{p}$, $\theta_s = \frac{\Delta p}{p}$. After N_{turn} revolutions in the ring the square of the scattering angle is equal to the sum of the square angles at each revolution. The variation of the particle trajectory angular deviation is then calculated in accordance with

$$\Delta \theta_i = \sqrt{\langle \theta_i^2 \rangle} \xi, \quad (4.3)$$

where ξ is again a random value from a unit normal distribution.

4.2.1.3 Runge-Kutta Methods

Runge-Kutta methods are a class of iterative methods, implicit and explicit, used in numerical analysis to integrate ordinary differential equations [127]. They are well known and reliable, based on the concept of using a trial step at the midpoint of an interval to cancel out lower-order error terms [128]. One of the most widely used methods for the solution of initial value problems is the fourth order Runge-Kutta (RK4) [129], which is one of the method that can be chosen in Betacool to solve the ion motion equations.

The procedure can be written as the following formula

$$y_{i+1} = y_i + \frac{1}{6}(k_1 + 2k_2 + 2k_3 + k_4), \quad (4.4)$$

where

$$k_1 = hf(x_i, y_i), \quad (4.5)$$

$$k_2 = hf(x_i + \frac{h}{2}, y_i + \frac{k_1}{2}), \quad (4.6)$$

$$k_3 = hf(x_i + \frac{h}{2}, y_i + \frac{k_2}{2}), \quad (4.7)$$

$$k_4 = hf(x_i + h, y_i + k_3), \quad (4.8)$$

$$(4.9)$$

and h being the step size. $F_j(X)$ represents the forces corresponding to external fields, which are derived by differentiating the Hamiltonian.

4.2.1.4 Mapping the cooling section

The map of the cooler takes the initial ion co-ordinates at the entrance and returns the ion coordinates at the exit of the cooler. The probability of ion loss due to recombination with electrons is also calculated, under the assumption that the ion velocity is less than the velocity of the electrons. The map of the cooler is used as a representation of the electron cooling effect acting on the ion distribution function. The action of the electron cooler is evaluated through two separate procedures. One of them computes the kick of the momentum components for all the ions in the model beam and calculates the particle losses due to recombination in the cooling section. The other procedure calculates the characteristic times of the ion beam emittance variation and the beam lifetime. The characteristic times can be evaluated using two models of the ion beam: single particle cooling times and cooling times for Gaussian beam obtained using the Monte-Carlo method.

The map of the cooler provides transformation of the ion co-ordinates from the entrance to the exit of the cooling section. This transformation is based on the solution of the ion motion equation in the cooling section. The ion motion inside a storage ring is described in the canonically conjugated variables:

$$\vec{X} = \{x, \theta_x, y, \theta_y, s - s_0, \theta_s\}, \quad (4.10)$$

where x, y are the horizontal and vertical co-ordinates,

$$\theta_{x,y} = \frac{P_{x,y}}{P}, \quad (4.11)$$

$$\theta_s = \frac{\Delta P}{P}, \quad (4.12)$$

$$P = \beta_{rel}\gamma_{rel}Mc \quad (4.13)$$

P is the longitudinal component of the reference particle momentum, $P_{x,y}$ are the transverse components of the ion momentum, ΔP is the longitudinal momentum deviation, $s - s_0$ is the ion longitudinal distance from the reference particle, $\beta_{rel} = V_0/c$, γ_{rel} are the relativistic Lorentz parameters, V_0 the velocity of the reference particle. Under the assumption, that the transverse components of the particle momentum are substantially smaller than the longitudinal one, the ion motion equations can be presented in the following form:

$$\begin{aligned} \frac{dx}{ds} &= \theta_x \\ \frac{d\theta_x}{ds} &= \frac{F_x}{Mc^2\beta^2\gamma} \\ \frac{dy}{ds} &= \theta_y \\ \frac{d\theta_y}{ds} &= \frac{F_y}{Mc^2\beta^2\gamma} \\ \frac{d(s - s_0)}{ds} &= \frac{\theta_s}{\gamma^2} \\ \frac{d\theta_s}{ds} &= \frac{F_s}{Mc^2\beta^2\gamma} \end{aligned} \quad (4.14)$$

where $F_{x,y,s}$ are the force components in the laboratory reference frame. The force acting on the ion inside the cooling section is the sum of the Lorentz force from the solenoid magnetic field, the electron beam space charge force, the cooling force and the force randomly distributed around zero value, which determines the diffusion in the electron beam.

4.2.1.5 Model of the cooler

The model of the electron cooler provides a choice of numerical methods for the integration of the system of equations in Eq. 4.14. The system takes into account the misalignment of the electron beam position in the cooling section. The system can be solved in the frame of two different models of the cooler:

1. Electron cooler as a thin lens,

2. Electron cooler as a system of non-zero length.

If the cooling force variation along the cooling section is negligible and the relative change of the particle momentum is small, the electron cooling section can be treated as a thin lens. This model assumes also that the ion transverse co-ordinates do not change during motion inside the cooler. Thus, the ion angle variation is calculated as following:

$$\Delta\theta = \frac{F}{Mc^2\beta^2\gamma}l_{cool} \quad (4.15)$$

where F is the cooling force in the lab reference frame, M is the ion mass, l_{cool} is the cooling section length, N_{turn} is the number of revolutions around the ring. The circulating particle co-ordinates are not changed inside the cooler. At non-zero length of the cooler the ion motion equation can be solved using one of the numerical methods: Euler or Runge-Kutta. Numerical integration of the ion motion equations is necessary in the case when the electron beam trajectory does not coincide with the ion equilibrium orbit. The cooler model provides the ion co-ordinates transformation from the frame referenced to the ion equilibrium orbit to the frame referenced to the electron beam trajectory.

The ion transverse co-ordinates relative to the electron beam trajectory are calculated as functions of its longitudinal co-ordinate (independent variable in the system of Eq. 4.14) in accordance with the angles between electron and ion beam axis

$$\begin{aligned} \theta_{e,i,x} &= \frac{x_f - x_0}{\delta l}, \\ \theta_{e,i,y} &= \frac{y_f - y_0}{\delta l} \end{aligned} \quad (4.16)$$

where the subscripts f and 0 correspond to final and initial co-ordinates of the electron beam trajectory in the sub-interval of length δl , calculated from the ion equilibrium orbit.

The ion velocity components in the frame referenced to the electron beam trajectory are corrected by these angles. We assume that the angles between the electron beam trajectory and the antiproton equilibrium orbit are sufficiently less than unity. In this case correction of the antiproton longitudinal velocity is not necessary.

Under the assumption that both angles are sufficiently smaller than the ion angle, the ion co-ordinates in the sub-interval are calculated as

$$\begin{aligned}
x &= x + x_0 + \theta_{e,i,x}s \\
y &= y + y_0 + \theta_{e,i,y}s \\
\theta_x &= \theta_x + \theta_{e,i,x} \\
\theta_y &= \theta_y + \theta_{e,i,y}
\end{aligned} \tag{4.17}$$

where the co-ordinate s is calculated from the entrance of the corresponding sub-interval.

The MB algorithm presumes that the ion geometrical co-ordinates do not change after crossing the cooling section and the action of the cooling leads to a change of the ion momentum components only. The kick in the ion beam momentum after crossing the cooler is calculated on the base of the map of the cooling section. The map transforms the initial ion co-ordinates in 6D phase space to the final ones

$$\begin{aligned}
M \cdot \vec{X}_{in} &= M \cdot \{x_{in}, \theta_{x,in}, y_{in}, \theta_{y,in}, (s - s_0)_{in}, \theta_{s,in}\} \\
&= \vec{X}_f = \{x_f, \theta_{x,f}, y_f, \theta_{y,f}, (s - s_0)_f, \theta_{s,f}\}
\end{aligned} \tag{4.18}$$

The MB algorithm ignores the ion geometry co-ordinate variation $(x, z, s - s_0)$ and multiplies the ion momentum components by the factor

$$\theta_\xi = \theta_{\xi,0} \times e^{\left((\theta_{\xi,f} - \theta_{\xi,in}) \frac{\Delta t}{T_{rev}}\right)}, \tag{4.19}$$

where $\xi = x, z, s - s_0$ and Δt is the step over time of the dynamics simulation.

4.2.1.6 Betacool modifications

Some modifications have been introduced in the program as part of this study in order to be able to accurately simulate the antiproton beam inside of ELENA. The negative charge of the antiprotons needed to be correctly inserted in the various cooling force formulae to evaluate the different effects acting on the beam. First of all the absolute value of the electric charge of the circulating beam was taken into account for the relevant calculations. The negative sign in the particle electric charge in fact created problems in the calculations of the cooling force (independently of the force model) and of the space charge effects. The modified impact parameter threshold in the Erlangen formula of the cooling force (see section 3.1.2.1) needed to be added. The maximum impact parameter below which the momentum transfer is twice the initial momentum is:

$$\rho_{min} = \frac{|Z|e^2}{m(V_{i,\parallel} - v_{e,\parallel})^2}. \tag{4.20}$$

The negatively charged ions of the simulated beam which satisfy this condition contribute to the force calculation with

$$\Delta F_{\parallel} = -\pi \rho_{min}^2 Z^2 n_e v_r (2m_e v_r) = -\frac{8\pi n_e e^4}{m v_r^2}. \quad (4.21)$$

Additionally a function to calculate the space charge effect for Gaussian distributed electrons was included in the program, similarly as for the other possible electron distributions.

4.3 RF-Track

RF-Track can simulate beams of particles with arbitrary energy, mass, and charge, even mixed, solving fully relativistic equations of motion. It can simulate the effects of space-charge forces, both in bunched and continuous-wave beams. It can transport the beams through common elements as well as through special ones: 1D, 2D, and 3D static or oscillating radio-frequency electromagnetic field maps (real and complex), flux concentrators, and electron coolers. It allows element overlap, direct and indirect space-charge calculation using fast parallel algorithms. RF-Track is written in optimized and parallel C++. It uses the scripting languages Octave or Python as user interfaces. The approach used to develop the RF-Track electron cooling routine is the following: the cooling force formula is based on the Erlangen group formulation in which the integrals are solved numerically using a Monte-Carlo technique and tabulated in appropriate 2D meshes (to be interpolated linearly at run time). In this case the, cooling force formula is described by

$$\vec{F} = -\frac{4\pi n_e Z^2 e^4}{(4\pi\epsilon_0)^2 m_e} \left\{ \underbrace{\iiint \left[L_F \frac{\vec{U}}{U^3} \right] f(\vec{v}_e) d\vec{v}_e}_{F_{unmagnetized}} + \underbrace{\int \left[L_M \frac{U_{\perp}^2}{U^5} \left(U_{\parallel} + \frac{U_{\perp}}{2} \left(1 - \frac{U_{\parallel}^2}{U_{\perp}^2} \right) \right) \right] f(v_{e\parallel}) dv_{e\parallel}}_{F_{magnetized}} \right\}, \quad (4.22)$$

where U is the ion-electron relative velocity, and

$$L_F = \frac{1}{2} \ln \left(1 + \frac{r_F^2}{r_{min}^2} \right), \quad (4.23)$$

$$L_M = \frac{1}{2} \ln \left(1 + \frac{r_{max}^2}{r_F^2} \right). \quad (4.24)$$

Here $r_F = \frac{\sqrt{U_{\parallel}^2 + \Delta_{\parallel}^2}}{\omega_e}$ is the pitch of the electron helix, $r_{min} = \frac{Ze^2}{4\pi\epsilon_0 m_e U^2}$ represents the minimum impact distance and r_{max} the maximum impact parameter calculated as

$$r_{max} = \min \left(r_{aprt}, \lambda_D \sqrt{1 + \frac{3U^2}{\Delta_e^2}}, U \Delta t \right), \quad (4.25)$$

where r_{aprt} is the beam aperture and λ_D is the Debye screening length. In the program, the ion beam is represented as an ensemble of macroparticles in 6D phase space in order to provide an accurate tracking and capturing non-linearities. The electron beam is represented as a fluid (plasma) on a 3D cartesian mesh that enables arbitrary electron densities and velocity distributions to be considered. The evolution of the electrons is performed following the Euler equation of fluid dynamics.

RF-Track was developed to optimize the design and beam transport of the TULIP backward travelling-wave linac [130, 131]. The main requirements were:

1. Being able to track particles in backward-travelling radio-frequency field maps;
2. Being able to transport protons as well as light ions in a fully relativistic regime;
3. Being able to dynamically tune the radio frequency parameters in order to perform non-trivial optimizations of the linacs transport efficiency.

Given the limited number of codes capable of tracking in oscillating electric and magnetic field maps, it was decided to develop a new ad hoc tool, optimized and tailored for the TULIP project.

The code was carefully designed to fulfil the above requirements and can offer 6D tracking in 3D electromagnetic field maps. The developer also focused on the possibility to maximise the transmission tuning of the following parameters:

- RF input power
- quadrupole strength
- quadrupole position
- input distribution.

RF-Track is a flexible and fast simulation program, fully relativistic, which allows the tracking of particles of any kind. It was successfully tested with electrons, positrons, antiprotons and ions at various energies, allowing the tracking of mixed-species beams [132–134].

By default the program uses a so-called “leapfrog” integration algorithm, which is fast, second-order and symplectic (it conserves the energy of dynamical systems). Leapfrog integration is a second-order method, in contrast to Euler integration which is only first-order, yet requires the same number of function evaluations per step. When the leapfrog algorithm is not accurate enough, RF-Track offers several other alternatives: explicit and implicit algorithms from the GNU Scientific Library [135] and exact analytic integration of the equations of motion in a locally constant electromagnetic field. These powerful high-level languages are ideal for numerical and scientific experimentations. They offer a large number of off-the-shelf toolboxes to perform complex numerical tasks: e.g., multidimensional optimizations, nonlinear fits, complex data processing, etc. The accelerator physics capabilities embedded in RF-Track, together with these expressive and rich scientific languages, make the simulation possibilities offered by RF-Track extensive.

A dedicated element called “Electron Cooler” has been implemented: it simulates the Coulomb interaction between a bunch of heavy particles and an arbitrary plasma. The electron beam is represented as a fluid (plasma) on a 3D cartesian mesh which enables arbitrary electron density/velocity distributions to be considered. Each cell (i, j, k) of the 3D mesh is characterised by: electron density, average electron velocity, electron transverse temperature and electron longitudinal temperature. Automatic tri-cubic interpolation of each quantity is performed, allowing it to work at any arbitrary location (e.g. ion positions). The integrals of the cooling force are then solved numerically, using a Monte-Carlo technique. Computationally it is relatively fast (about ten seconds), and it is performed just once.

Unfortunately the program does not include an IBS routine yet, making it unsuitable for long term beam tracking in the case of low energy storage rings, where IBS is a dominating factor.

4.4 Benchmarking

The RF-Track implementation of electron cooling and Betacool have been benchmarked against the experimental results detailed in [69]. As an example, the measurements of longitudinal cooling forces for a beam of fully stripped heavy $^{131}\text{Xe}^{54+}$ ions conducted at the electron cooler of the ESR storage ring [136] are shown in Fig. 4.1. Two different methods have been used here to determine the cooling force. At low ion velocities the cooling force is extracted from the equilibrium between cooling and longitudinal heating with RF noise. At high relative velocities between the rest frames of the beams the cooling force is deduced from the momentum drift of the ion beam after a rapid change

of the electron energy. Details of these methods are given in references [137, 138]. The measured cooling forces are shown in Fig. 4.1, where the data (black dots) are compared with simulations performed using both Betacool and RF-Track.

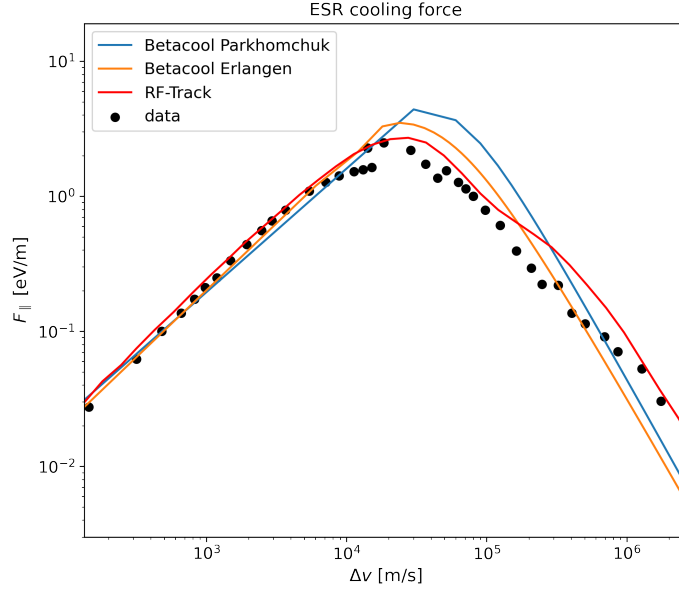


FIGURE 4.1: Cooling force for xenon ions as function of the relative ion velocity in the ESR storage ring at GSI. Measured data (black circles) are compared with simulations performed using Betacool (blue and orange lines) and RF-Track (red line).

The electron beam in these experiments has a typical density of $n_e \approx 1 \times 10^6 \text{ cm}^{-3}$ and can be described by an anisotropic velocity distribution with $T_{\perp} = m_e v_{th\perp}^2 \approx 0.11 \text{ eV}$ and $T_{\parallel} = m_e v_{th\parallel}^2 \approx 0.1 \text{ meV}$. The strength of the magnetic guiding field was $B = 0.1 \text{ T}$ over a drift region of length $L = 1 \text{ m}$. The measured longitudinal cooling force represents an average over the stopping forces on individual ions. For a comparison with the simulation models the cooling force is thus interpreted as the average $\langle F_{\parallel} \rangle$ of the component F_{\parallel} of the stopping force parallel to the beam axis (and the magnetic field) over the ion distribution $f_i(V_{\parallel}, V_{\perp})$ in the beam.

For low ion velocities this average is taken with respect to the transverse ion velocity only and the cooling force depends on the parallel ion velocity, i.e. $\langle F_{\parallel} \rangle = \langle F_{\parallel} \rangle(V_{\parallel})$. In the experimental procedure used for high ion velocities the cooling force is an average over the complete ion distribution. This average $\langle F_{\parallel} \rangle = \langle F_{\parallel} \rangle(\langle V_{\parallel} \rangle)$ depends now on the velocity of the centre of mass of the ion beam relative to the rest frame of the electron beam. To perform the average the distribution must be known. However, in the experiment this distribution was not determined in detail, but an estimate of the beam angular divergence was made: $\langle \vartheta_i \rangle \lesssim 0.5 \text{ mrad}$ [138]. This yields, after transformation to the rest frame of the ion beam, for the transverse ion velocities $\langle V_{\perp} \rangle \approx \gamma_{rel} \beta_{rel} c \langle \theta_i \rangle$,

where, γ_{rel} , β_{rel} are the relativistic factors related to the beam velocity in the lab frame and c is the speed of light. In the experiment considered here, the xenon ions had an energy of 250 MeV/u ($\beta_{rel} = 0.615$, $\gamma_{rel} = 1.268$) resulting in $\langle V_{\perp} \rangle \lesssim 1.17 \times 10^5$ m/s.

Very good agreement is observed at low relative velocities for both the codes. The semi-empirical Parkhomchuk formula curve overestimates the maximum of the force and expects it at higher relative velocity. As shown in Fig. 3.2, this formula exhibits some shift when varying the parameters, namely Δ_{eff} , while essentially retaining its shape. It is a derived formula, very useful for electron cooling approximation but not taking into account the different impact regimes considered in the BC model from which the Erlangen formula is derived. The Erlangen formula, based on the full equations of motion in the presence of a magnetic field, exhibits a much more intricate structure. The RF-Track implementation of the cooling force appears to better fit the data around the maximum and but the Betacool version is very similar. It is important to note that the deviations of the theoretical formulae for the cooling force (solid curves) from the ESR data (black circles) can be mainly ascribed to the rather unknown distribution function of the ions in the beam which has been modelled here in the form of an anisotropic Maxwell distribution. Indeed the actual velocity spread in ion beams may essentially differ from the Maxwellian.

The agreement of the simulated cooling forces with the experimental data is rather good. The comparison of the two codes with the data, considering the differences that can be essentially ascribed to the deviations of the model distribution function from the experimental distribution, validates the Erlangen formula. The different implementation of the aforementioned cooling force expression induce small deviations in the curves but overall a good agreement is observed.

In the next chapter the measurements and analysis of data from another storage ring will be shown, further improving the codes benchmarking.

Chapter 5

LEIR Measurements

In this chapter measurements performed on LEIR during the final measurement period before CERN's LS2 are detailed. This measurement campaign took place during Autumn 2018 and subsequently the diagnostics output was analysed off line using Python. The details of the data acquisition process are presented, followed by an explanation of how the collected data are treated and compared to simulations. Additionally, measurements of the cooling force performed by the CERN cooling group are used for simulation model benchmarking [139].

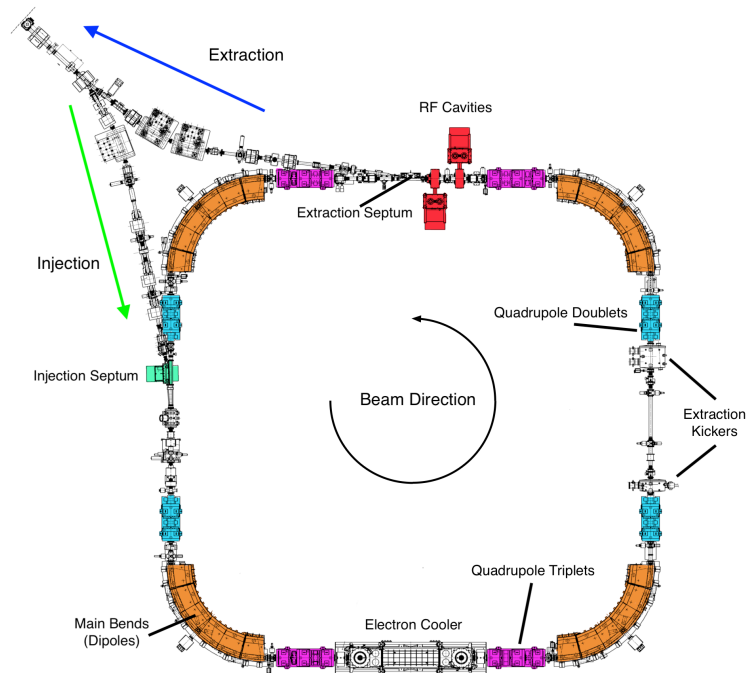


FIGURE 5.1: Layout of the LEIR machine and its main components

5.1 LEIR

The Low Energy Ion Ring (LEIR) is a 78.54 m accumulator ring (Fig. 5.1) and was first proposed in 1993 as a conversion of a then-existing machine, the Low Energy Antiproton Ring (LEAR). After the completion of the antiproton physics programme at the end of 1996, LEIR was modified for a final series of experiments to test the lead ion accumulation scheme that was foreseen for the LHC. The goals of the 1997 experiments were to test a new combined transverse and longitudinal multiturn injection scheme, the stacking of lead ions [140] and the optimisation of the electron cooling device for fast and efficient reduction of the beam emittance. Following the series of tests in 1997 [141], LEIR underwent a major upgrade in order to prepare dense bunches of lead ions by the transformation of ion beam pulses from the Linac3 into short high-brightness bunches using multi-turn injection, cooling and accumulation. A typical cycle in LEIR for lead ions is shown in Fig. 5.2. This cycle includes: injection, electron cooling acceleration and extraction.

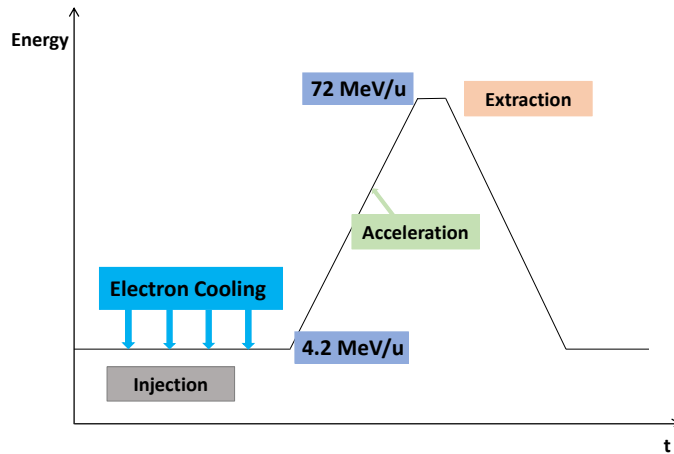


FIGURE 5.2: Schematic of a typical LEIR cycle.

The conversion of LEIR required new magnets and power converters, a high-current electron cooling system produced by BINP, Novosibirsk [142], broad-band RF cavities, upgraded beam diagnostics and vacuum equipment to achieve a pressure of $<10^{-12}$ mbar. The electron cooler is based on the design used by BINP for the electron cooler which it built for IMP Lanzhou in China and was delivered to CERN at the end of 2004. Subsequently a new electron gun design was implemented in 2006, opening up the possibility of investigating the influence of the electron beam size and density profile on the cooling process. It uses a high-perveance, variable-density gun followed by an adiabatic expansion provided by an additional solenoid. The high perveance aims at providing an electron beam with a high density in order to decrease the cooling time. The parameters for LEIR operations are listed in Table 5.1.

TABLE 5.1: LEIR parameters [143].

(Main) Ion particle	$^{208}\text{Pb}^{54+}$
Ring Circumference (m)	78.54
Energy (MeV/u)	4.2–72.2
Relativistic β_{rel}	0.09–0.37
Revolution frequency (MHz)	0.36–1.42
Vacuum (Torr)	1×10^{-12}
Intensity (Charges)	$1.5\text{--}2 \times 10^{10}$
Tunes	$Q_H = 1.82, Q_V = 2.72$

5.1.1 LEIR cooling force

For an accurate understanding of the cooling process, a detailed description of Coulomb collisions in a strong magnetic field are required, this is a topic of great interest both for accelerator and plasma physics. Coulomb collisions in a magnetic field are described by the cooling force which ions experience when moving through the electron beam of the cooler. This section presents measurements of the longitudinal cooling force — the component parallel to the magnetic field and the direction of propagation of the electron beam — for lead ions at injection energy in LEIR performed by the CERN cooling group in August 2018. In this experiment the longitudinal cooling force between the ions and the electrons was measured directly following the electron energy-step method [137], and benchmarked with simulations in Betacool and RF-Track. First, the ion bunch was cooled until two conditions were reached: its transverse emittance was reduced, and its average velocity reached equilibrium with the electrons' velocity. To improve the estimate of the cooling force the electron energy needs to be changed after cooling has been completed. In this way most particles in the ion beam have the same velocity and behave like a single particle, which enabled the measurement of the average cooling force. Once these two conditions were reached, the electron energy was changed rapidly by changing the cathode potential, creating a well defined velocity difference between ions and electrons. The energy of the electrons is controlled by varying the voltage of the electron gun grid. This velocity difference induced a cooling force that could be measured by tracking the variation of the ions' momentum in time, for different ion-electron velocity differences. The ion-electron velocity difference was measured as the difference in equilibrium ion momentum before and after the electron velocity step, determined by Schottky spectra from the change in revolution frequency per unit time. The cooling force was measured as the time derivative of the ion momentum during the first 50 ms after the step. When the relative ion-electron velocity is large, the ions experience the full range of forces.

TABLE 5.2: Nominal electron cooler parameters for LEIR [144].

Momentum (MeV/c)	88
Electron beam energy (keV)	2.3
Relativistic β	0.094
Electron current (mA)	600
Electron beam density (m^{-3})	4.3×10^{12}
B_{gun} (T)	Up to 0.23
B_{drift} (T)	0.075
Expansion Factor	3
Cathode radius (mm)	29
Electron beam radius (mm)	14-25
Electron beam temperatures (eV)	$T_{\perp} = 0.01, T_{\parallel} = 0.001$
Twiss parameters in the cooler (m)	$\beta_x = 5, \beta_y = 5, D_x = 0$
Flange-to-flange (m)	7
Drift solenoid length (m)	2.5

The change of the electron velocity causes an acceleration of the ion beam as a whole until the new average velocity is reached. Assuming that this drag force exerted on the ions is constant over the observed momentum interval, the cooling force is

$$F_{\parallel}(v) = \frac{\Delta p}{\Delta t} \propto \frac{\Delta f}{\Delta t}. \quad (5.1)$$

The frequency shift Δf is determined by a Schottky scan delayed by a time $\Delta t = 50$ ms with respect to the voltage step event. The scanned velocity range is $\Delta v = 6 \times 10^3 - 4 \times 10^5$ m/s. It is very important to consider the response time required for the electrons to reach the new velocity, thus the finite time response of the electron beam to a change in gun voltage is taken into account. Otherwise, considering the electron response as instantaneous with respect to a slower/faster one leads to an over/under estimate of the force in the high velocity range with respect to the cooling force peak. It was observed that the velocity rise time is about 20 ms, so the time step of 50 ms is sufficiently large to avoid this systematic error.

In Fig. 5.3 the experimental data (black circles) together with simulation results obtained with both Betacool (blue and yellow lines) and RF-Track (red line) are shown. The simulations were performed with the nominal beam parameters listed in Table 5.2.

The simulated force appears to be in good agreement with the data up to a relative velocity of 1×10^5 m/s. For higher velocities, the Parkhomchuk formula departs considerably from the data. As already observed for the ESR case, the Parkhomchuk approach,

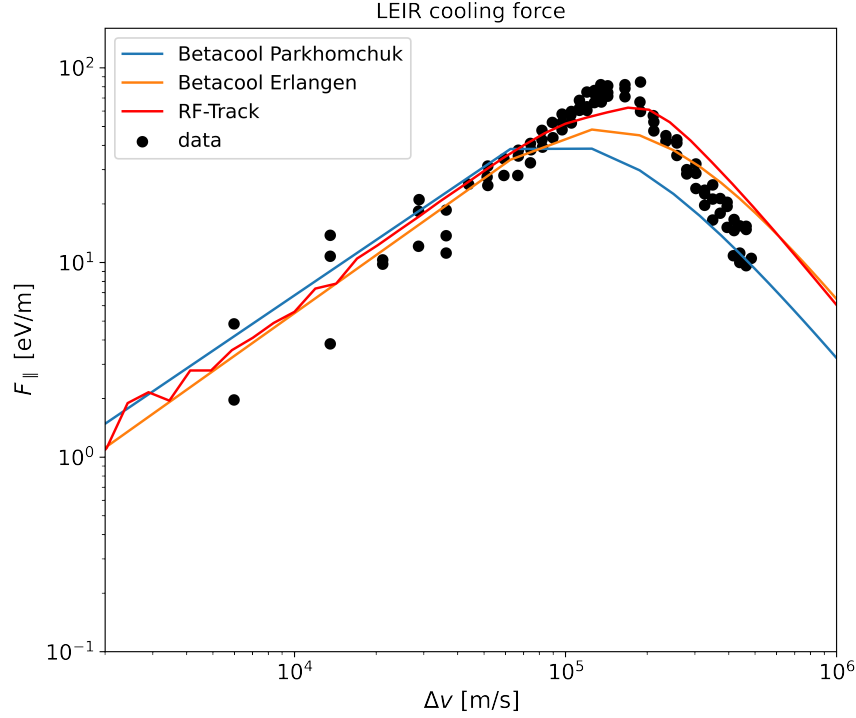


FIGURE 5.3: Longitudinal cooling force for LEIR lead ion beam as function of the relative ion velocity with respect to the rest frame of the electron beam. Black circles: experimental data. Blue and orange curves: simulations with Betacool. Red curve: simulation with RF-Track.

compared to the Erlangen formulation, underperforms in predicting the force peak. Betacool and RF-Track implementation of the Erlangen cooling force are in reasonable good agreement and exhibit similar behaviour.

5.1.2 Emittance Measurements

After injection into the machine the beam was electron cooled and stacked before being bunched and accelerated. At the end of the accumulation process, the transverse emittances and momentum spread of the beam reached an equilibrium between the cooling and heating processes such as SC and IBS. In order to benchmark the simulation model presented in chapter 3 and correctly evaluate cooling and heating effects in LEIR, measurements of the lead ion beam parameters were performed for the cooled ion beam. The beam was composed of a single injection from Linac3 ($1.5\text{--}2 \times 10^{10}$ ions). The transverse emittances were calculated with the optical functions of the model and the measurements of the transverse beam sizes obtained with a horizontal and a vertical

ionisation profile monitor (IPM) at a sampling rate of 200 Hz. IPMs measured the distribution of free electrons created by ionization of the residual gas (see section 2.5.2). These electrons were swept from the beam line by a transverse electric field, amplified by a microchannel plate (MCP), and collected on an anode consisting of 64 strips oriented parallel to the beam axis. The MCP is a device that is constructed from a glass substrate with channels cut through it.

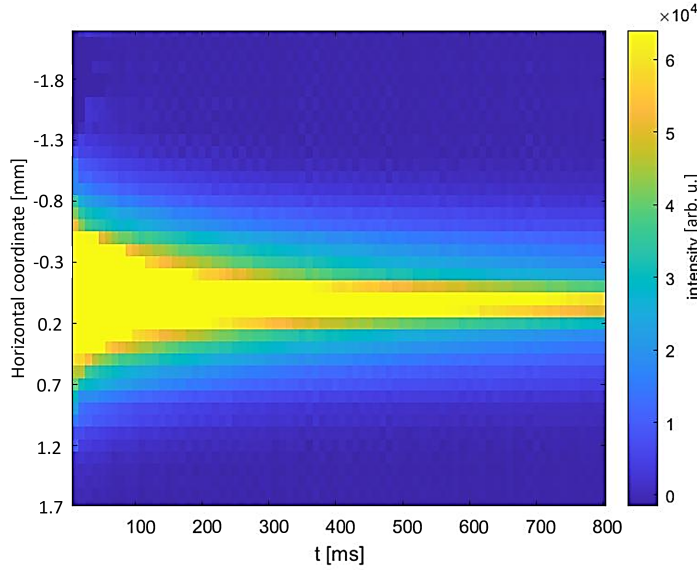


FIGURE 5.4: Lead beam profiles measured by the IPM during electron cooling. A shrinkage in the size is visible.

The MCP requires a potential between the two sides which creates an electric field in the channels. When a charged particle enters a channel on the input side of the MCP it will start an avalanche of electrons inside the channel which are expelled from the other side, effectively multiplying the input signal. The gain varies with the applied electric field and the properties of the MCP that is used. A plot of the raw data obtained by one of the IPMs is shown in Fig. 5.4. The electron cooler was on and it is clearly visible how the width of the beam was reduced over time. The data from the IPMs was then imported into Python, where the analysis code fitted a Gaussian function to the measured profile after subtracting noise signals as shown in Fig. 5.5. The emittance was calculated using the rms width of the fit and the beta function $\beta_{x,y}$ from ring lattice function calculations. The rms beam width $\sigma_{x,y}$ is related to the emittances by

$$\varepsilon_{x, \text{rms}} = \frac{1}{\beta_{x,y}} \left[\sigma_x^2 - \left(D_x \frac{\Delta p}{p} \right)^2 \right], \quad (5.2)$$

$$\varepsilon_{y, \text{rms}} = \frac{\sigma_y^2}{\beta_y}. \quad (5.3)$$

The beta functions at the IPM position are $\beta_x = 15$ m and $\beta_y = 6.5$ m and the dispersion D_x is 0.4 m.

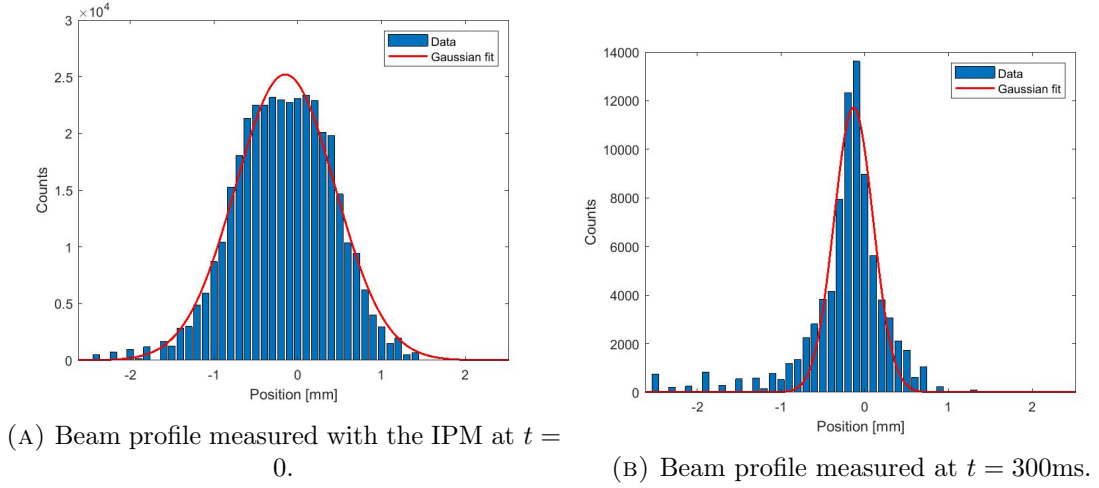


FIGURE 5.5: Example of the horizontal IPM signal transformation and Gaussian fit for emittance evaluation at different times during cooling.

To benchmark the simulation model for LEIR the emittance measurements taken during cooling for 500 ms were compared with simulations performed with Betacool. The data were taken from selected measurements where no instability arose during the cooling time observed and the intensity losses did not exceed 20%. The electron gun was regulated to produce an electron beam with a uniform transverse distribution, which is the basic operational setting for LEIR electron cooler. The resulting plots are presented in Fig. 5.6. The simulations show very good agreement with the observations which validates the simulation model and confirms that Betacool correctly evaluates the cooling force for the evolving ion beam.

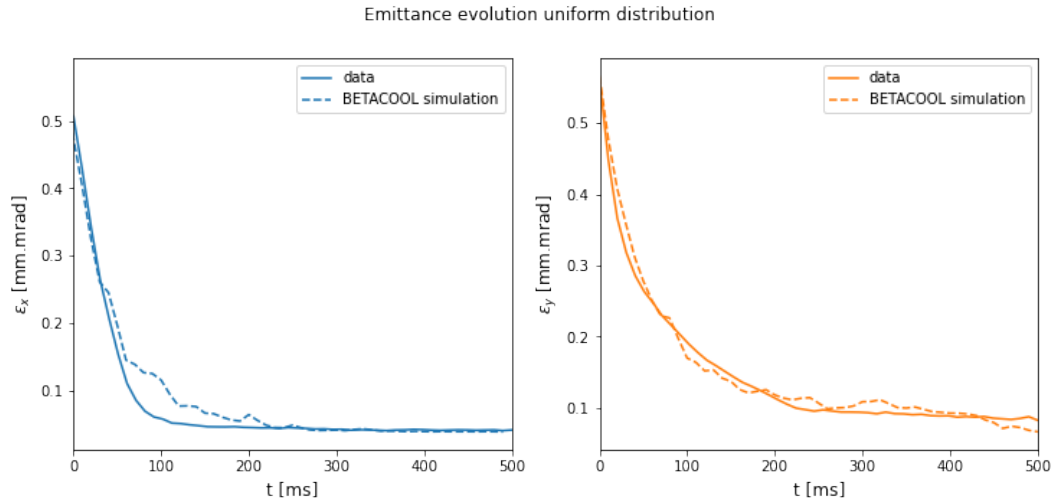


FIGURE 5.6: LEIR emittance measurements compared with Betacool simulations for uniform electron distribution.

5.1.3 Electron Beam Distribution

The same phase-space cooling characteristics measurements were performed to investigate the influence of the electron beam profile on the ion beam lifetime [145].

The cooling time is influenced by a number of machine and cooler parameters [146]. The electron current I_e , and the relative angle difference between the ions and the electrons θ , for example are two parameters that are accessible for experiments. This naturally leads to the question of whether the electron beam velocity distribution $f(v_e)$ can be controlled/modified.

The new electron gun installed in the electron cooler in 2006 is equipped with a control electrode used to vary the density distribution of the electron beam. The electron beam intensity and density distribution can be varied by applying voltages to the grid and control electrodes. Broadly speaking, the grid determines the intensity whilst the control electrode changes the density distribution by enhancing the emission from the edge of the cathode. The electron beam profile is determined by the ratio between the grid and the anode potential.

The electron beam density in the central part can be decreased without causing a reduction of the cooling rate of the whole ion beam. Thus the recombination losses in the core of the stored ion beam can be reduced. In this way the intense ion beam interacts with a hollow electron beam with a reduced central density that can decrease undesirable coherent oscillations. The electron gun with variable beam profile design was applied previously on the CSR cooler (IMP, China) [147]. The control electrode is situated near the cathode edge, so its potential strongly affects the emission from this area. By varying the potential of this electrode it is possible to vary the electron beam profile from the simple uniform cylinder distribution to a hollow or parabolic distribution. The ratio of the control to grid voltages determines the the shape of the electron beam, for example [148, 149]:

- $V_c/V_g = 0.3$ leads to a uniform distribution.
- $V_c/V_g = 1$ leads to a hollow distribution.
- $V_c/V_g = 0.08$ leads to a parabolic distribution.

The IPM data for the different electron distributions were extracted and analysed following the same procedures described in the previous section. The simulations were performed using Betacool with the different electron beam models but maintaining the same electron current hence the same overall electron density ($4.3 \times 10^{12} \text{ m}^{-3}$). The

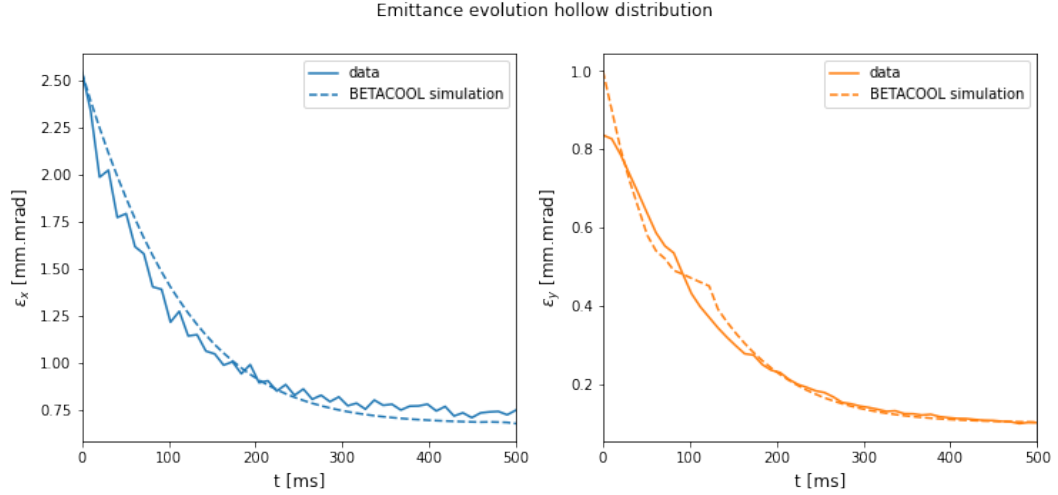


FIGURE 5.7: LEIR emittance measurements compared with Betacool simulations for hollow electron beam distribution.

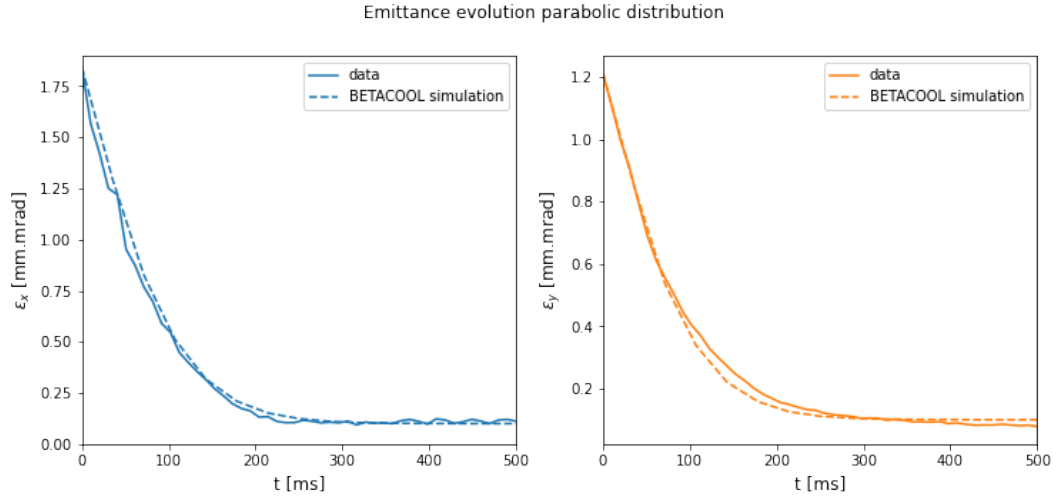


FIGURE 5.8: LEIR emittance measurements compared with Betacool simulations for parabolic electron distribution.

results of the measurements and simulations are shown in Fig. 5.7 for the hollow distribution and Fig. 5.8 for the parabolic case.

The simulations of the emittance evolution of the lead particle beam in presence of electron cooling show a very good agreement with experimental data. This indicates that the cooling process, together with the collective effects acting on the beam, are correctly taken into account in the simulation model. Since the agreement is consistently good for all the three different control electrode configurations, this also suggests that the Betacool electron beam models accurately represent the actual distributions used in the experiments and their resulting cooling forces.

5.1.4 Cooling maps

Traditionally, electron cooling is used with the heavy-particle and the electron beams overlapping concentrically, i.e. with the antiprotons' reference orbit aligned with the centre of the electron distribution. It was shown in chapter 3 how systematic errors related to element misalignment can interfere in the cooling process and how the electron velocity distribution has to be taken into account to accurately simulate the emittance evolution. In order to understand the impact of such misalignments on the performance of the electron cooler, simulations of the emittance evolution for different electron velocity distribution and with different beam displacements have been performed. From these scans of the parameter space “cooling maps” have been generated, representing the equilibrium emittance (achieved after few seconds with the electron cooler on) as a function of the orbit of the ion beam in the cooler. Translational and angular misalignments of the electron and ion beams are realised through the use of orbit bumps on the antiproton beam.

5.1.4.1 Orbit bumps

It is often necessary to shift the beam deliberately in a certain position of the accelerator without affecting the rest of the ring – this is called a closed orbit bump. It can be performed using small dipole magnets which are added to the existing lattice of the accelerator. For example one of the major performance limitations for operating the LHC at high energy are the so called Unidentified Falling Objects, or UFOs, presumably micrometer sized dust particles which lead to fast beam losses when they interact with the beam [150]. Aperture measurements revealed the presence of an unidentified lying object (ULO), at the bottom of the beam pipe. The interaction of this object with the beam triggered UFOs. To mitigate the problem a local orbit bump (horizontally and vertically) was implemented to bypass the ULO, which reduced the UFO rate and solved the problem [151]. At LEIR four orbit bumpers are installed, to modify the horizontal orbit. Those magnets are able to kick the beam by a certain angle. To control this effect LEIR is equipped with orbit knobs, which act on certain correctors to create orbit bumps and shifting the position of the ion beam inside of the accelerator pipes. The beam orbit position can then be measured and optimised using BPMs, also called pick-ups. Around the LEIR ring 32 ceramic-based electrostatic pick-ups are installed. Eight horizontal and vertical pick-ups are placed in the bending magnets, four combined pick-ups are installed in the straight sections and another four around the electron cooler. The electronics system consists of head amplifiers with three different gains followed by an analogue normaliser whose output is proportional to the average beam position. The front-end software has to read the digitised values from the normaliser and to compute

the 32 positions using scaling factors and offsets measured in the calibration process. Figure 5.9 shows the data from the horizontal and vertical pick-ups calibrated to zero offset and angle inside the electron cooler.

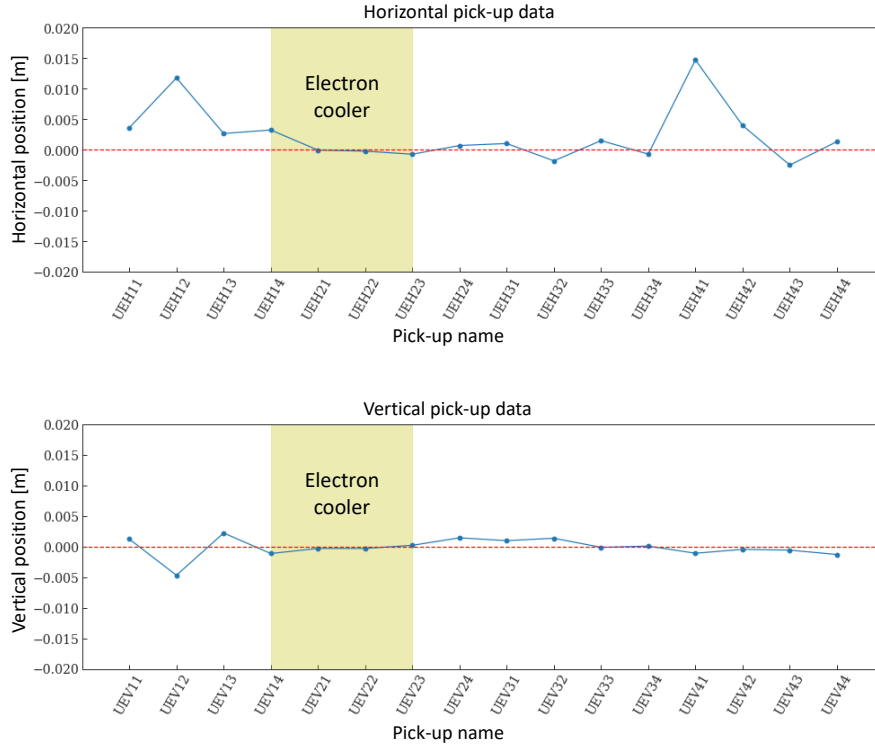
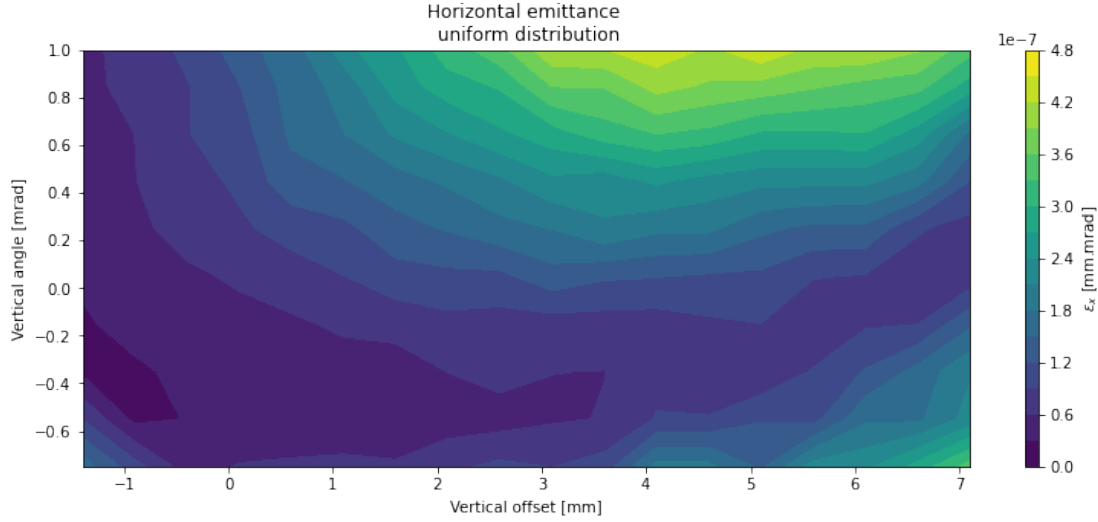


FIGURE 5.9: LEIR electron cooler bump knob, calibrated to no offset and no angle

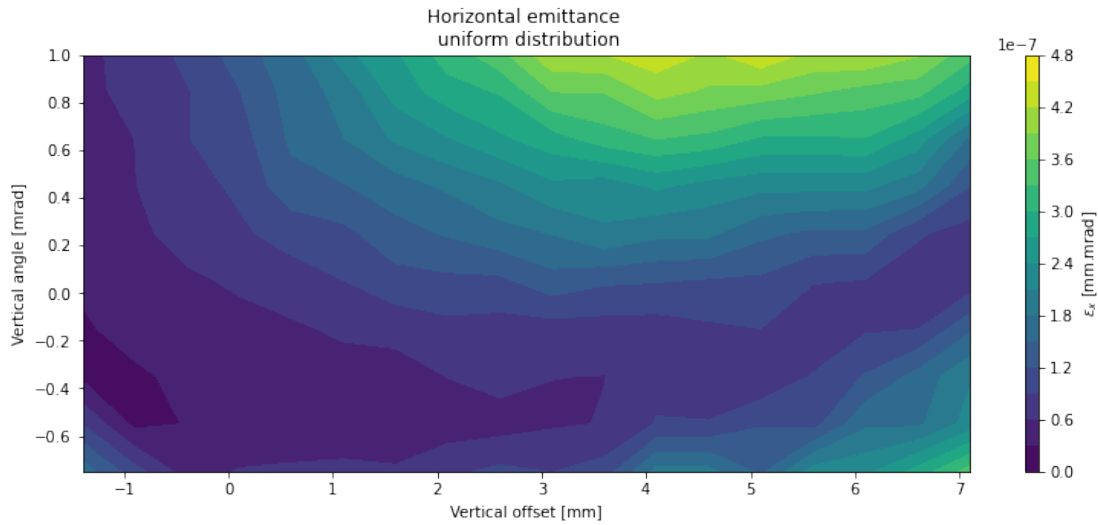
5.1.4.2 Results

The cooling map studies were performed with one injection into LEIR from Linac3. The offset and angle were systematically varied at each measurement cycle, spanning through a set of positive and negative angles and offsets. Due to beam stability issues the scans in the horizontal plane were of limited use and no additional beam time was available to repeat the measurements. The emittances were calculated at the equilibrium between cooling and IBS, which was observed after 500 ms of cooling. The resulting cooling maps obtained with the different electron beam configurations (uniform, hollow and parabolic) are shown in Figs. 5.10, 5.11 and 5.12.

In Fig. 5.10 are the cooling maps for the uniform electron beam case. There seem to be clear regions of larger and of smaller emittances, indicating regions of more or less effective cooling. It is interesting to observe that the maps are not symmetric, which could be explained by an existing misalignment inside of the cooler. This could be mainly explained due to a misalignment of the solenoid. If the magnetic field is not well



(A) Equilibrium horizontal emittance vs. vertical orbit, uniform electron distribution

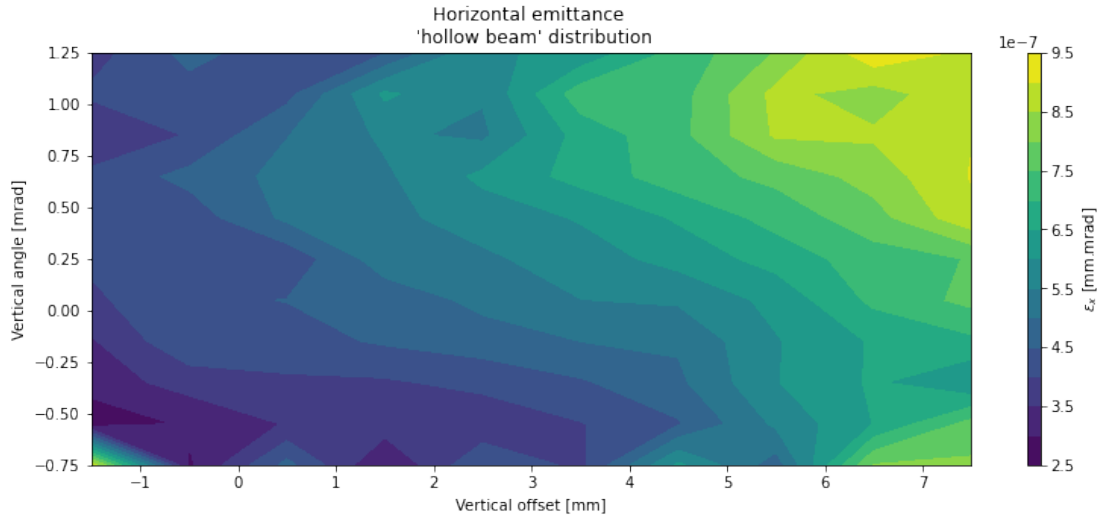


(B) Equilibrium vertical emittance vs. vertical orbit, uniform electron distribution

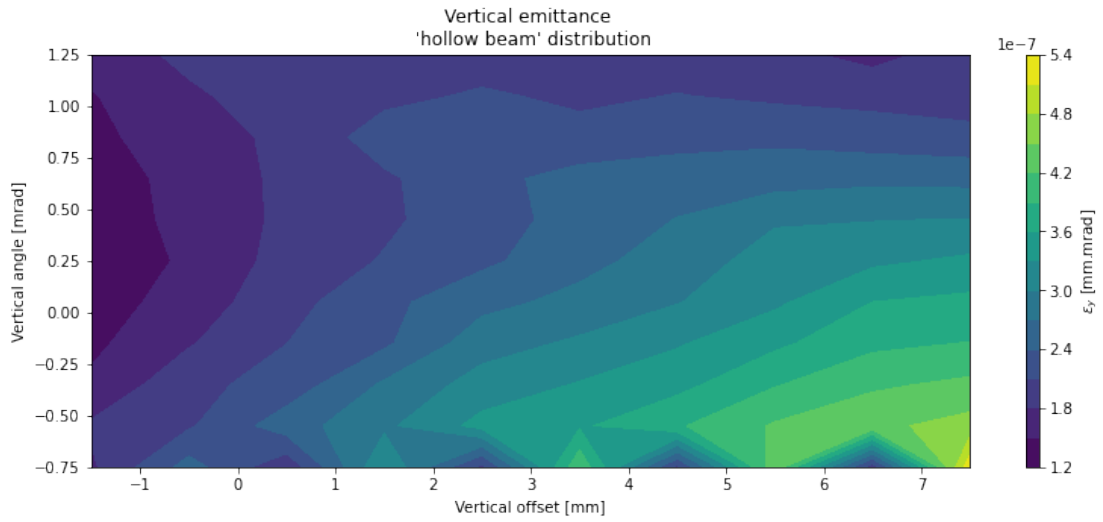
FIGURE 5.10: Vertical cooling maps for uniform electron beam distribution.

aligned the electron velocities will mix resulting in less efficient cooling (transverse and longitudinal temperatures).

The maps for the hollow electron beam configuration are shown in Fig. 5.11 where again an asymmetry is present indicating a systematic error present in the cooler. The most efficient cooling is located at a vertical offset of -1 mm, which suggests that the electron and ions fully overlap when the ion orbit is shifted a millimetre downwards. Compared to cooling maps for the uniform electron beam, the presence of a central area with a smaller electron density in the hollow beam distribution leads to a higher emittance at smaller offset. This is due to the fact that the misalignment of the electron and ions results in a fraction of ions being outside the interaction area of the electrons and a



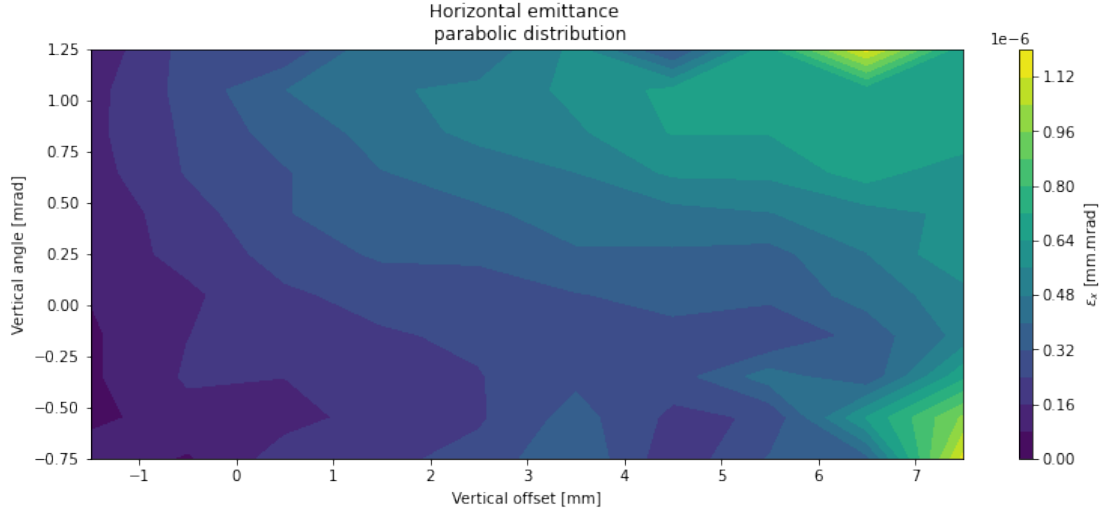
(A) Equilibrium horizontal emittance vs vertical orbit, hollow electron distribution



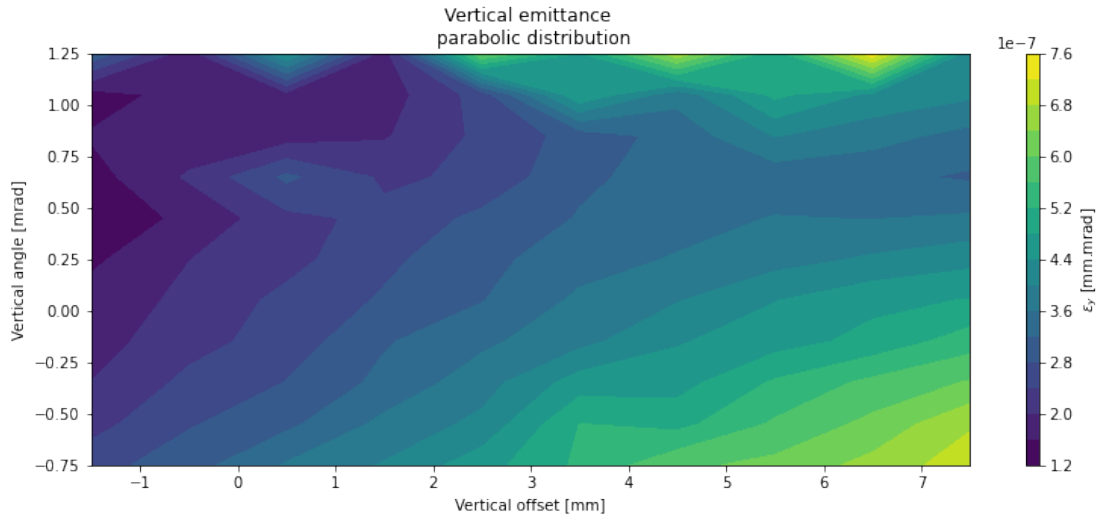
(B) Equilibrium vertical emittance vs vertical orbit, hollow electron distribution

FIGURE 5.11: Vertical cooling maps for hollow electron beam distribution

fraction of ions which still overlap experiencing a reduced electron density (in the centre of the hollow beam).



(A) Equilibrium horizontal emittance vs vertical orbit, parabolic electron distribution



(B) Equilibrium vertical emittance vs vertical orbit, parabolic electron distribution

FIGURE 5.12: Vertical cooling maps for parabolic electron beam distribution.

In the parabolic electron beam cooling maps (Fig. 5.12) the ≈ 1 mm shift in the negative vertical direction observed previously is confirmed by the smallest emittances being found about the vertical offset value of -1 mm. As for the hollow beam case the obtained equilibrium emittances are higher than the ones measured with the uniform beam. In this case is in the external part of the electron beam that the density decreases, hence the lead ions experience a cooling force induced by a smaller number of electrons when displaced from the nominal orbit.

This concludes the measurements taken at LEIR. The cooling force data were compared to simulations and showed good agreement with the Erlangen formula. This approach was then adopted for simulating the emittance evolution in presence of electron cooling for different electron beam profiles by acting on the control and grid voltages. The

Betacool simulations provided effective predictions for the emittances on both horizontal and vertical planes. The impact of misalignments and orbit displacements between electron and circulating ions was investigated by measuring the equilibrium emittances while acting on orbit bumps. The observed cooling maps, measured for uniform, hollow and parabolic electron distributions, demonstrated the most effective cooling when the beams have a vertical offset of 1 mm, suggesting a small imperfection in the alignment of the cooler.

In the next chapter, the stimulations performed for ELENA based on the model supported by the validation observed in the LEIR benchmarking are discussed.

Chapter 6

ELENA studies

In this chapter simulation studies carried for ELENA performance optimisation are presented. Only a handful of measurements on the ELENA machine suitable for antiproton beam dynamics studies were available during the preparation of this thesis. The data of interest are here presented and possible future measurements to confirm the simulation results are also discussed in the final section of this chapter.

6.1 ELENA cooling force

In this section simulations of the longitudinal cooling force in ELENA are presented. The simulations were performed with Betacool and RF-Track. The nominal operating parameters of ELENA's electron cooler used for the simulations are shown in Table 2.1. Figure 6.1 shows the cooling force simulated with RF-Track and for the different models available in Betacool. The curves obtained using Erlangen formula for protons in Betacool and RF-Track show good agreement. However, they neglect the negative charge of the antiprotons, the impact of which is calculated with the modified Erlangen formula as shown in section 3.1.2.1.

It is worth noting that the Parkhomchuk force model shows a similar peak as the modified Erlangen, provided that the semi-empirical effective temperature parameter Δ_{eff} is of an order of magnitude smaller than the electron temperatures (in this case $\Delta_{\text{eff}}=0.0001$ eV), but the relative velocity at which such peak is reached is much smaller. The inability to calculate Δ_{eff} for the ELENA case makes it a less reliable method for detailed beam dynamics calculations. Considering these differences, the modified Erlangen formula, analytically derived from the dielectric theory and the binary collision approximation is the most suitable for the ELENA case.

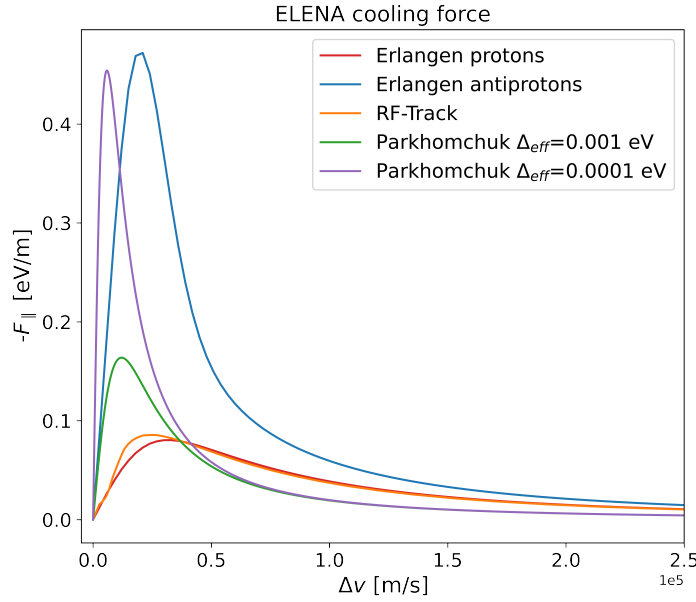


FIGURE 6.1: Longitudinal cooling force for ELENA as a function of the relative ion velocity with respect to the rest frame of the electron beam.

6.2 Measurements

To validate the accuracy of the simulations with data, measured emittances acquired with the ELENA scraper were used for comparison. The set of measurements together with the analysis were made by James R. Hunt and obtained with a scraper during the 100 keV plateau for an ELENA cycle [152]. The measurements were made in all transverse directions, twice at the same cycle time $t = 28.875$ s, with electron cooling on and off. This approach allows for investigation into the effects of the electron cooler. Electron cooling began at the start of the plateau at $t = 4.897$ s and so the measurements highlight the effects of 3.888 s of electron cooling.

The detector signals can be used to reconstruct the emittance as described in detail in reference [152]. The first step is to determine which quantity to reconstruct and when in the cycle, i.e. horizontal or vertical emittance. The analysis program can load two scraper measurements from opposing directions, in the same transverse plane, and both taken at a specific time. After transforming the detector data points in terms of scraper position, it is useful to plot the signals from the different detectors connected to the scraper blades. This allows one to determine which signals appear clearest for this measurement and to determine a single detector for use in the analysis program. It is necessary to apply cuts to the data to ensure that noise detected before or after the measurement is not included as large amplitude particles in the analysis. Typically for these measurements data were clipped within 25 mm. Scintillator and MCP data are

given as signal intensity at a specific time and are not cumulative. Working with a single measurement direction at a time, the first analysis step is to convert the detector data to a cumulative signal by a simple summation. All values in the cumulative signal array are then divided by the total sum in order to normalise and give a cumulative distribution function (CDF). The CDF is then converted to a probability density function (PDF), by differentiation through the finite difference method [153]. From here the algorithm reconstructs values for the beam size variance σ^2 and the mean position in the x plane of the intercepted particles for this particular scraper direction. This process is repeated for the scraper measurement in the opposite direction resulting in each direction which may then be inserted directly into the emittance equation:

$$\varepsilon_{\text{rms}} = \frac{1}{4\beta} \left[\sigma_+^2 + \sigma_-^2 + \frac{(\bar{x}_+ - \bar{x}_-)^2}{2} \right] - \frac{D^2 \sigma_\delta^2}{2\beta} \quad (6.1)$$

where β is the lattice function at the scraper location in the plane considered, \bar{x}_\pm is the mean value of the measured density distribution and σ_\pm^2 is the variance, D is the dispersion (which is 0 in the vertical plane) and σ_δ is the RMS width of the momentum offset distribution.

The results obtained are listed in Table 6.1. Analysis of the vertical data using the two scan algorithm gave emittances of 2.55 0.03 mm mrad and 0.53 0.01 mm mrad, without and with cooling respectively. After 3.9 s of electron cooling at 100 keV the vertical beam emittance is significantly reduced. At this point after cooling the beam is well approximated by a Gaussian distribution, due to the cooling being more effective and correcting IBS more in the core. Also, when the beam size is smaller so is the deviation in electron velocities interacting with the beam, resulting in more even cooling across the entire beam.

TABLE 6.1: Scraper measurements results for the ELENA 100 keV cooling plateau.

	Initial	Error	Final	Error
ε_x (mm mrad)	2.5	0.20	0.55	0.04
ε_y (mm mrad)	2.55	0.03	0.53	0.01

6.3 Emittance evolution

The model presented in Chapter 3 was implemented in the Betacool code. The obtained emittance evolution curve is compared with the scraper data in Fig. 6.2. The simulations

were performed 20 times and for each time step the mean value and standard deviation were calculated, in order to average out the effect of the random IBS kick.

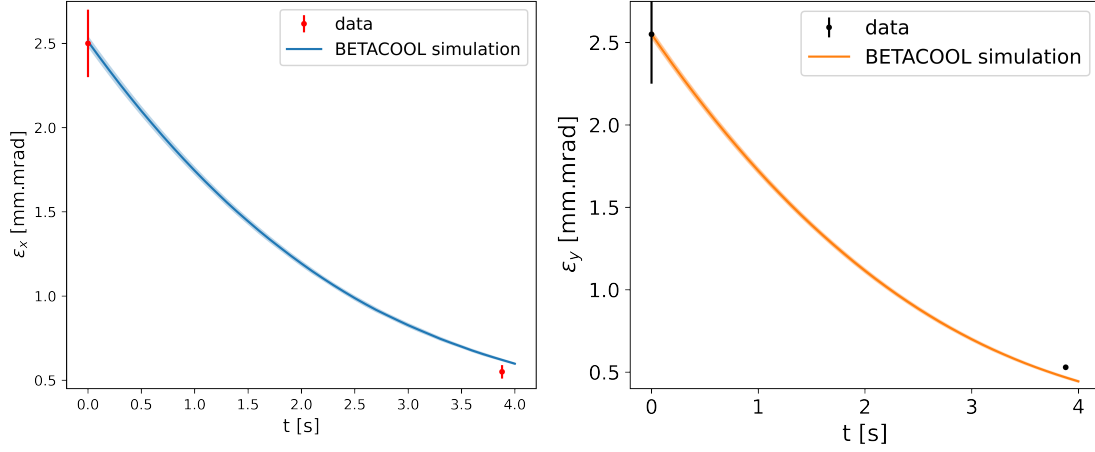


FIGURE 6.2: BETACOOL emittance evolution simulations for ELENA compared with scraper data.

Unfortunately it is clear that the model used for the simulations does not provide full agreement with the experimental data. This suggests that some of the effects may be incorrectly represented or an additional element influencing the beam evolution has been neglected.

As discussed in Sect. 3.2.4 and 3.2.5, the presence of misalignments and magnetic field imperfections — which even if controlled cannot be completely avoided in a real machine — have a big impact on a storage ring performance. The difference between the simulated and the measured emittances could be ascribed to the omission of such imperfections in the simulations. To verify if the model is indeed suitable for simulating the ELENA beam dynamics, alignment and magnetic field imperfections must be included and correctly evaluated.

6.4 Magnetic field

For fast and efficient cooling special attention must be paid to the quality of the magnetic field guiding the electrons from the gun to the collector. The ELENA electron cooler magnetic system was carefully designed and assembled to ensure the best cooling results. In this section measurements of the magnetic field in the electron cooler are analysed and implemented in the simulation model.

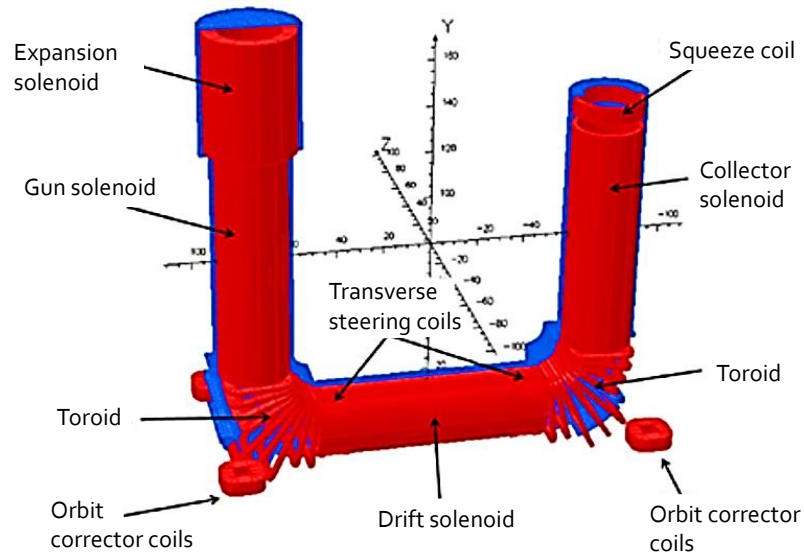


FIGURE 6.3: OPERA model of the ELENA cooler magnet system [83].

6.4.1 The electron cooler magnetic system

The performance of electron cooler in ELENA is greatly influenced by the properties of the electron beam. Careful design of the electron gun electrodes, the efficient recuperation of the electrons in the collector and the quality of the guiding magnetic field ensure an optimal performance of the cooler. The ELENA cooler is a compact device incorporating an adiabatic expansion to reduce the electron beam temperature as well as electrostatic bending plates for efficient collection of the electron beam. The complete setup of the main magnetic components can be seen in Fig. 6.3 and consists of [154]:

- An expansion solenoid to increase the magnetic field around the electron gun which is needed for the adiabatic expansion of the electron beam.
- Three main solenoids for the gun, drift and collector.
- Two toroid sections each made up of nine racetrack coils.
- A squeeze coil placed at the collector entrance to ensure that the electrons are focused as they are decelerated by the repeller electrode.
- Two orbit correctors at the cooler entrance and exit to compensate for the horizontal kick experienced by the circulating beam in the toroids.

The toroid coils come in three different sizes; two medium sized coils near the drift solenoid, three large coils to allow access by the antiproton beam as well as access for pumps and finally four small coils near the gun and collector solenoids. To compensate

for the larger size, the two outer large coils have one extra turn whilst the centre large coil has two extra turns. To guide the electron beam through the solenoid magnets and toroids, steering coils have also been integrated into the magnets. These provide a small deflection such that the electrons can be aligned to the circulating ion beam and steered correctly into the collector.

6.4.2 Magnetic field measurements

One of the few available measurements from ELENA electron cooler is the magnetic field inside of the drift chamber and the adjacent beam pipes, taken before it was installed in the ring. The measurements of the magnetic field \vec{B} were taken by the TESLA magnet division [155] on a cylindrical grid. The measurements started 180 cm upstream from the centre of the electron cooler and were performed every 5 mm until reaching 180 cm downstream, with a total extension of 360 cm. At each longitudinal position, a measurement was recorded every 5 mm from the centre to the maximum radial distance of 25 mm on the horizontal plane and 30 mm on the vertical plane. The measurements were performed using a Gaussmeter with 3-axis Hall probe (1 mG resolution in range up to 300 G, accuracy of 0.1%). The Hall probe holder was equipped with a mirror for precise alignment. It also allowed four possible rotational positions with three mounting points (0, 10 and 25 mm), used also in the opposite direction (-10 and -25 mm). The instrumentation included a balanced carbon fibre tube to hold probe still. The measurements were performed in the following steps:

- Power on until thermal equilibrium was reached.
- Probe carrier and tube driven and positioned with a coordinate measurement machine arm with a 0.5 mm accuracy.
- The angles at which the probe was placed were measured at the start of the line.
- The magnetic measurements for the different positions along line were taken.
- The angles at which the probe was placed at the start end of line were measured.

Precise probe alignments were made with an auto-collimator and spider fixtures.

Figure 6.4 shows the results of the measurements in the form of field maps. The three components of the field are plotted against the longitudinal (z) and the vertical (y) position on five distinct horizontal planes. The values of the magnetic flux density are in Tesla.

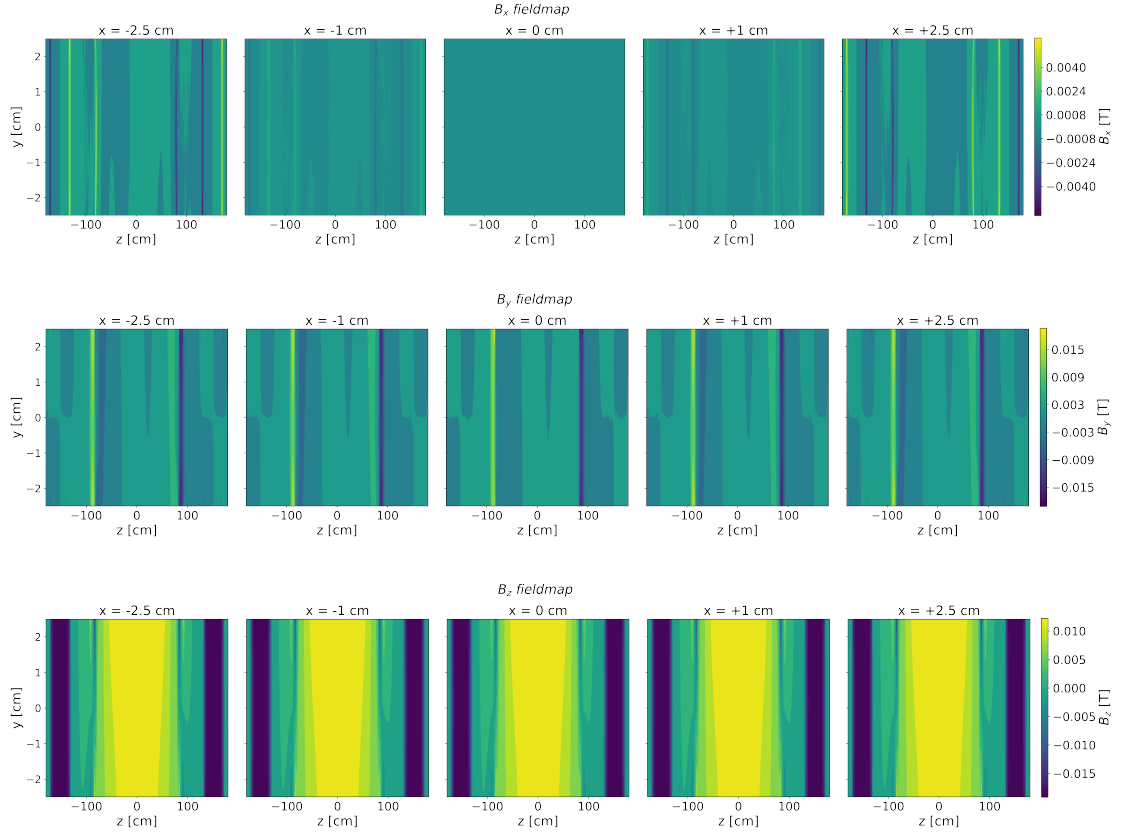


FIGURE 6.4: Measured magnetic field map inside of the ELENA electron cooler apparatus.

The field maps were then used to create a model in G4Beamline [156]. The software allows the placement of field maps through the `fieldmap` command, provided the map is in a grid format with a constant step in either $\{x, y, z\}$ or $\{z, r\}$. It reads an input file containing the values of the field components to define electric and/or magnetic fields. An electron beam was created in the simulation assuming an initial Gaussian distribution, at $z = -500$ mm, with the average energy of 55 eV. The electrons propagate through the central part of the electron cooler, experiencing the effect of the magnetic field.

With the command `virtualdetector` it is possible to generate a set of parameters of any track when it enters the physical volume of the Virtual Detector, an idealized perfect detector that detects every track that hits it, and measures all of the track properties with the resolution of a 32-bit float (including position, 3-momentum, particle type, event number, etc.). It is “virtual” because any material (including vacuum) can be used and it does not affect the tracking of particles. Figure 6.5 shows the magnetic field visualisation in G4Beamline, including the electron beam and virtual detectors. Multiple detectors were used to monitor the behaviour of the electrons along the magnetic field and track their position along the cooling drift.

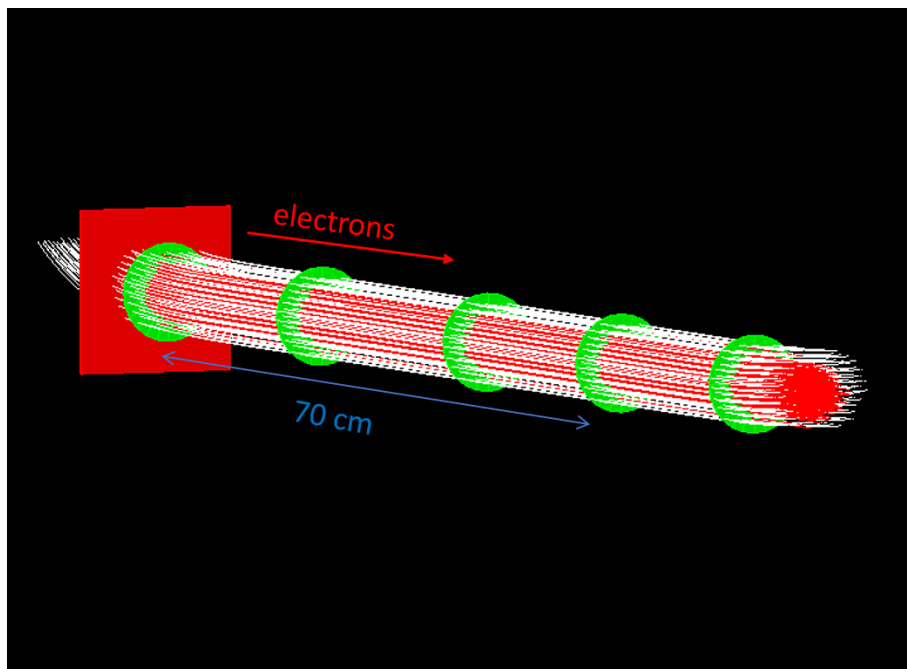


FIGURE 6.5: G4beamline visualisation of the electron beam (red lines) inside of the magnetic field (white lines). The red square represents where the electrons are generated and the green circles are virtual detectors

The output of the virtual detector contains the coordinates and momentum for each simulated particle, from which it is possible to reconstruct the electron beam distribution, represented by a histogram. Figure 6.6 shows the obtained electron beam profile at the beginning of the cooling drift.

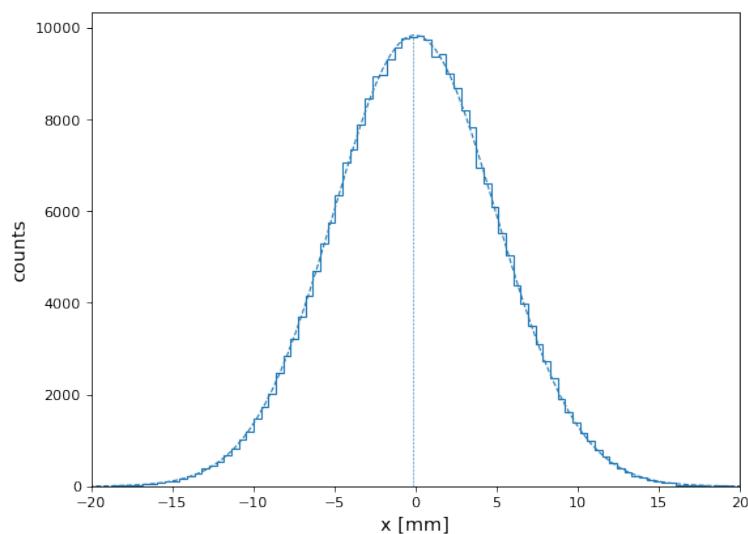


FIGURE 6.6: Profile obtained from the first virtual detector, next to the electron source, in the G4Beamline simulation

Comparing the distribution right after the electron source at the beginning of the drift with the output from the virtual detector placed at the end of the drift, 70 cm after, a

shift in the centre of the distribution is observed as shown in Fig. 6.7. The mean value for the Gaussian fit of the x position changes from being -0.150 mm to -0.954 mm, indicating a shift towards the negative direction of 0.804 mm. This is due to the tilt in the longitudinal component of the magnetic field, introducing a transverse drift to the electron motion. In order to accurately describe the ELENA electron cooling process, it is essential to take into account this misalignment.

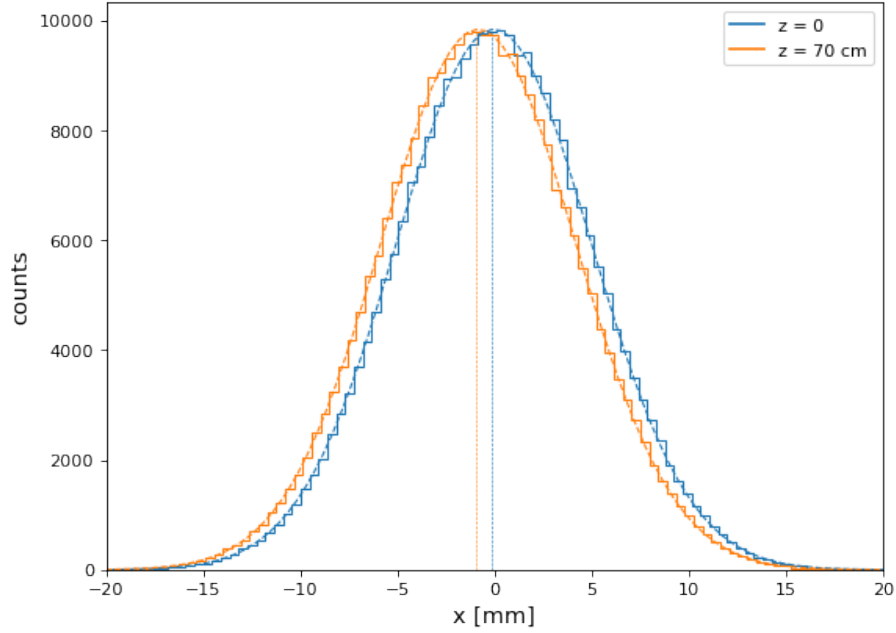


FIGURE 6.7: Comparison of the initial and final electron beam profile across the electron cooler. The orange distribution is detected at 70 cm, the end of the drift solenoid and good field region.

The Gaussian cylinder electron distribution model has been chosen as it showed better agreement with the data. It is reasonable to expect that the uniformity of the electron beam steered towards the cooling drift is not perfect and the Gaussian distribution model is likely more appropriate than the uniform distribution model. Two procedures to account for the observed angular deviation along the cooling section could be used in Betacool: a shift in the circulating and electron beam central axis or a solenoid error. In Fig. 6.8 and 6.9 it is shown how introducing misalignment of different values impact on the final achieved emittance on both the horizontal and vertical plane. The simulation where solenoid imperfection causing a shift in the magnetic field of 0.8 mm (green curve), as observed in the magnetic field simulation, was included show good agreement with the data from the scraper measurement. The simulations shown were performed considering the misalignment on the horizontal axis but the exact same behaviour was observed on simulations including a shift in the vertical direction.

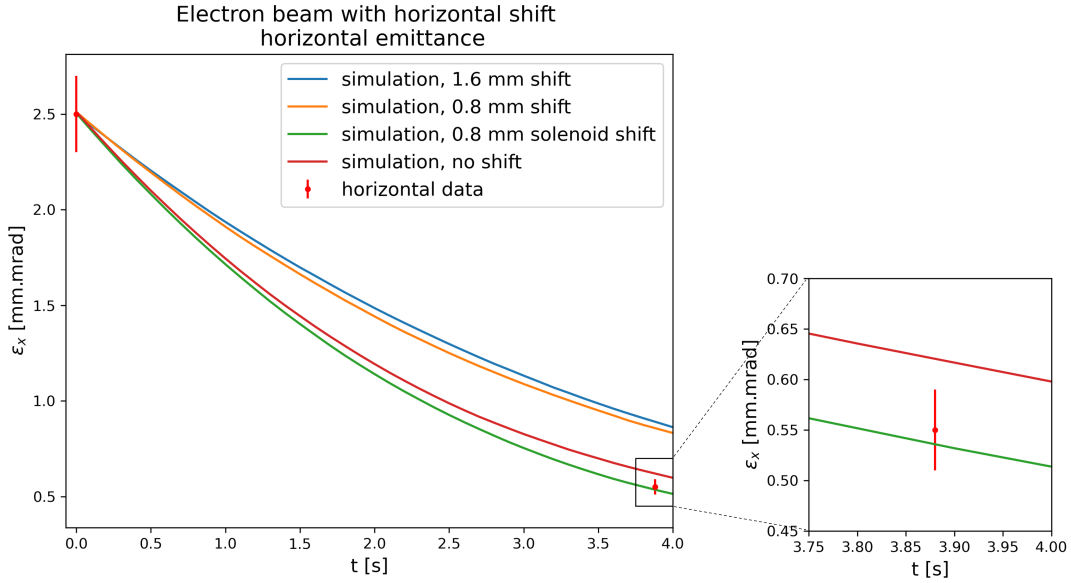


FIGURE 6.8: ELENA horizontal emittance measurements compared with Betacool simulations for different beam misalignment effects. The figure on the right shows the portion delimited by the black square in the larger plot.

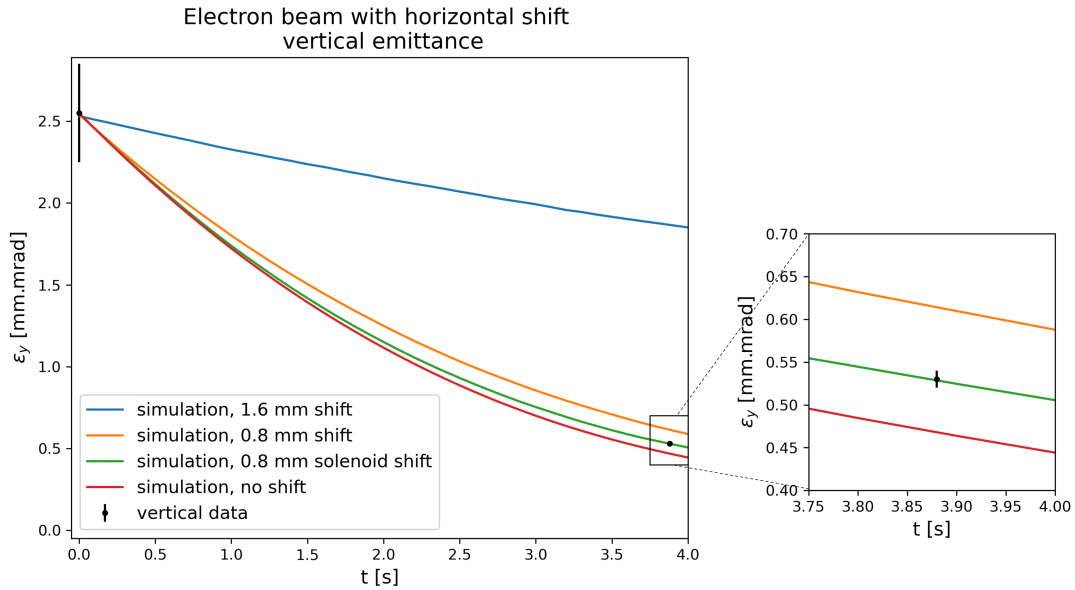


FIGURE 6.9: ELENA vertical emittance measurements compared with Betacool simulations for different beam misalignment effects. The figure on the right shows the portion delimited by the black square in the larger plot.

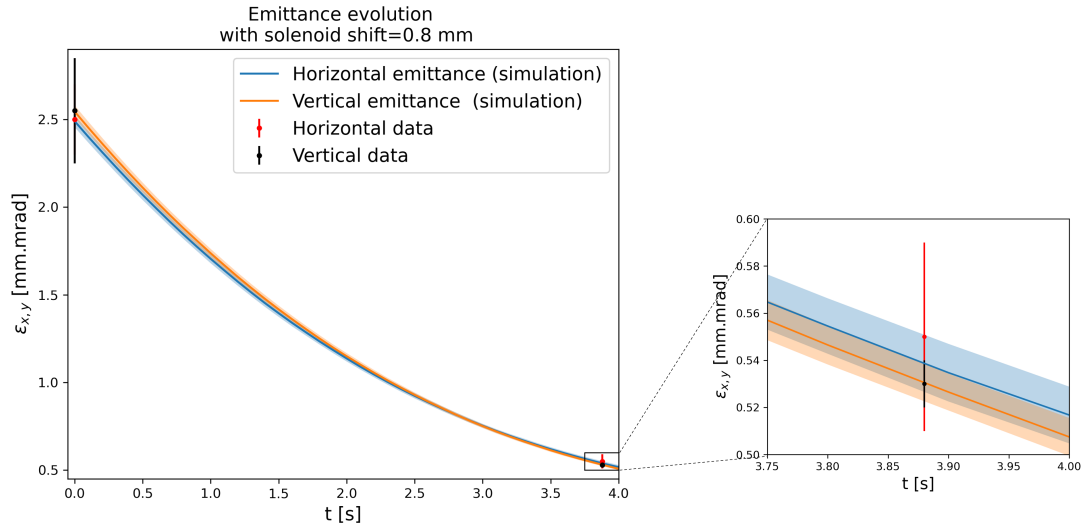


FIGURE 6.10: ELENA measurements compared with Betacool emittance evolution simulations. The figure on the right shows the portion delimited by the black square in the larger plot.

The code Betacool simulates the presence of solenoid errors by introducing coils transverse dislocation in respect of the solenoid central axis. The corresponding field inhomogeneities cause a misalignment between the electron and antiproton beam orbits, altering the relative velocity. In fact, the circulating beam faces a higher effective electron temperature because part of the longitudinal velocity is now experienced as an additional transverse velocity. Finally, the longitudinal and transverse degrees of freedom of the electron beam are mixed, which may lead to less effective cooling as described in Section 3.2.4. Figure 6.10 shows the ELENA emittance evolution for the second cooling plateau simulated with Betacool including a horizontal solenoid error of 0.8 mm.

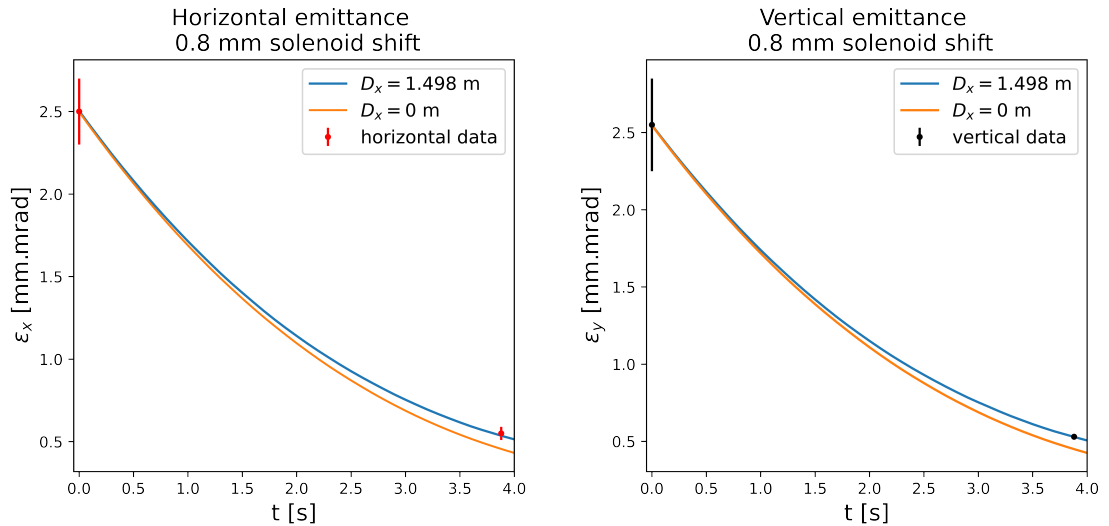


FIGURE 6.11: Betacool emittance evolution simulations for ELENA with 0.8 mm solenoid shift and $D_x=0$ m or $D_x=1.498$ m.

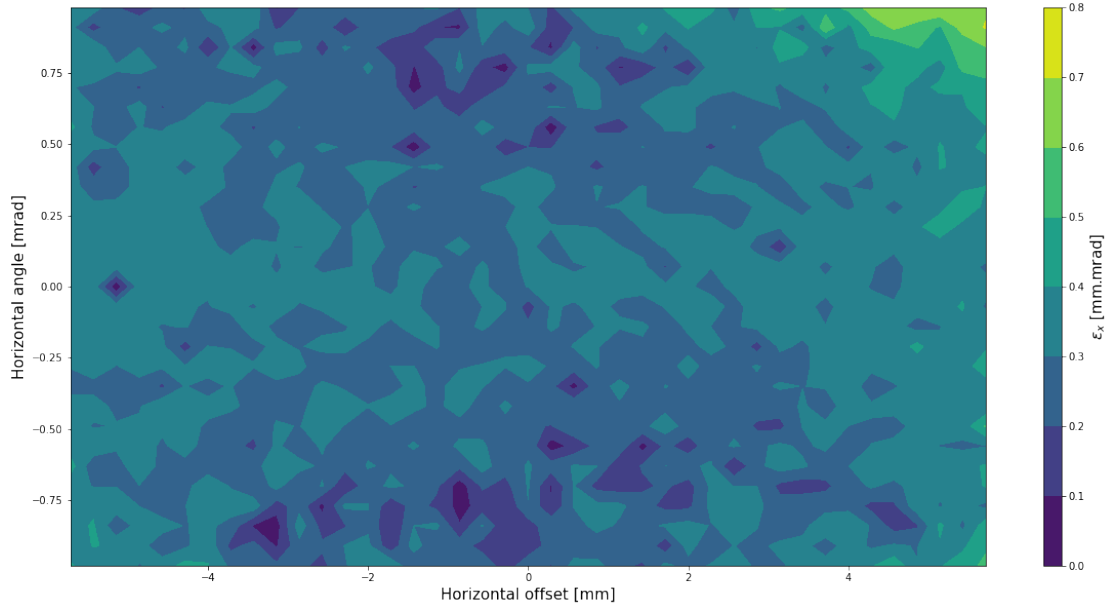
Observing the simulations it is notable that the presence of the solenoid error causes a larger final vertical emittance but a better cooling on the horizontal plane compared to simulations with no shift. This is related to the presence of a dispersion factor on the horizontal dimension. When simulating the beam evolution with the dispersion D_x set to 0, the final cooling emittance is improved on both x and y plane even in presence of the solenoid imperfection, as shown in Fig. 6.11.

6.5 Cooling Maps

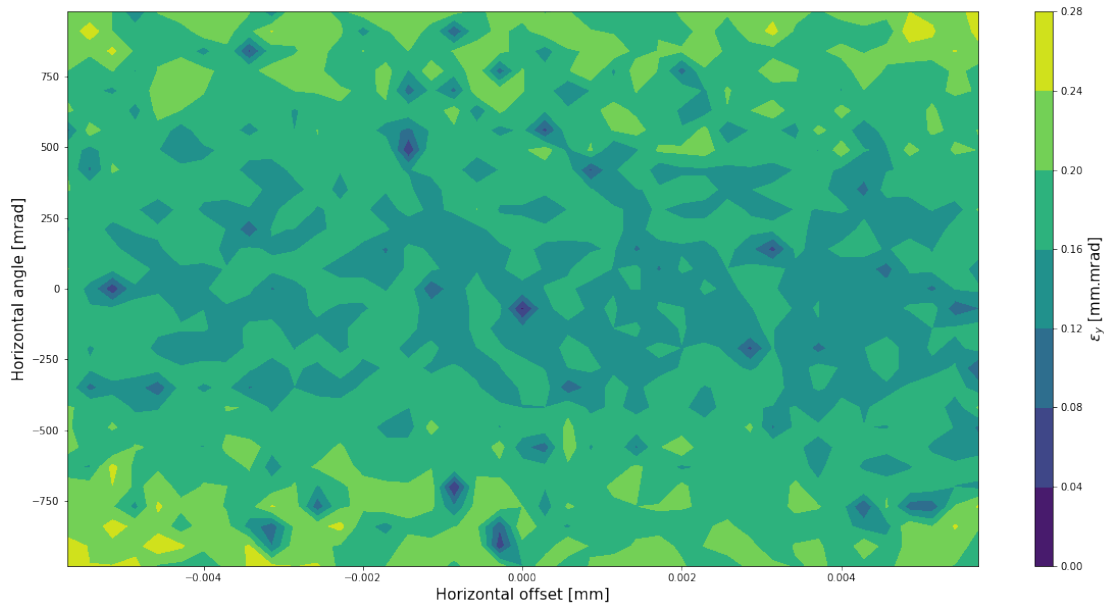
The analysis of the data and the simulation study suggest the presence of a misalignment inside the electron cooler. Likewise, the observation of the LEIR measured cooling maps hints that a similar shift is also present. In order to investigate the effect of various size of shifts and misplacements, cooling maps were simulated for the ELENA machine. For these simulations the different electron beam distribution models were employed. In this way the electron cooler performance could be better characterised. The simulations show a perfect symmetry between horizontal and vertical cooling maps, thus only the ones with translational and angular misalignments of the electron and antiprotons beams on the horizontal plane are shown.

Figures 6.12 and 6.13 show the simulated cooling maps in ELENA for uniform and Gaussian electron distributions, respectively. The behaviour appears very different. In the uniform distribution case the effects of orbit shifts and tilting angles seem to have a smaller impact. This can be explained by the fact that the local density is constant across the whole electron beam hence only big shifts can cause a large difference in the equilibrium emittances. In the Gaussian distribution case instead we can see how the impact is given by large tilting angles but not by large offsets. Even for a 4 mm shift the final emittance is the same as the aligned situation if the angle between the orbits is under the threshold of ± 0.5 mrad.

Figure 6.14a presents the cooling maps for horizontal emittance obtained with a hollow electron beam. In this case two areas of optimal cooling are found separated by an almost vertical strip of higher emittances. A similar picture is observed for the vertical emittance (Fig. 6.14b). The particular shape observable in these maps may be due to the fact that with the hollow electron distribution a weaker cooling force is exerted on the antiproton closer to the beam axis. When a shift is introduced the more dense external regions of the electron beam are overlapped with the centre of the antiproton beam ensuring a better cooling.

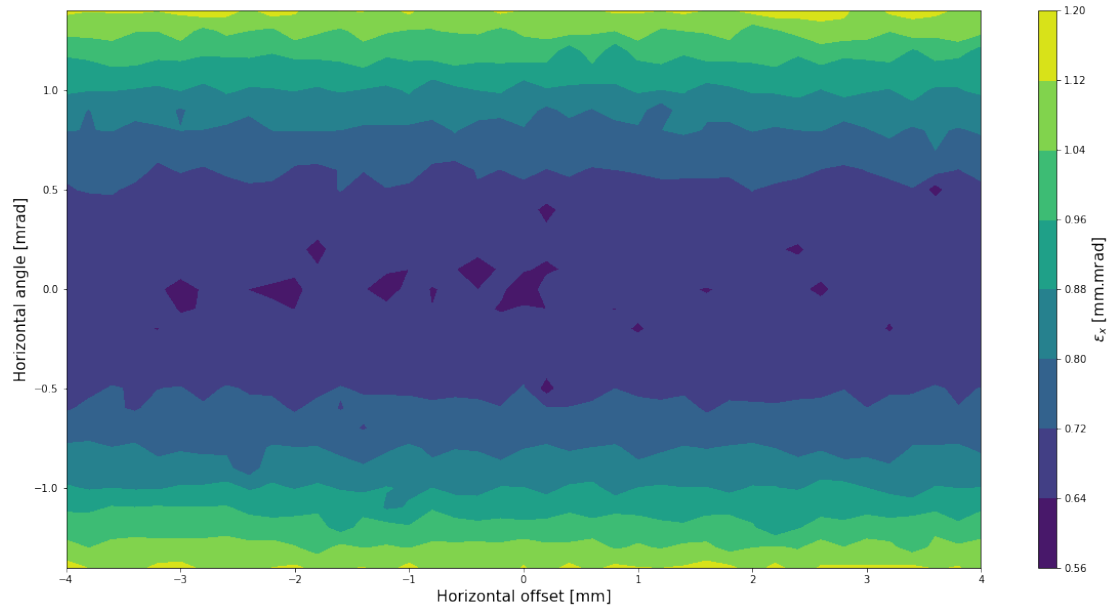


(A) Equilibrium horizontal emittance vs. horizontal orbit, uniform electron distribution

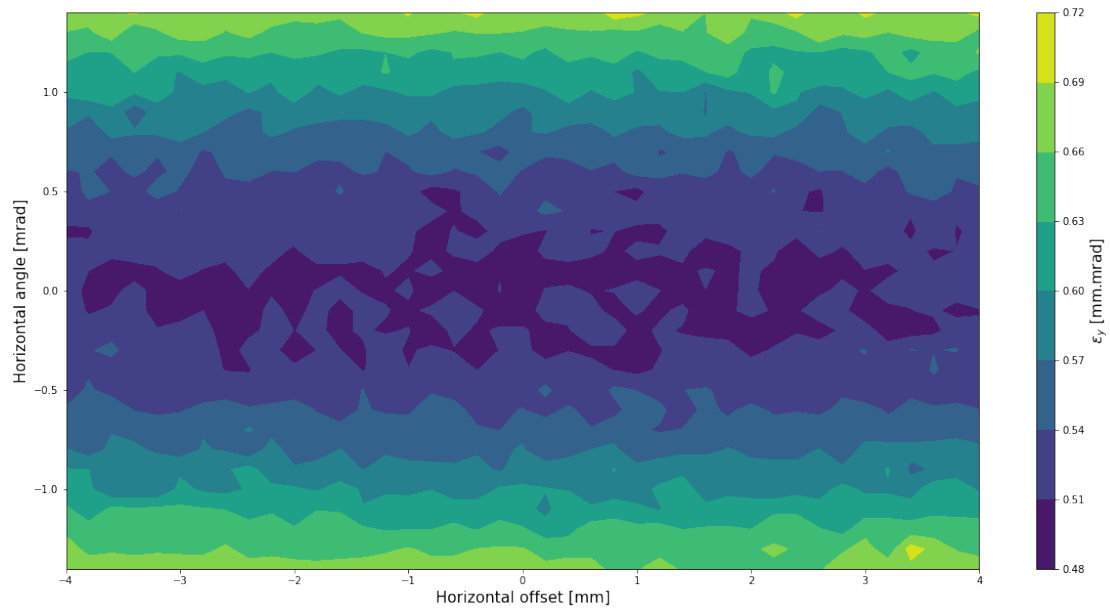


(B) Equilibrium vertical emittance vs. horizontal orbit, uniform electron distribution

FIGURE 6.12: ELENA cooling maps for uniform electron beam distribution.

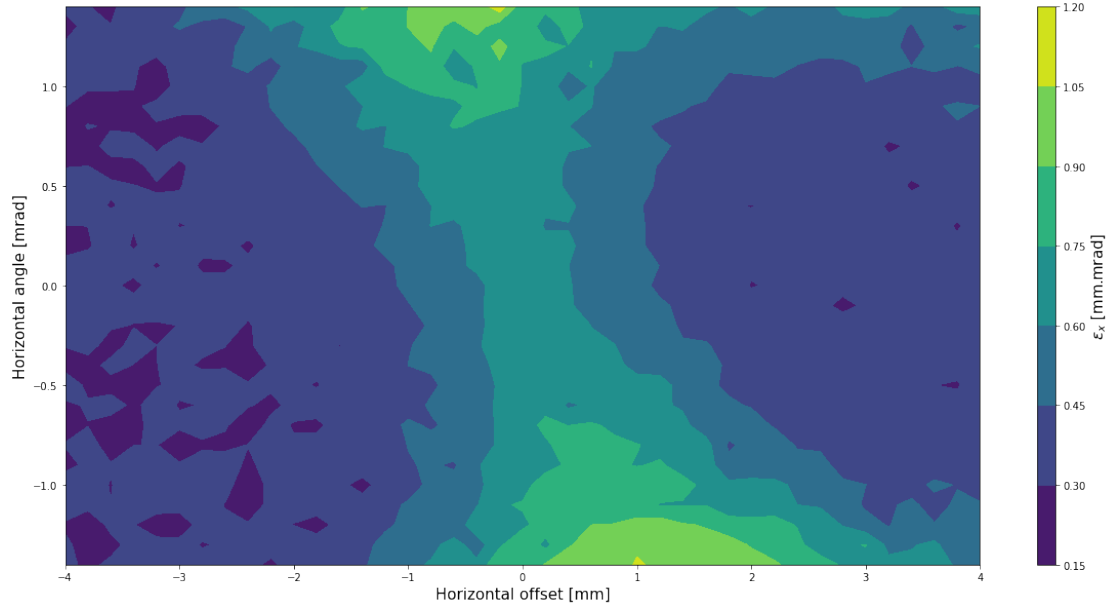


(A) Equilibrium horizontal emittance vs. horizontal orbit, Gaussian electron distribution

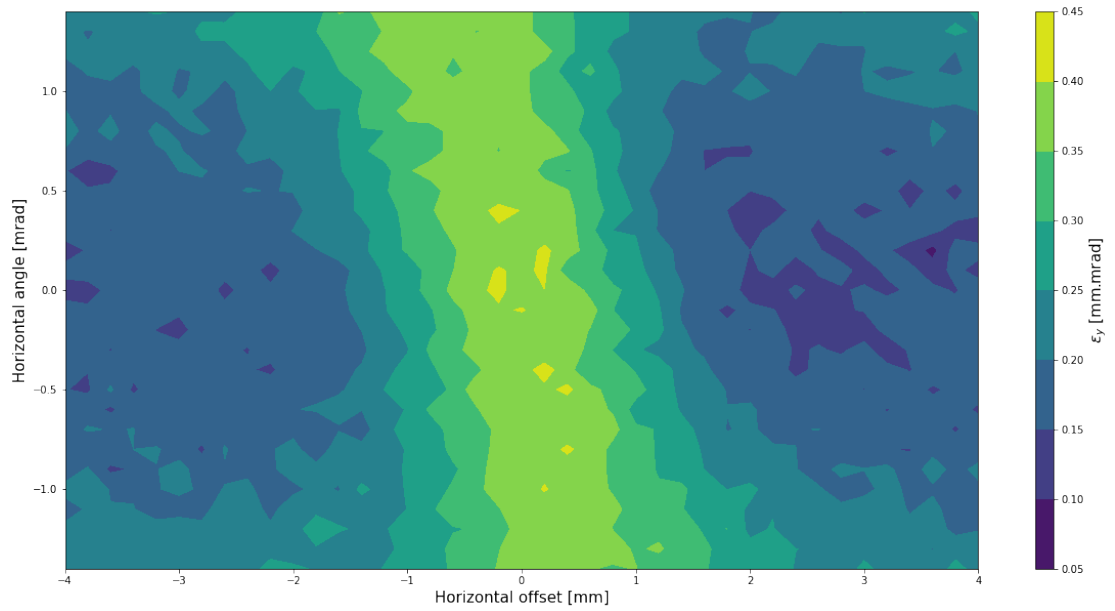


(B) Equilibrium vertical emittance vs. horizontal orbit, Gaussian electron distribution

FIGURE 6.13: ELENA cooling maps for Gaussian electron beam distribution.



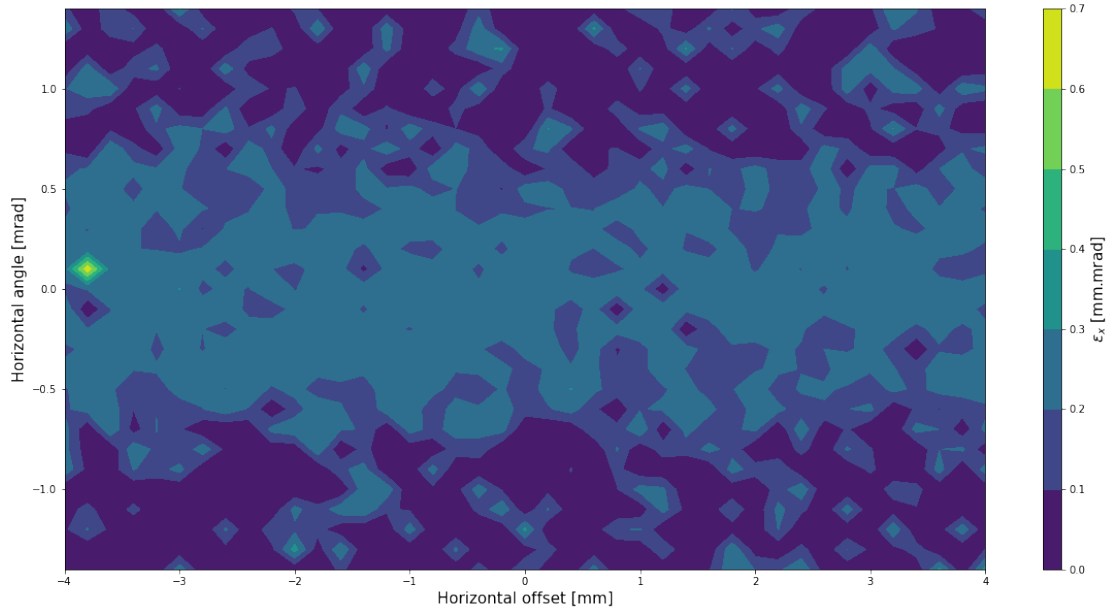
(A) Equilibrium horizontal emittance vs. horizontal orbit, hollow electron distribution



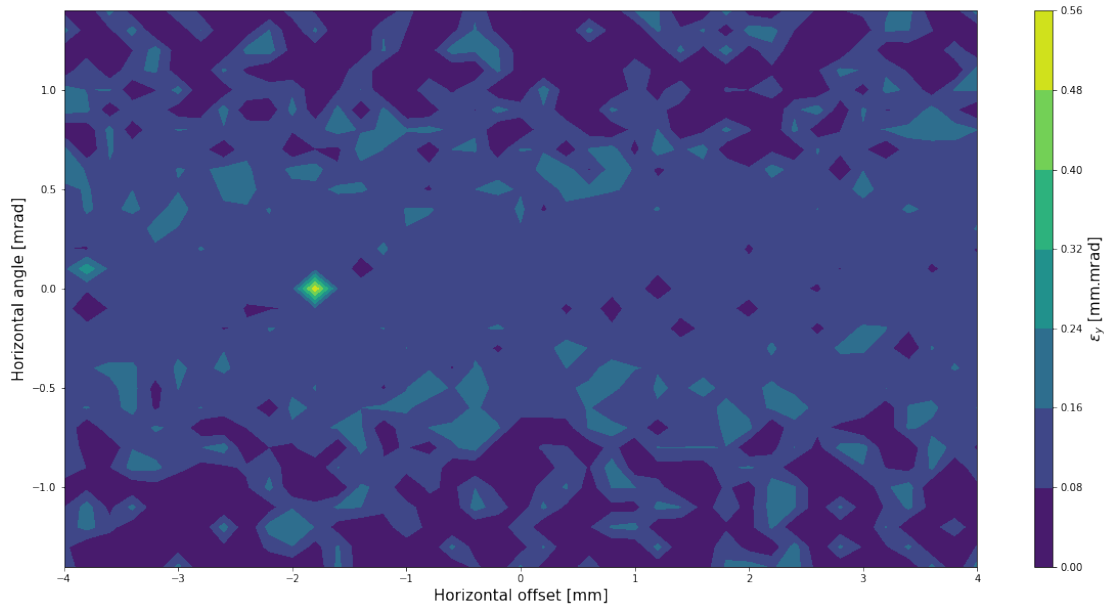
(B) Equilibrium vertical emittance vs. horizontal orbit, hollow electron distribution

FIGURE 6.14: ELENA cooling maps for hollow electron beam distribution.

Figure 6.15 shows the cooling maps simulated using a parabolic electron beam distribution. The regions of more and less effective cooling are distributed similarly to what is observed with the uniform electron distribution, but with smaller fluctuations. At bigger angle values but the horizontal and vertical emittances are slightly reduced. This could be related to the very intense core of the parabolic electron beam that might over-cool the central part of the ion beam enhancing the IBS and resulting in an increased emittance. When instead a tilting angle is introduced the cores are not fully overlapped for the entire drift length and this effect is mitigated. It is also notable that there are two points of higher emittances, the cause of which can be attributed to the IBS blow-up caused by the aforementioned unstable over-cooling.



(A) Equilibrium horizontal emittance vs. horizontal orbit, parabolic electron distribution



(B) Equilibrium vertical emittance vs. horizontal orbit, parabolic electron distribution

FIGURE 6.15: ELENA cooling maps for parabolic electron beam distribution.

6.6 ELENA Lifetime limitation effects and mitigations

In order to improve the lifetime of antiprotons in ELENA, one should mitigate the impact of limiting effects. For instance, the extraction energy of 100 keV represented the optimal solution to sensibly increase the trapping efficiency of the experiments without meeting the very strong limitations associated with lower energies. These include: increased IBS, more stringent limitations due to transverse space charge, even lower vacuum would have been required together with the difficulties to manufacture stopping foils thinner than $1\text{ }\mu\text{m}$ needed for the trapping.

The ELENA lattice had been designed to meet requirements common to all synchrotrons, such as suitable tunes and sufficient acceptances, and to deal with strong focusing due to bending magnets typical for small machines. The solution adopted is a machine with hexagonal shape and, with two straight sections without quadrupoles for the electron cooler and the injection elements. The other four straight sections host two fast deflectors to extract the beam towards the experimental areas, one wide-band RF cavity and one wide-band longitudinal diagnostic device, among three families of quadrupoles for optics control [68]. The three quadrupole families allow for the adjustment over a certain range of the transverse tunes to avoid resonances and of the dispersion at the electron cooler in order to optimise the cooling process.

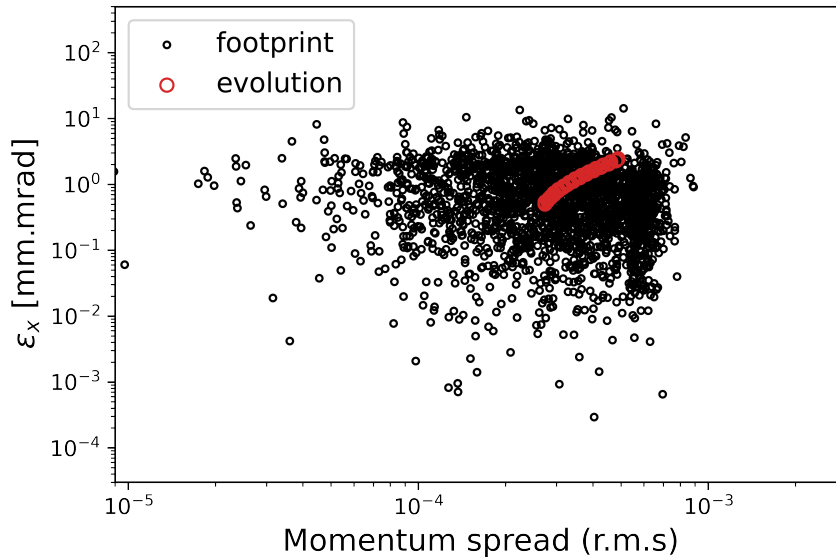


FIGURE 6.16: Distribution of the ELENA antiproton beam in 3D phase space (dP/P , ε_x). Scattered points (black) are particle invariants simulated in the frame of the model beam algorithm. Evolution of rms emittance and momentum spread in time is outlined by the red circles.

Nominal acceptance values of $A_{x,y} = 75$ mm mrad have been chosen for the ELENA ring which are enough to accommodate the beam from the AD and to decelerate it avoiding beam losses down to a momentum of 35 MeV/c, where the beam emittance is at its maximal value. Then the electron cooling is applied for the first time, particles have small transverse amplitudes, and nonlinearities are less harmful causing no beam losses. With beta function values at electron cooler $\beta_{x,y} \approx 2$ m the beam size, for the worst case scenario of a maximal emittance, is $\sigma_{x,y} = (75 \times 2)^{1/2} \approx 12.5$ mm which would still fit in the electron beam radius of 25 mm. The machine momentum deviation acceptance given as 2σ RMS is $dP/P = \pm 9 \times 10^{-3}$.

The behaviour of the 100 keV antiproton beam in 3D phase space is shown in Fig. 6.16 where the distribution of the beam emittance is plotted against the distribution of the beam momentum spread during four seconds of cooling. The particles are distributed according to a Gaussian shape and are located below the transverse and momentum acceptance limits.

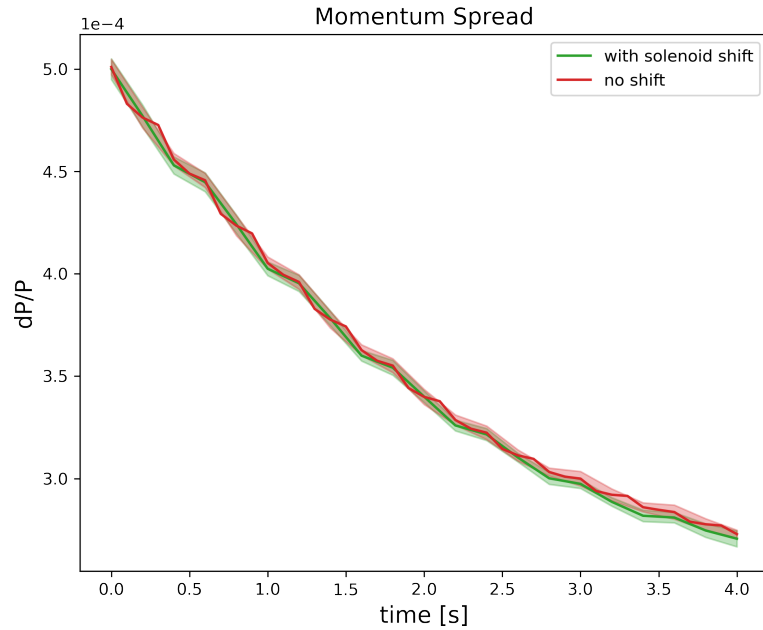


FIGURE 6.17: BETACOOOL longitudinal momentum spread for ELENA with and without the 0.8 mm solenoid shift.

Figure 6.17 shows the evolution of the momentum spread over the time span of the cooling with and without the solenoid misalignment. The imperfection does not impact the longitudinal spread of the antiprotons. The electron cooling largely reduces the momentum deviation, reaching very small final values of 2.7×10^{-4} . In this way, even with the momentum spread increase due to bunching before extraction, the requirements of experiments are met.

This concludes the simulation studies carried out for ELENA. It had been shown how introducing in the simulation model solenoid field imperfections (as observed in magnetic field measurements) the agreement with data is excellent. Investigating the impact of misalignment in the cooling performance, cooling maps were presented for different electron distribution models, as was done for the set of measurements from LEIR described in the previous Chapter. Finally, considerations of the effect of the ELENA electron cooler on the longitudinal plane were presented together with an overview of lifetime limiting factors and the mitigations implemented in the storage ring.

6.7 Suggested measurements for the future

With the recent restart of the ELENA operations, it is possible to anticipate that numerous measurement campaigns will be conducted, delivering new data that would help to improve the understanding of the processes influencing the antiproton beam and to further validate the observations presented in this chapter.

Measurements of the cooling force — as done for LEIR — using the electron energy-step method [137] would be of great interest to validate the modified Erlangen formula. Another effective technique to quantify the cooling force on bunched beam is the phase shift method. This is a well-established method, which for example has been used for measurements of the longitudinal cooling force in the recycler at Fermilab [157], at IUCF [158], MSL [159] and in TSR [160] in Heidelberg. By combining electron cooling and rf bunching, an equilibrium will be established for which the rf force balances the electron cooling force. The longitudinal component of the cooling force can then be related to the phase φ of the antiproton bunch relative to the rf system.

Additional measurements and studies, for example using the scraper, can give better insight on the cooler performance. These include taking pairs of scraper measurements in incremental time steps along the energy plateau to build up a more continuous picture of the emittance evolution in the presence of electron cooling. Similar measurements in the absence of cooling would allow an investigation into the significance and phase space growth rates introduced by IBS. The use of the scraper, unfortunately, is destructive and systematic measurements of emittance evolution along the cycle are time consuming.

Other emittance measurements, also using the IPMs and the Schottky monitors could be performed with and without cooling. Introducing a controlled orbit bump would help understanding if it is possible to counterbalance the solenoid field imperfection observed and to increase the cooling efficiency.

Chapter 7

Summary and Conclusions

A tailored simulation model for the ELENA storage ring has been developed and presented. The implementation of the different effects acting on the low energy antiprotons are based on both theoretical derivations and empirical observations of other low energy storage rings.

In the introductory chapter the ELENA storage ring was presented together with the motivations for its development and the relevance it holds in antimatter research was explained. An overview of the antiproton production and deceleration chain at CERN was also given, including a description of the several antimatter experiments and how they will benefit from the addition of ELENA to the antiproton chain.

In the second chapter important concepts such as emittance, beta functions, momentum spread, and dispersion have been introduced. Beam effects specific to low energy storage rings such as ELENA have also been introduced giving a theoretical framework for the simulations study. The fundamental concepts of the electron cooling technique were presented. Additionally a description of the beam instrumentation used for measurements was presented.

The third chapter went into details describing the model and approximations used for the electron cooling process and specifically the derivation of different force formulae. The approaches considered were the dielectric theory and the binary collision approximation, both of which are valid instrument for treating the cooling process. Along with the commonly used ones, a modified formula for negatively charged particles in presence of a guiding magnetic field was derived. The additional contribution to the cooling force was derived in the framework of the binary collision approximation and based on symmetry arguments. The resulting force is considerably increased compared to the

version independent on the circulating particle charge and for the ELENA case the maximum was found to be almost five times larger.

In the fourth chapter the simulation programs used in this study were described and benchmarked versus established measurements from a low energy storage ring equipped with an electron cooler. The new formulae derived in chapter 3 together were implemented in the Betacool code with other modifications necessary to correct bugs related to introducing negatively charged antiprotons in the simulations. Since it was shown that the simulations reached a good agreement with measurements performed on the machine, the introduction of the force additional contribution appears a valid choice for electron cooled storage rings for negatively charged ions and antiprotons.

In chapter 5 the simulation model was validated by comparisons with data taken at LEIR. The measurement process and the data analysis were described. A novel investigation on the LEIR electron cooler performance and imperfections was presented through the cooling maps for different electron beam velocity distributions. The observation of the cooling maps suggested the presence of a misalignment in the electron and ion orbits which can be counteracted with orbit corrections to increase the cooling efficiency. The emittance evolution data from LEIR showed good agreement with the beam evolution simulations based on the predictive model for low energy beam dynamics with different electron beam velocity distribution. This indicates that the beam profiles are correctly represented and the impact of the distribution on the cooling and heating effects are well implemented in the model.

The last chapter discusses the simulation studies made for the ELENA performance, comparing the obtained predictions with the limited data available. The simulation results showed very good agreement with measurements when observed magnetic field inhomogeneities were accounted for in the electron cooling code, validating the model. The presence of the magnetic field errors impacted the equilibrium emittances of about 0.1 mm mrad. The observed imperfection in the cooler could be compensated in the future ELENA operations improving the cooling efficiency and obtaining lower emittances. In order to investigate the effect of various misalignments, cooling maps were simulated for the ELENA machine employing different electron beam distribution models. This showed how different electron antiproton overlapping patterns can enhance or reduce the cooling efficiency of the machine. In the perspective of future upgrades in the ELENA cooler electron production, this maps can be used to identify the conditions for required performance targets.

Since the simulation models have been shown to have a good predictive ability when compared with scraper data taken from ELENA, it is proposed that it can be suitable for use in other low energy storage rings. The updated force formula for negatively charged

ions has been proved to be a valid instrument for electron cooling modelling and together with other modifications introduced for antiproton handling, it will be made available to the Betacool code share folder.

The results of the simulations also gave an accurate characterisation of the beam, essential for the optimisation of the transfer lines to the antimatter experiments. The importance of ELENA performance, and hence its optimisation, is entirely related to the delivery of high quality, low energy antiprotons to the antimatter experiments. In order to transport the cooled 100 keV antiprotons to the six experiments currently operating in the AD hall, electrostatic transport lines will be used. The use of electrostatic elements in such a large configuration is a relatively recent practice and much less common compared with the use of their magnetic counterparts. For example, the racetrack shaped electrostatic storage ring ELISA [161] was the first of its kind and was constructed as recently as 1998 in Denmark. It has since inspired other facilities to duplicate its design, such as ELASR constructed in Saudi Arabia between 2014 and 2015 [162]. The use of electrostatic elements was also considered for other design studies and potential facilities, such as FLAIR at FAIR [56, 163]. The electrostatic rigidity is independent of mass, so electrostatic elements become more desirable for low energy ion beams than their magnetic counterparts.

The simulations can be combined to studies of the transport lines to the experiments in the AD hall and investigate further sources of error, such as the influence of stray magnetic fields on beam stability [164]. Following the recent trend to apply machine learning to improve optimisation results [165, 166], with this type of study the antimatter community is expected to benefit from the beam improved quality at the handover points to all experiments. Finally, the simulations could extend to beyond the interface with experiments, for example to include the degrader foils at ALPHA and its antiproton trap [167]. Such an extension would allow a more comprehensive optimisation process and could further improve antiproton trapping efficiencies.

To conclude the study some interesting future experiments to expand the ELENA data pool are suggested, possibly to further validate the observations presented. For example experiments to measure the cooling force for antiproton in ELENA with different relative velocity would be of great interest to test the modified Erlangen formula. Additional time steps for emittance measurements can give an insight into the beam evolution during cooling and potentially further validate the simulation model.

7.1 Outlook

Simulations environments are essential for correctly plan, design and optimize the operations of accelerators. Although the theory has been developed decades ago and coolers have been successfully implemented in several accelerators, the numerical simulation of electron cooling remains challenging and the available tools presents limits. The introduction of a modified formula taking into account the repulsive potential between negatively charged particles and electrons overcomes some of these limits and there is ample opportunity to expand this work. The implementation of an IBS routine into the RF-Track code would offer an additional tool for long term simulations and, using the scripting languages Octave and Python as user interfaces, a more flexible instrument than Betacool.

The ELENA simulation may be enlarged including the AD antiproton deceleration tailoring beam parameters to specific conditions. Field maps of the cooler stray fields could be implemented into the simulation. Ongoing work to optimise the e-gun is being carried, aiming to develop a cold cathode gun based on carbon nanotubes. The resulting electron beam properties should be used for the ELENA antiproton beam characterisation.

Finally, applications of machine learning with the optimisation tools presented in these thesis would be of great interest and could offer a valuable instruments for improving the performance of electron cooled storage rings.

Bibliography

- [1] Accelerators Validating Antimatter. University Of Liverpool. URL <https://www.liverpool.ac.uk/ava/>. AVA - University of Liverpool.
- [2] Marie Skłodowska-Curie Actions. European Commission. URL <https://ec.europa.eu/research/mariecurieactions/>. Horizon Europe.
- [3] W. Bartmann et al. The ELENA facility. *Philosophical Transactions of the Royal Society A: Mathematical, Physical and Engineering Sciences*, 376(2116):20170266, 2018. doi: 10.1098/rsta.2017.0266. URL <https://royalsocietypublishing.org/doi/abs/10.1098/rsta.2017.0266>.
- [4] I. Meshkov, A. O. Sidorin, A. Smirnov, and G. Trubnikov. Physics guide of BETA-COOL code Version 1.1. Jan 2006. URL https://www.agsrhichome.bnl.gov/AP/ap_notes/ap_note_262.pdf.
- [5] A. Latina. Rf-track reference manual. Technical report, CERN, Geneva, Switzerland, 2020.
- [6] C. L. Bennett et al. First-year Wilkinson Microwave Anisotropy Probe (WMAP) observations: preliminary maps and basic results. *The Astrophysical Journal Supplement Series*, 148(1):1–27, September 2003. doi: 10.1086/377253. URL <https://doi.org/10.1086/377253>.
- [7] A. Das and T. Ferbel. *Introduction to nuclear and particle physics*. World Scientific, 2nd edition, 2003. doi: 10.1142/5460. URL <https://www.worldscientific.com/doi/abs/10.1142/5460>.
- [8] J. Ellis. Antimatter matters. *Nature*, 424(6949):631–634, Aug 2003. ISSN 1476-4687. doi: 10.1038/424631a. URL <https://doi.org/10.1038/424631a>.
- [9] U. Sarkar. *Particle and Astroparticle Physics*. Taylor & Francis Inc., 2008. doi: 10.1201/9781584889328.

- [10] A. Schuster. Potential matter—a holiday dream. *Nature*, 58(1503):367–367, Aug 1898. ISSN 1476-4687. doi: 10.1038/058367a0. URL <https://doi.org/10.1038/058367a0>.
- [11] P. A. M. Dirac and R. H. Fowler. The quantum theory of the electron. *Proceedings of the Royal Society of London. Series A, Containing Papers of a Mathematical and Physical Character*, 117(778):610–624, 1928. doi: 10.1098/rspa.1928.0023. URL <https://royalsocietypublishing.org/doi/abs/10.1098/rspa.1928.0023>.
- [12] R. Shankar. *Principles of quantum mechanics*. Springer Science & Business Media, 2012.
- [13] C. Y. Chao. Scattering of hard γ -rays. *Phys. Rev.*, 36:1519–1522, Nov 1930. doi: 10.1103/PhysRev.36.1519. URL <https://link.aps.org/doi/10.1103/PhysRev.36.1519>.
- [14] C. D. Anderson. Cosmic-ray positive and negative electrons. *Phys. Rev.*, 44:406–416, Sep 1933. doi: 10.1103/PhysRev.44.406. URL <https://link.aps.org/doi/10.1103/PhysRev.44.406>.
- [15] O. Chamberlain, E. Segrè, C. Wiegand, and T. Ypsilantis. Observation of antiprotons. *Phys. Rev.*, 100:947–950, Nov 1955. doi: 10.1103/PhysRev.100.947. URL <https://link.aps.org/doi/10.1103/PhysRev.100.947>.
- [16] W. L. Laurence. New atom particle found; termed a negative proton. *The New York Times*, 19 October 1955.
- [17] Nature Publishing Group. Nobel prize for physics for 1959 : Dr. Emilio Segrè and Dr. Owen Chamberlain. *Nature*, 184(4694):1189–1189, Oct 1959. ISSN 1476-4687. doi: 10.1038/1841189a0. URL <https://doi.org/10.1038/1841189a0>.
- [18] J. H. Christenson, J. W. Cronin, V. L. Fitch, and R. Turlay. Evidence for the 2π decay of the k_2^0 meson. *Phys. Rev. Lett.*, 13:138–140, Jul 1964. doi: 10.1103/PhysRevLett.13.138. URL <https://link.aps.org/doi/10.1103/PhysRevLett.13.138>.
- [19] V. L. Fitch. The discovery of charge-conjugation parity asymmetry. *Nobel lecture*, pages 594–603, 1980. ISSN 0034-6861. doi: 10.1103/revmodphys.53.367.
- [20] A. D. Sakharov. Violation of CP Invariance, C asymmetry, and baryon asymmetry of the universe. *Pisma Zh. Eksp. Teor. Fiz.*, 5:32–35, 1967. doi: 10.1070/PU1991v034n05ABEH002497.

- [21] C. Hagedorn et al. CP Violation in the Lepton Sector and Implications for Leptogenesis. *Int. J. Mod. Phys. A*, 33(05n06):1842006, 2018. doi: 10.1142/S0217751X1842006X.
- [22] F. Capozzi, C. Giunti, M. Laveder, and A. Palazzo. Joint short- and long-baseline constraints on light sterile neutrinos. *Phys. Rev. D*, 95(3):033006, 2017. doi: 10.1103/PhysRevD.95.033006.
- [23] K. Abe et al. Combined analysis of neutrino and antineutrino oscillations at T2K. *Phys. Rev. Lett.*, 118:151801, Apr 2017. doi: 10.1103/PhysRevLett.118.151801. URL <https://link.aps.org/doi/10.1103/PhysRevLett.118.151801>.
- [24] M. Fukugita and T. Yanagida. Baryogenesis without grand unification. *Physics Letters B*, 174(1):45–47, 1986. ISSN 0370-2693. doi: [https://doi.org/10.1016/0370-2693\(86\)91126-3](https://doi.org/10.1016/0370-2693(86)91126-3). URL <https://www.sciencedirect.com/science/article/pii/0370269386911263>.
- [25] A. G. Cohen and D. B. Kaplan. Spontaneous baryogenesis. *Nuclear Physics B*, 308(4):913–928, 1988. ISSN 0550-3213. doi: 10.1016/0550-3213(88)90134-4. URL <https://www.sciencedirect.com/science/article/pii/0550321388901344>.
- [26] E. Roueff et al. The full infrared spectrum of molecular hydrogen. *Astronomy & Astrophysics*, 630:A58, Sep 2019. ISSN 1432-0746. doi: 10.1051/0004-6361/201936249. URL <http://dx.doi.org/10.1051/0004-6361/201936249>.
- [27] Conseil Européen pour la Recherche Nucléaire. URL <https://home.cern/>.
- [28] G. Baur et al. Production of antihydrogen. *Physics Letters B*, 368(3):251–258, Feb 1996. doi: 10.1016/0370-2693(96)00005-6.
- [29] G. Blanford et al. Observation of atomic antihydrogen. *Phys. Rev. Lett.*, 80:3037–3040, Apr 1998. doi: 10.1103/PhysRevLett.80.3037. URL <https://link.aps.org/doi/10.1103/PhysRevLett.80.3037>.
- [30] M. Vretenar et al. *Linac4 design report*, volume 6 of *CERN Yellow Reports: Monographs*. CERN, Geneva, 2020. doi: 10.23731/CYRM-2020-006. URL <https://cds.cern.ch/record/2736208>.
- [31] C. Bracco. Injection: Hadron Beams. *CERN Yellow Rep. School Proc.*, 5:131, 2018. doi: 10.23730/CYRSP-2018-005.131. URL <https://e-publishing.cern.ch/index.php/CYRSP/article/view/700/500>.
- [32] E. Mobs. The CERN accelerator complex - 2019. Complexe des accélérateurs du CERN - 2019. Jul 2019. URL <https://cds.cern.ch/record/2684277>. General Photo.

- [33] D. Mhl. Production of low-energy antiprotons. *Hyperfine Interact.*, 109:33–41. 16 p, Sep 1996. doi: 10.1023/A:1012680728257. URL <https://cds.cern.ch/record/311679>.
- [34] S. Maury. The Antiproton Decelerator: AD. *Hyperfine Interactions*, 109(1):43–52, Aug 1997. ISSN 1572-9540. doi: 10.1023/A:1012632812327. URL <https://cds.cern.ch/record/405621/files/ps-99-050.pdf>.
- [35] S. A. Baird et al. Design study of the Antiproton Decelerator: AD. Technical report, CERN, Nov 1996. URL <https://cds.cern.ch/record/317704>.
- [36] H. Kalinowsky. Deceleration of antiprotons from MeV to keV energies. *Hyperfine Interactions*, 76:73–80, 1993.
- [37] MAD-X Homepage. URL <http://mad.home.cern.ch/mad/>. CERN - BE/ABP Accelerator Beam Physics Group.
- [38] W. Bertsche et al. The ALPHA experiment: A cold antihydrogen trap. In *LOW ENERGY ANTIPROTON PHYSICS: Eighth International Conference on Low Energy Antiproton Physics (LEAP '05)*, volume 796 of *AIP Conference Proceedings*, 2005. doi: 10.1063/1.2130184.
- [39] M. Hori and E. Widmann. ASACUSA proposal for ELENA. Technical report, CERN, Geneva, Oct 2019. URL <https://cds.cern.ch/record/2691506>.
- [40] S. Ulmer et al. High-precision comparison of the antiproton-to-proton charge-to-mass ratio. *Nature*, 524(7564):196–199, Aug 2015. ISSN 1476-4687. doi: 10.1038/nature14861. URL <https://doi.org/10.1038/nature14861>.
- [41] M. Ahmadi et al. Observation of the 1s–2s transition in trapped antihydrogen. *Nature*, 541(7638):506–510, Jan 2017. ISSN 1476-4687. doi: 10.1038/nature21040. URL <https://doi.org/10.1038/nature21040>.
- [42] A. Kellerbauer et al. The AEGIS experiment at CERN. In *EXA 2011*, pages 43–49, Dordrecht, 2012. Springer Netherlands. ISBN 978-94-007-4890-3.
- [43] C. So, J. Fajans, and W. Bertsche. The ALPHA-g antihydrogen gravity magnet system. *IEEE Transactions on Applied Superconductivity*, 30(4):1–5, 2020. doi: 10.1109/TASC.2020.2981272.
- [44] P. Debu and for the GBAR collaboration. Gbar. *Hyperfine Interactions*, 212(1):51–59, Dec 2012. ISSN 1572-9540. doi: 10.1007/s10751-011-0379-4. URL <https://doi.org/10.1007/s10751-011-0379-4>.

- [45] G. Consolati et al. Positronium for Antihydrogen Production in the AEGIS Experiment. *Acta Phys. Polon. A*, 132(5):1443–1449, 2017. doi: 10.12693/APhysPolA.132.1443.
- [46] M. Amoretti et al. Production and detection of cold antihydrogen atoms. *Nature*, 419(6906):456–459, Oct 2002. ISSN 1476-4687. doi: 10.1038/nature01096. URL <https://doi.org/10.1038/nature01096>.
- [47] A. E. Kramida. A critical compilation of experimental data on spectral lines and energy levels of hydrogen, deuterium, and tritium. *Atomic Data and Nuclear Data Tables*, 96(6):586–644, 2010. ISSN 0092-640X. doi: <https://doi.org/10.1016/j.adt.2010.05.001>. URL <https://www.sciencedirect.com/science/article/pii/S0092640X10000458>.
- [48] J. R. Danielson, D. H. E. Dubin, R. G. Greaves, and C. M. Surko. Plasma and trap-based techniques for science with positrons. *Rev. Mod. Phys.*, 87:247–306, Mar 2015. doi: 10.1103/RevModPhys.87.247. URL <https://link.aps.org/doi/10.1103/RevModPhys.87.247>.
- [49] D. J. Griffiths. Hyperfine splitting in the ground state of hydrogen. *American Journal of Physics*, 50(8):698–703, Aug 1982. doi: 10.1119/1.12733. URL <https://ui.adsabs.harvard.edu/abs/1982AmJPh..50..698G>.
- [50] M. Diermaier et al. In-beam measurement of the hydrogen hyperfine splitting and prospects for antihydrogen spectroscopy. *Nature Communications*, 8(1):15749, Jun 2017. ISSN 2041-1723. doi: 10.1038/ncomms15749. URL <https://doi.org/10.1038/ncomms15749>.
- [51] H. Dehmelt. Continuous Stern-Gerlach effect: Principle and idealized apparatus. *Proceedings of the National Academy of Sciences*, 83(8):2291–2294, 1986. ISSN 0027-8424. doi: 10.1073/pnas.83.8.2291. URL <https://www.pnas.org/content/83/8/2291>.
- [52] J. D. Tasson. The standard-model extension and gravitational tests. *Symmetry*, 8(11):111, 2016. doi: 10.3390/sym8110111.
- [53] M. Bohman et al. Sympathetic cooling of protons and antiprotons with a common endcap Penning trap. *Journal of Modern Optics*, 65(5-6):568576, Dec 2017. ISSN 1362-3044. doi: 10.1080/09500340.2017.1404656. URL <http://dx.doi.org/10.1080/09500340.2017.1404656>.
- [54] M. Niemann et al. *CPT test with (anti)proton magnetic moments based on quantum logic cooling and readout*, pages 41–44. World Scientific, 2014. doi:

- 10.1142/9789814566438_0011. URL https://www.worldscientific.com/doi/abs/10.1142/9789814566438_0011.
- [55] P. Debu. Status report on the GBAR CERN experiment. *Journal of Physics Conference Series*, 460:2008–, Oct 2013. doi: 10.1088/1742-6596/460/1/012008.
- [56] FLAIR. Facility for Low-Energy Antiproton and Ion Research. URL <http://www.flairatfair.eu>.
- [57] C. P. Welsch and H. Danared. FLAIR: a Facility for Low-energy Antiproton and Ion Research. In *Proceedings of EPAC 2006*, 2006.
- [58] E. Widmann. Low-energy antiproton physics and the FLAIR facility. In *9th International Conference on Nuclear Physics at Storage Rings*, Feb 2015.
- [59] U. Amaldi and G. Magrin. *Accelerators in Medicine*, pages 488–513. Jan 2013. ISBN 978-3-642-23052-3. doi: 10.1007/978-3-642-23053-0_43.
- [60] M R Cleland. Industrial applications of electron accelerators. 2006. doi: 10.5170/CERN-2006-012.383. URL <https://cds.cern.ch/record/1005393>.
- [61] R. F. Ziesche. 4D imaging of lithium-batteries using correlative neutron and X-ray tomography with a virtual unrolling technique. *Nature Communications*, 11(1): 777, Feb 2020. ISSN 2041-1723. doi: 10.1038/s41467-019-13943-3. URL <https://doi.org/10.1038/s41467-019-13943-3>.
- [62] F. Foglia et al. Aquaporin-like water transport in nanoporous crystalline layered carbon nitride. *Science Advances*, 6(39), 2020. doi: 10.1126/sciadv.abb6011. URL <https://advances.sciencemag.org/content/6/39/eabb6011>.
- [63] A. J. Antolak. Overview of accelerator applications for security and defense. *Reviews of Accelerator Science and Technology*, 8(11):27–36, Jan 2015. doi: 10.1142/S1793626815300029.
- [64] R. Appleby. *Introduction to Beam Dynamics*. Accelerator Lecture Series, Daresbury, UK, 2017. URL https://ukri.mediasite.com/Mediasite/Showcase/cockcroft_institute/Channel/lectures.
- [65] W. Barletta, L. Spentzouris, and E. Harms. US Particle Accelerator School notes, June 2012. URL <https://uspas.fnal.gov/materials/10MIT/Emittance.pdf>.
- [66] F. Zimmerman. Measurement and correction of accelerator optics. Jun 1998. doi: 10.1142/9789812818003_0002. URL <https://www.osti.gov/biblio/291052>.
- [67] H. Wiedemann. *Particle Accelerator Physics*. Springer, Berlin, 2007. doi: 10.1007/978-3-540-49045-6.

- [68] V. Chohan et al. *Extra Low ENergy Antiproton (ELENA) ring and its Transfer Lines: Design Report*. CERN Yellow Reports: Monographs. CERN, Geneva, 2014. doi: 10.5170/CERN-2014-002. URL <https://cds.cern.ch/record/1694484>.
- [69] H. Nersisyan, C. Tpffer and G. Zwicknagel. *Interactions between charged particles in a magnetic field: a theoretical approach to ion stopping in magnetized plasmas*. Springer, Berlin, 2008.
- [70] A Piwinski. Intra-beam-scattering. 1974. doi: 10.5170/CERN-1992-001.226. URL <https://cds.cern.ch/record/400720>.
- [71] M. P. Ehrlichman et al. Intrabeam scattering studies at the Cornell Electron Storage Ring Test Accelerator. *Phys. Rev. ST Accel. Beams*, 16:104401, Oct 2013. doi: 10.1103/PhysRevSTAB.16.104401. URL <https://link.aps.org/doi/10.1103/PhysRevSTAB.16.104401>.
- [72] D. V. Sivukhin. Coulomb collisions in a fully ionized plasma. *Rev. Plasma Phys. (USSR)(Engl. Transl.)*, Vol: 4, Jan 1966. URL <https://www.osti.gov/biblio/4541439>.
- [73] B. Touschek et al. Lifetime and beam size in a storage ring. *Phys. Rev. Lett.*, 10: 407–409, May 1963. doi: 10.1103/PhysRevLett.10.407. URL <https://link.aps.org/doi/10.1103/PhysRevLett.10.407>.
- [74] H. Bruck and J. Le Duff. Beam enlargement in storage rings by multiple Coulomb scattering. In *5th International Conference on High-Energy Accelerators*, 1965.
- [75] W. Chou and A. Piwinski. Intra-beam scattering in the SSC collider and in the boosters. Technical report, SSC, Dallas, TX, Jun 1992. URL <https://cds.cern.ch/record/241284>.
- [76] M. Martini. Intrabeam scattering in the ACOL-AA machines. Technical report, CERN, Geneva, 1984. URL <https://cds.cern.ch/record/151638>.
- [77] J. D. Bjorken and S. K. Mtingwa. Intrabeam scattering. *Part. Accel.*, 13:115–143, Jul 1982. URL <https://cds.cern.ch/record/140304>.
- [78] C. Carli, T. Rijoff, O. Karamyshev, and C. P. Welsch. Review of rest gas interaction at very low energies applied to the Extra Low Energy Antiproton ring ELENA. page 4 p, Jun 2014. URL <https://cds.cern.ch/record/1742278>.
- [79] N. Madsen. Beam evolution in the Antiproton Decelerator (AD) under the influence of residual gas and intra beam scattering. AD Note 047. URL <http://massen.web.cern.ch/physics/AD047.pdf>.

- [80] R. Kersevan. The Vacuum System of the Extra-Low Energy Antiproton Decelerator ELENA at CERN. In *6th International Particle Accelerator Conference*, 6 2015. doi: 10.18429/JACoW-IPAC2015-WEPHA010.
- [81] E. Mahner. The vacuum system of the low energy ion ring at cern: Requirements, design, and challenges. *Vacuum*, 81(6):727–730, 2007. ISSN 0042-207X. doi: <https://doi.org/10.1016/j.vacuum.2005.11.054>. URL <https://www.sciencedirect.com/science/article/pii/S0042207X05003994>. Proceedings of the European Vacuum Conference (EVC-9).
- [82] H. Bradt. *Astrophysics Processes*. Cambridge University Press, 2008. doi: <https://doi.org/10.1017/CBO9780511802249>.
- [83] G. Tranquille, L. Jrgensen, D. Luckin, and R. Warner. The CERN-ELENA Electron Cooler Magnetic System. pages 842–845, 2018. doi: 10.18429/JACoW-IPAC2018-TUPAF056. URL <https://cds.cern.ch/record/2649948>.
- [84] G. I. Budker. An effective method of damping particle oscillations in proton and antiproton storage rings. *Soviet Atomic Energy*, 22(5):438–440, May 1967. doi: 10.1007/bf01175204. URL <https://doi.org/10.1007/bf01175204>.
- [85] H. G. Hereward. Artificial damping in the CERN Proton Storage Rings. Technical report, CERN, Geneva, Sep 1966. URL <http://cds.cern.ch/record/954894>.
- [86] C. Habfast et al. The LEAR electron cooler: Recent improvements and tests. *Physica Scripta*, T22:277–281, Jan 1988. doi: 10.1088/0031-8949/1988/t22/041. URL <https://doi.org/10.1088/0031-8949/1988/t22/041>.
- [87] H. Poth et al. First Results of Electron Cooling Experiments at LEAR. *Zeitschrift fur Physik A Atomic Nuclei*, 332:171–188, 1989.
- [88] P. Belochitskii et al. Commissioning and first operation of the Antiproton Decelerator (AD). In *PACS2001. Proceedings of the 2001 Particle Accelerator Conference*, volume 1, pages 580–584 vol.1, 2001. doi: 10.1109/PAC.2001.987574.
- [89] Ya. S. Derbenev and A. N. Skrinsky. The Effect of an Accompanying Magnetic Field on Electron Cooling. *Part. Accel.*, 8:235–243, 1978.
- [90] M. E. Glinsky et al. Collisional equipartition rate for a magnetized pure electron plasma. *Physics of Fluids B: Plasma Physics*, 4(5):1156–1166, 1992. doi: 10.1063/1.860124. URL <https://doi.org/10.1063/1.860124>.
- [91] J. G. Siambis. Resonances in binary charged-particle collisions in a uniform magnetic field. *Phys. Rev. Lett.*, 37:1750–1753, Dec 1976. doi: 10.1103/PhysRevLett.37.1750. URL <https://link.aps.org/doi/10.1103/PhysRevLett.37.1750>.

- [92] G. Zwicknagel. Ion-electron collisions in a homogeneous magnetic field. *AIP Conference Proceedings*, 498(1), Dec 1999. ISSN 0094-243X. doi: 10.1063/1.1302150. URL <https://www.osti.gov/biblio/21210389>.
- [93] G. Zwicknagel. *Theory and Simulation of the Interaction of Ions with Plasmas: Nonlinear stopping, ion-ion correlation effects and collisions of ions with magnetized electrons*. PhD thesis, May 2000.
- [94] P. Forck, P. Kowina, and D. Liakin. Beam position monitors. 2009. doi: 10.5170/CERN-2009-005.187. URL <https://cds.cern.ch/record/1213277>.
- [95] D. A. Goldberg and G. R. Lambertson. Dynamic devices. a primer on pickups and kickers. *AIP Conference Proceedings*, 249(1):537–600, 1992. doi: 10.1063/1.41979. URL <https://aip.scitation.org/doi/abs/10.1063/1.41979>.
- [96] J. Bosser and L. Burnod. Proposal for a profile detector. page 7 p., Aug 1978. CERN-SPS-ABM-JB-78-3 report.
- [97] L. Sby et al. Elena Orbit and Schottky Measurement Systems. page MOPTY056. 4 p, 2015. URL <https://cds.cern.ch/record/2141807>.
- [98] P. Forck. Lecture Notes on Beam Instrumentation and Diagnostics, 2017. URL https://indico.cern.ch/event/569714/contributions/2303731/attachments/1415057/2166101/juas_script.pdf.
- [99] H Schoenauer. BEAMSCOPE - A novel device for measuring emittances and betatron amplitude distributions. 1979. URL <https://cds.cern.ch/record/890485>.
- [100] J. Hunt, C. Carli, J. Resta-Lpez, and C. Welsch. A new method for emittance reconstruction using a scraper in a dispersive region of a low energy storage ring. page MOPAB127. 4 p, 2017. doi: 10.18429/JACoW-IPAC2017-MOPAB127. URL <https://cds.cern.ch/record/2289126>.
- [101] J. R. Hunt et al. Novel transverse emittance measurements for electron cooling characterization. *Phys. Rev. Accel. Beams*, 23:032802. 9 p, 2020. doi: 10.1103/PhysRevAccelBeams.23.032802. URL <http://cds.cern.ch/record/2712780>.
- [102] Yaroslav S Derbenev and A N Skrinsky. The Kinetics Of Electron Cooling Of Beams On Heavy Particle storage Rings. *Part. Accel.*, 8:1–20, 1977. URL <https://cds.cern.ch/record/923404>.
- [103] Ya. S. Derbenev and A. N. Skrinskii. Magnetization effects in electron cooling. *Soviet Journal of Plasma Physics*, 4:273–278, May 1978.

- [104] D.V. Pestrikov. Magnetized electron cooling map. *Nuclear Instruments and Methods in Physics Research Section A: Accelerators, Spectrometers, Detectors and Associated Equipment*, 412(2):288–293, 1998. ISSN 0168-9002. doi: 10.1016/S0168-9002(98)80029-6. URL <https://www.sciencedirect.com/science/article/pii/S0168900298800296>.
- [105] M. Walter. *Dielektrische lineare Antworttheorie magnetisierter Elektronenplasmen*. PhD thesis, Universitt Erlangen, 2002.
- [106] H. B. Nersisyan, M. Walter, and G. Zwicknagel. Stopping power of ions in a magnetized two-temperature plasma. *Phys. Rev. E*, 61:7022–7033, Jun 2000. doi: 10.1103/PhysRevE.61.7022. URL <https://link.aps.org/doi/10.1103/PhysRevE.61.7022>.
- [107] B. Mllers et al. Cooling of ions and antiprotons with magnetized electrons. *Nuclear Instruments and Methods in Physics Research Section A: Accelerators, Spectrometers, Detectors and Associated Equipment*, 532(1):279–284, 2004. ISSN 0168-9002. doi: <https://doi.org/10.1016/j.nima.2004.06.057>. URL <https://www.sciencedirect.com/science/article/pii/S0168900204012550>. International Workshop on Beam Cooling and Related Topics.
- [108] M. Walter, C. Tpffer, and G. Zwicknagel. Particle-in-cell simulation of the stopping power in the presence of a magnetic field. *Hyperfine Interactions*, 115:67–72, Jan 1998. doi: 10.1023/A:1012688319905.
- [109] A. A. Vlasov. The vibrational properties of an electron gas. *Phys. Usp.*, 10(6): 721–733, 1968. doi: 10.1070/PU1968v010n06ABEH003709. URL <https://ufn.ru/en/articles/1968/6/a/>.
- [110] C. Tpffer. Scattering of magnetized electrons by ions. *Phys. Rev. A*, 66:022714, Aug 2002. doi: 10.1103/PhysRevA.66.022714. URL <https://link.aps.org/doi/10.1103/PhysRevA.66.022714>.
- [111] H. B. Nersisyan. Scattering of magnetized electrons by a moving heavy ion. *Nuclear Instruments and Methods in Physics Research Section B: Beam Interactions with Materials and Atoms*, 205:276–280, 2003. ISSN 0168-583X. doi: [https://doi.org/10.1016/S0168-583X\(02\)01974-2](https://doi.org/10.1016/S0168-583X(02)01974-2). URL <https://www.sciencedirect.com/science/article/pii/S0168583X02019742>. 11th International Conference on the Physics of Highly Charged Ions.
- [112] V.V. Parkhomchuk. Recent development in electron cooling and its applications. pages 462–464. High Energy Accelerator Research Organization (KEK), Tsukuba : KEK, 1998, 1998.

- [113] V.V. Parkhomchuk. New insights in the theory of electron cooling. *Nuclear Instruments and Methods in Physics Research Section A: Accelerators, Spectrometers, Detectors and Associated Equipment*, 441(1):9–17, 2000. URL <https://www.sciencedirect.com/science/article/pii/S0168900299011006>.
- [114] M. Reiser. *Theory and Design of Charged Particle Beams*. Wiley, 1994.
- [115] L. Serafini and J. B. Rosenzweig. Envelope analysis of intense relativistic quasi-laminar beams in rf photo-injectors: ma theory of emittance compensation. *Phys. Rev. E*, 55:7565–7590, Jun 1997. doi: 10.1103/PhysRevE.55.7565. URL <https://link.aps.org/doi/10.1103/PhysRevE.55.7565>.
- [116] A. O. Sidorin, I. N. Meshkov, I. A. Seleznev, A. V. Smirnov, E. M. Syresin, and G. V. Trubnikov. BETACOOOL program for simulation of beam dynamics in storage rings. *Nucl. Instrum. Meth. A*, 558:325–328, 2006. doi: 10.1016/j.nima.2005.11.041.
- [117] A. V. Fedotov et al. Simulations of high-energy electron cooling. United States, May 2005. URL <https://www.osti.gov/biblio/15016270>.
- [118] C. Dimopoulou et al. Design of the new experimental storage ring for operation with ions and antiprotons. *Phys. Rev. ST Accel. Beams*, 10:020101, Feb 2007. doi: 10.1103/PhysRevSTAB.10.020101. URL <https://link.aps.org/doi/10.1103/PhysRevSTAB.10.020101>.
- [119] B. Glnander et al. Cooling Force Measurements at CELSIUS. *AIP Conference Proceedings*, 821(1):259–264, 2006. doi: 10.1063/1.2190120. URL <https://aip.scitation.org/doi/abs/10.1063/1.2190120>.
- [120] A. Noda, M. Ikegami, and T. Shirai. Approach to ordered structure of the beam at s-LSR. *New Journal of Physics*, 8(11):288–288, Nov 2006. doi: 10.1088/1367-2630/8/11/288. URL <https://doi.org/10.1088/1367-2630/8/11/288>.
- [121] D. S. Lemons and A. Gythiel. Paul Langevins 1908 paper On the Theory of Brownian Motion [Sur la thorie du mouvement brownien, C. R. Acad. Sci. (Paris) 146, 530533 (1908)]. *American Journal of Physics*, 65(11):1079–1081, 1997. doi: 10.1119/1.18725. URL <https://doi.org/10.1119/1.18725>.
- [122] Yu. Eidelman and A.V. Fedotov. Recent developments of the SIMCOOL code. unpublished, 2004.
- [123] A.V. Fedotov, A. O. Sidorin, and A. V. Smirnov. IBS for non-gaussian distributions. In *Proceedings of the 46th ICFA Advanced Beam Dynamics Workshop on High-Intensity and High-Brightness Hadron Beams*, 9 2010.

- [124] A. D. Fokker. Die mittlere Energie rotierender elektrischer Dipole im Strahlungsfeld. *Annalen der Physik*, 348(5):810–820, 1914. doi: <https://doi.org/10.1002/andp.19143480507>. URL <https://onlinelibrary.wiley.com/doi/abs/10.1002/andp.19143480507>.
- [125] Deutsche Akademie der Wissenschaften zu Berlin. *Sitzungsberichte der Königlich Preussischen Akademie der Wissenschaften zu Berlin.*, volume Jan-Dec 1917. 1917. URL <https://www.biodiversitylibrary.org/item/92720>. <https://www.biodiversitylibrary.org/bibliography/42231>.
- [126] D. M. Benov. The Manhattan Project, the first electronic computer and the Monte Carlo method. *Monte Carlo Methods and Applications*, 22(1):73–79, 2016. doi: [doi:10.1515/mcma-2016-0102](https://doi.org/10.1515/mcma-2016-0102). URL <https://doi.org/10.1515/mcma-2016-0102>.
- [127] C. Runge and H. Knig. *Vorlesungen ber numerisches Rechnen*. Springer, Berlin, 1924.
- [128] P. L. DeVries and J. Hasbun. *A First Course in Computational Physics*. Jones & Bartlett Learning, 2011. ISBN 9780763773144. URL <https://books.google.de/books?id=X3FEPiebLH0C>.
- [129] E. Sli and D. F. Mayers. *An Introduction to Numerical Analysis*. Cambridge University Press, 2003. doi: [10.1017/CBO9780511801181](https://doi.org/10.1017/CBO9780511801181).
- [130] A. Degiovanni et al. Design of a fast-cycling high-gradient rotating Linac for protontherapy. In *4th International Particle Accelerator Conference*, Jun 2013.
- [131] S. Benedetti, A. Grudiev, and A. Latina. Design of a 750 MHz IH structure for medical applications. In *Proceedings of the 28th International Linear Accelerator Conference (LINAC16)*, Sep 2016.
- [132] S. Benedetti, U. Amaldi, A. Grudiev, and A. Latina. Design of a proton travelling wave linac with a novel tracking code. In *Proc. 6th Int. Particle Accelerator Conf. (IPAC'15)*, pages 3945–3948. JACoW Publishing, May 2015. doi: [doi:10.18429/JACoW-IPAC2015-THPF101](https://doi.org/10.18429/JACoW-IPAC2015-THPF101).
- [133] Janet Schmidt and Andrea Latina. Simulations of Beam-Beam Interactions With RF-Track for the AWAKE Primary Beam Lines. page THPAB050. 4 p, 2017. doi: [10.18429/JACoW-IPAC2017-THPAB050](https://doi.org/10.18429/JACoW-IPAC2017-THPAB050). URL <https://cds.cern.ch/record/2289646>.
- [134] C. Bayar, S. Doebert, A. Latina, and A. K. Ciftci. Tracking simulations and optimization of the clic injector linac. *AIP Conference Proceedings*, 1935(1):070004,

2018. doi: 10.1063/1.5025985. URL <https://aip.scitation.org/doi/abs/10.1063/1.5025985>.
- [135] M. Galassi et al. GNU scientific library reference manual, 2018. URL <https://www.gnu.org/software/gsl/>.
- [136] M. Steck et al. Commissioning of the ESR electron cooling device. In *"EPAC 92: Third European Particle Accelerator Conference"*, 01 1992.
- [137] T. Winkler et al. Electron cooling force measurements for highly charged ions in the ESR. *Hyperfine Interactions*, 99(1):277–283, December 1996. doi: 10.1007/BF02274931. URL <https://ui.adsabs.harvard.edu/abs/1996HyInt..99..277W>.
- [138] T. Winkler. *"Untersuchung zur Elektronenkhlung hochgeladener schwerer Ionen"*. PhD thesis, Ruprecht-Karls-Universitt, 1996.
- [139] Simon Albright et al. Review of LEIR operation in 2018. Dec 2019. URL <http://cds.cern.ch/record/2715365>.
- [140] S. Maury and D. Mohl. Combined longitudinal and transverse multiturn injection into a heavy ion accumulator ring. Technical report, CERN, Geneva, May 1994. URL <https://cds.cern.ch/record/2636534>.
- [141] J. Bosser et al. The production of dense lead-ion beams for the CERN LHC. *Nuclear Instruments and Methods in Physics Research Section A: Accelerators, Spectrometers, Detectors and Associated Equipment*, 441:116–122. 8 p, Jun 1999. doi: 10.1016/S0168-9002(99)01120-1. URL <https://cds.cern.ch/record/390617>.
- [142] S. Nagaitsev and V. V. Parkhomchuk. Development of electron coolers in Novosibirsk. In *IPAC12: Third International Particle Accelerator Conference*, 5 2012.
- [143] C Carli, P Belochitskii, M Chanel, and J Pasternak. LEIR lattice. page 4 p, Jul 2006. URL <https://cds.cern.ch/record/972662>. revised version submitted on 2006-09-15 14:51:41.
- [144] G. Tranquille. Specification of a new electron cooler for the low energy ion accumulator ring, LEIR. *Nucl. Instrum. Meth. A*, 532:399–402, 2004. doi: 10.1016/j.nima.2004.06.072.
- [145] C. Bal, V. Prieto, R. Sautier, and G. Tranquille. First results from the LEIR ionisation profile monitors. 2007. URL <https://cds.cern.ch/record/1045238>.
- [146] G. Tranquille. Optimum parameters for electron cooling. In *Workshop on Beam Cooling and Related Topics*, Sep 2001.

- [147] J. W. Xia and CSR Group. Lanzhou cooler storage ring commissioning. In *1st International Particle Accelerator Conference, IPAC10*, pages 3611–3615, Jun 2010. URL <https://accelconf.web.cern.ch/IPAC10/papers/thymh01.pdf>.
- [148] G. Tranquille et al. LEIR electron cooler status. Jul 2006. doi: 10.1063/1.2190093. URL <https://cds.cern.ch/record/972691>.
- [149] G. Tranquille et al. Commissioning of the LEIR electron cooler with Pb^{+54} ions. 2006. URL <https://cds.cern.ch/record/2252621>.
- [150] P. Belanger. *Unidentified Falling Objects in the Large Hadron Collider: formation, charging mechanisms and dynamics of dust particulates in a high energy proton accelerator*. PhD thesis, Oct 2020. URL <https://cds.cern.ch/record/2744948>. Master Thesis.
- [151] D. Mirarchi et al. Special Losses during LHC Run 2. *9th LHC Operations Evian Workshop*, pages 213–220, Feb 2019. URL <https://cds.cern.ch/record/2750296>.
- [152] J. R. Hunt. *Beam Quality Characterisation and the Optimisation of Next Generation Antimatter Facilities*. PhD thesis, University of Liverpool, 2019. URL https://www.liverpool.ac.uk/media/livacuk/quasargroup/files/downloads/JamesHunt-PhD_Thesis.pdf.
- [153] C. Grossmann, H. Roos, and M. Stynes. *Numerical Treatment of Partial Differential Equations*. Springer-Verlag Berlin Heidelberg.
- [154] G. Tranquille et al. The ELENA Electron Cooler. 2016. doi: 10.18429/JACoW-IPAC2016-TUPMR006. URL <https://cds.cern.ch/record/2207345>.
- [155] D. Luckin. ELENA electron cooler magnetic measurement report. May 2017. URL https://e-beam.web.cern.ch/e-cooling/docs/ELENA_MeasReport_17_05_26.pdf.
- [156] T. J. Roberts et al. G4beamline particle tracking in matter dominated beam lines. *Conf. Proc. C*, 110328:373–375, 2011.
- [157] S. Nagaitsev et al. Experimental demonstration of relativistic electron cooling. *Phys. Rev. Lett.*, 96, 2006. doi: 10.1103/PhysRevLett.96.044801.
- [158] D. D. Caussyn et al. Effects of a nonlinear damping force in synchrotrons with electron cooling. *Phys. Rev.*, E51(5):49474957, 1995. doi: 10.1103/PhysRevE.51.4947.

- [159] H. Danared. Electron cooling at Cryring with an expanded electron beam. *Nucl. Inst. and Meth*, A391(1):2431, 1997. doi: 10.1016/S0168-9002(97)00249-0.
- [160] M. Beutelspacher et al. Longitudinal and transverse electron cooling experiments at the Heidelberg heavy ion storage ring TSR. *Nucl. Inst. and Meth*, A441(1-2): 110115, 2000. doi: 10.1016/S0168-9002(99)01119-5.
- [161] S. P. Mller. ELISA, and electrostatic storage ring for atomic physics. *Nuclear Instruments and Methods in Physics Research Section A: Accelerators, Spectrometers, Detectors and Associated Equipment*, 394(3):281–286, 1997.
- [162] M. O. El Ghazaly. ELASR An electrostatic storage ring for atomic and molecular physics at KACST. *Results in Physics*, 5:60–61, Jan 2015.
- [163] C. P. Welsch and J. Ullrich. FLAIR a facility for low-energy antiproton and ion research. In *4th International Conference on Trapped Charged Particles and Fundamental Physic*. Berlin, Heidelberg: Springer Berlin Heidelberg, 2006.
- [164] V. Rodin et al. Multi-objective optimization of 3D beam tracking in electrostatic beamlines. In *Proceedings of the 10th International Particle Accelerator Conference: IPAC19*, 07 2019. doi: 10.18429/JACoW-IPAC2019-WEPTS060.
- [165] F. Wang, M. Song, A. Edelen, and X. Huang. Machine learning for design optimization of storage ring nonlinear dynamics. *ArXiv*, abs/1910.14220, 2019.
- [166] Z. Zhang, M. Song, and X. Huang. Online accelerator optimization with a machine learning-based stochastic algorithm. *Machine Learning: Science and Technology*, 2(1), Dec 2020. doi: 10.1088/2632-2153/abc81e. URL <https://doi.org/10.1088/2632-2153/abc81e>.
- [167] S. Fabbri and W. Bertsche. Optimization of Antiproton Capture for Antihydrogen Creation in the ALPHA Experiment. In *8th International Beam Instrumentation Conference*, 2019. doi: 10.18429/JACoW-IBIC2019-WEPP040.